

UNIVERSITY OF RIJEKA  
FACULTY OF ENGINEERING  
Department of Naval Architecture and Ocean Engineering

Ivan Sulovsky

**NUMERICAL MODELLING OF SHIP  
PROPULSION CHARACTERISTICS IN  
SEA WAVES**

DOCTORAL THESIS

Rijeka, 2026



UNIVERSITY OF RIJEKA  
FACULTY OF ENGINEERING  
Department of Naval Architecture and Ocean Engineering

Ivan Sulovsky

**NUMERICAL MODELLING OF SHIP  
PROPULSION CHARACTERISTICS IN  
SEA WAVES**

DOCTORAL THESIS

Supervisor: Prof. dr. sc. Jasna Prpić-Oršić

Co-supervisor: Assist. Prof. dr. sc. Andro Bakica

Rijeka, 2026



SVEUČILIŠTE U RIJECI  
TEHNIČKI FAKULTET

Zavod za brodogradnju i inženjerstvo morske tehnologije

Ivan Sulovsky

**NUMERIČKO MODELIRANJE  
PROPULZIJSKIH KARAKTERISTIKA  
BRODA NA MORSKIM VALOVIMA**

DOKTORSKI RAD

Mentorica: Prof. dr. sc. Jasna Prpić-Oršić

Komentor: Doc. dr. sc. Andro Bakica

Rijeka, 2026



Thesis Supervisor: Prof. Jasna Prpić-Oršić, PhD

University of Rijeka, Faculty of Engineering, Croatia

Thesis Co-Supervisor: Assist. Prof. Andro Bakica, PhD

University of Split, Faculty of Maritime studies, Croatia

This doctoral thesis was defended on \_\_\_\_\_ at the University of Rijeka,  
Faculty of Engineering, Rijeka, Croatia, in front of the following Evaluation  
Committee:

1. Assoc. Prof. Anton Turk, PhD, Chairman of the Committee

University of Rijeka, Faculty of Engineering, Croatia

2. Prof. Zoran Čarija, PhD, Member of the Committee

University of Rijeka, Faculty of Engineering, Croatia

3. Prof. Nastia Degiuli, PhD, Member of the Committee

University of Zagreb, Faculty of Mechanical Engineering and Naval Architecture,  
Croatia



## ACKNOWLEDGMENTS

This work was supported by the Croatian Science Foundation under the project HRZZ-IP-2022-10-2821. This thesis was also supported by the University of Rijeka (PROJECTS no. PU-17 uniri-iz-25-10 - Funded by the European Union – NextGenerationEU).

I want to first thank Marija and Igor Marač, my high school teachers who took on the challenging task of showing a group of teenagers the beauty and complexity of building ships. Their passion for the subject stayed with me. The biggest thanks go to Jasna Prpić-Oršić, for recognizing my passion for numerical modelling in ship hydrodynamics and encouraging me to pursue this research direction. Your supervision created a thriving working environment with abundant resources and valuable networking opportunities, for which I am deeply grateful. I also want to thank Andro Bakica, who served as co-supervisor for this thesis. Your expertise in C++ and patience with me as I learned the source code were essential to making this research successful. I am also grateful to all my colleagues at the Department of Naval Architecture and Ocean Engineering for being supportive throughout the years. I would especially like to acknowledge the late Prof. Roko Dejhalla, whose enthusiasm and encouragement for pursuing this field were particularly motivating. Also, many thanks to prof. Ould el Moctar from the University of Duisburg-Essen, Germany, for including me in the research group during my stay and giving me access to full-scale data. A warm thanks also goes to prof. Marilena Greco from Norwegian University of Science and Technology, Norway, who enabled me to get my hands on high-quality experimental data in model scale. My enrollment in the ship hydrodynamics course at MARIN, Netherlands, was supported by Croatian Science Foundation, for which I am particularly grateful. Furthermore, as the core of this thesis builds on OpenFOAM, an open-source project created through the volunteer work of many experts, it is important to acknowledge their contributions, without which this research would not have been possible in its current form.

Finally, I wish to thank my wife for incredible patience. Many times I was physically present but mentally elsewhere, with my thoughts deep in code that wouldn't work. On a more personal note, no academic or professional achievement even comes close to my greatest one: my boys, Oliver and Fran. Your arrival during this PhD brought some challenges but far more joy and beauty, for which I am forever grateful.

## Abstract

Ship propulsion systems are the main source of environmental pollution in global maritime transport, where performance in realistic wave conditions differs substantially from calm water design principles. Added resistance and changed propeller performance due to ship motions require reliable predictions and computational models that can capture wave-induced motions and their impact on propulsion characteristics across different scales. This thesis develops and validates numerical methods for predicting ship propulsion performance in waves using Computational Fluid Dynamics. Two numerical models are developed in OpenFOAM: an Actuator Disk model that represents the propeller as a simplified volumetric disk, and a Coupled Sliding Mesh model based on fully discretized propeller geometry coupled with rigid body dynamics. The first part applies the Actuator Disk model to a full-scale Post-Panamax containership, with results compared to onboard measurements recorded in actual ocean environments. The second part applies both models to a containership scale model in regular head waves, with validation against free-running model tests conducted in a towing tank. Both models accurately predict thrust and torque in calm water self-propulsion simulations. However, in wave conditions, the Coupled Sliding Mesh model provides better accuracy in severe sea states, while the Actuator Disk model shows limitations at higher sea states and longer wavelengths. The main scientific contributions include validated full-scale CFD simulations compared directly with onboard measurements, development and comparison of two propeller modeling approaches across different scales and conditions, and quantified accuracy limits of simplified propeller models in realistic wave environments.

### Key words

CFD, OpenFOAM, Actuator Disk, Coupled Sliding Mesh, hull-propeller interaction

## PROŠIRENI SAŽETAK

Brodski propulzijski sustavi predstavljaju glavni izvor onečišćenja okoliša u globalnom pomorskom prometu. Kako bi se odgovorilo na taj izazov, Međunarodna pomorska organizacija IMO postavila je cilj smanjenja godišnjih emisija stakleničkih plinova iz međunarodne plovidbe za najmanje 20 % do 2030. godine te za najmanje 80 % do 2040. godine. U svrhu smanjenja okolišnog zagađenja kroz hidrodinamičke aspekte, većina numeričkih istraživanja temelji se na uvjetima mirne vode, dok se stvarni okolišni uvjeti koji uključuju valove, vjetar i morske struje često ne uzimaju u obzir zbog povećanih zahtjeva za računalnom snagom. Propulzijske značajke broda u realnim uvjetima plovidbe značajno se razlikuju od onih u mirnoj vodi. Povećanje snage stroja u realnim uvjetima se prvenstveno pripisuje dodatnom otporu te promijenjenim uvjetima rada broskog vijka uslijed gibanja broda. Pouzdana predviđanja navedenih učinaka zahtijevaju računalne modele koji mogu obuhvatiti gibanje broda izazvana valovima te istodobno njihov utjecaj na propulziju broda pri različitim mjerilima i režimima rada. Ova disertacija bavi se izazovom numeričkih proračuna hidrodinamičkih značajki broda u realnim okolišnim uvjetima, oslanjajući se na numerički pristup temeljen na računalnoj dinamici fluida. U okviru disertacije razvijena su dva numerička modela u programskom okruženju OpenFOAM. Prvi model, temeljen na teoriji idealnog diska, predstavlja pojednostavljeni i matematički idealizirani prikaz broskog vijka. U modelu se stvarna geometrija vijka zamjenjuje volumetrijskim diskom u kojem se poriv i moment modeliraju prema Goldsteinovoj optimalnoj distribuciji. Drugi numerički model, oslovljen kao spregnuta klizeća mreža, temelji se na potpunoj diskretizaciji geometrije broskog vijka, pri čemu je rotacijsko gibanje vijka spregnuto s gibanjem broda, čime se omogućuje visoka razina točnosti u procjeni propulzijskih značajki broda. U prvom dijelu disertacije, model idealnog diska primjenjuje se na kontejnerski brod tipa Post-Panamax u naravnoj veličini, pri čemu se numerički rezultati izravno uspoređuju u vremenskoj domeni s rezultatima mjerenja na brodu. Time se ostvaruje doprinos razvoju i primjeni računalne dinamike fluida u hidrodinamici broda u naravnoj veličini. U prvom koraku, provode se simulacije broskog vijka u slobodnoj vožnji radi određivanja krivulja poriva i momenta koji su potrebni modelu idealnog diska. Zatim se provodi numerička verifikacija za jedan koeficijent napredovanja broskog vijka u slobodnoj vožnji radi utvrđivanja diskretizacijske pogreške. Nakon toga se provode numeričke simulacije

vlastitog pogona broda u naravi, pri čemu su rezultati uspoređeni s dostupnim podacima iz pokusne plovidbe Post-Panamax kontejnerskog broda, čime je postavljena čvrsta osnova za numeričke simulacije na nepravilnom valovlju. Rezultati simulacija pokazuju da model idealnog diska točno predviđa propulzijske značajke u reprezentativnom, često prisutnom stanju mora, tj. okolišnim uvjetima u kojima su provedena brodska mjerenja. Drugi dio disertacije uključuje primjenu oba modela, idealnog diska i spregnute klizeće mreže, na model kontejnerskog broda, pri čemu se rezultati izravno uspoređuju s eksperimentalnim podacima dobivenim iz vlastitog pogona modela broda na pravilnim valovima. Model kontejnerskog broda se podvrgava simulacijama vlastitog pogona primjenom oba numerička modela propulzije radi utvrđivanja njihove točnosti u uvjetima mirne vode. Rezultati pokazuju da oba modela točno predviđaju poriv i moment te istodobno zadovoljavaju uvjet točke vlastitog pogona. Kao i u prvom dijelu disertacije, provedena je u ovom slučaju pojednostavljena analiza osjetljivosti mreže zbog visokih računalnih zahtjeva numeričkih modela. Analiza osjetljivosti mreže pokazuje zanemariv utjecaj veličine mreže, što daje dovoljnu razinu pouzdanosti za nastavak simulacija propulzije na valovima. Osim finoće mreže, iznimno je važno ostvariti valne parametre u računalnoj domeni što se ispituje kroz dvodimenzionalnu analizu propagiranja pravilnih valova. Na temelju toga, oba numerička modela propulzije testirana su u uvjetima pravilnih pramčanih valova. Opsežan skup numeričkih simulacija pokazuje da model idealnog diska daje rezultate zadovoljavajuće kvalitete u primjeni pri naravnoj veličini, uz uspješno predviđanje dodatne potrebne snage u umjerenom stanju mora. U modelskom mjerilu, model idealnog diska pokazuje pogoršanje rezultata u odnosu na spregnutu klizeću mrežu, što implicira da njegova primjena nije opravdana pri težim stanjima mora. Međudjelovanje broskog trupa i broskog vijka kvantificirano je za oba modela, pri čemu rezultati u naravnoj veličini ukazuju na blago smanjenje propulzivne učinkovitosti, dok rezultati u mjerilu modela ukazuju na neznatno povećanje u odnosu na mirnu vodu.

### **Ključne riječi**

CFD, OpenFOAM, propulzija broda, idealni disk, spregnuta klizeća mreža, međudjelovanje trup-vijak

# Contents

<b>Acknowledgments</b>	<b>ix</b>
<b>Abstract</b>	<b>x</b>
<b>Prošireni sažetak</b>	<b>xii</b>
<b>1 Introduction</b>	<b>1</b>
1.1 Literature Review . . . . .	3
1.2 Objectives and Main Hypotheses . . . . .	7
1.3 Organization of the Thesis . . . . .	9
<b>2 Numerical Model of Fluid Flow</b>	<b>10</b>
2.1 Mathematical Model . . . . .	10
2.1.1 Governing Equations . . . . .	10
2.1.2 Turbulent Flow . . . . .	12
2.2 Discretization of the Mathematical Model . . . . .	16
2.2.1 Integral Formulation and Discretization . . . . .	16
2.2.2 Finite Volume Method Framework . . . . .	18
2.2.3 Discretization Schemes . . . . .	19
2.2.4 Solution of the Algebraic System . . . . .	21
<b>3 Numerical Propulsion Models in OpenFOAM</b>	<b>23</b>
3.1 Actuator Disk (AD) Model . . . . .	23
3.2 Coupled Sliding Mesh (CSM) Model . . . . .	28
<b>4 Propulsive Coefficients</b>	<b>32</b>
4.1 Definition and Physical Interpretation . . . . .	32
4.2 Methodology for Estimation of Propulsive Coefficients in Waves . . . . .	33
<b>5 Numerical Modelling of Ship Propulsion in Full Scale</b>	<b>36</b>
5.1 Post-Panamax Containership and Full-Scale Data . . . . .	36
5.1.1 Post-Panamax Containership . . . . .	37
5.1.2 Onboard Measurements . . . . .	39
5.2 Open Water Propeller Simulations . . . . .	41
5.3 Sea Trial Simulations . . . . .	45
5.3.1 Results of Sea Trial Simulations . . . . .	49
5.3.2 Influence of the Superstructure's Air Resistance in Sea Trial Simulations	51

5.4	Simulation in a Representative Sea State . . . . .	53
5.4.1	Assessment of Wave Spectrum in 2D . . . . .	54
5.4.2	Results of a Simulation in a Representative Sea State . . . . .	58
<b>6</b>	<b>Numerical Modelling of Ship Propulsion in Model Scale</b>	<b>63</b>
6.1	Experimental Data in Model Scale . . . . .	63
6.2	Self-Propulsion Simulations in Calm Water . . . . .	66
6.3	Self-propulsion Simulations in Regular Head Waves . . . . .	69
6.3.1	Assessment of Regular Waves in 2D . . . . .	69
6.3.2	Results of the Simulations . . . . .	71
6.4	Propulsive Coefficients in Waves . . . . .	85
<b>7</b>	<b>Discussion of the Results</b>	<b>88</b>
7.1	Discussion of the Results in Full Scale . . . . .	88
7.2	Discussion of the Results in Model Scale . . . . .	94
7.3	Comparative Analysis of the Results in Full and Model Scale . . . . .	100
<b>8</b>	<b>Conclusions and Future Work</b>	<b>104</b>
8.1	Conclusions . . . . .	104
8.2	Scientific Contributions . . . . .	106
8.3	Future Work . . . . .	108
	<b>List of Figures</b>	<b>123</b>
	<b>List of Tables</b>	<b>124</b>
	<b>Abbreviations</b>	<b>125</b>
	<b>List of Publications</b>	<b>127</b>
	<b>Curriculum Vitae</b>	<b>130</b>

# 1 INTRODUCTION

Three decades ago, a gradual shift from experimental to numerical investigations of ship hydrodynamics has transformed the process of initial ship design. Nowadays, designers are able to evaluate and verify different design prototypes using state-of-the-art computational tools with much lower costs than using experimental setups in specialized facilities. The main hydrodynamic aspects investigated within the ship design are ship resistance, propulsion, seakeeping and cavitation inception. Appropriate numerical tools for accurate assessment of the mentioned are almost exclusively based on Reynolds-Averaged Navier-Stokes (RANS) equations within the vast area of Computational Fluid Dynamics (CFD). Seakeeping assessments typically involve a significant computational burden when performed using CFD, so potential flow tools are often employed despite their well-known limitations.

RANS framework has positioned itself as a first choice for numerical investigation of resistance and propulsion of ships, as it offers a reasonable ratio of computational resources and result accuracy. Given the increasing importance of environmental aspects in maritime transport, ship designers are faced with a unique design challenges characterized by a disproportional relationship between competing objectives. On the one hand, efforts are directed toward minimizing the total energy consumption for achieving desired speed, i.e., *reducing* ship resistance. On the other hand, efforts focus on maximizing the efficiency of propulsion systems that drive the ship forward i.e., *increasing* propulsion efficiency. This mutually dependent energy system, ship resistance and propulsion, come with a great deal of complexity in their prediction. Therefore, most of the studies on the matter are based on ideal, simplified conditions in calm water and zero wind speed.

However, computational tools and the increasing availability of High-Performance Computing (HPC) facilities have enabled to study ship resistance and propulsion in realistic environments. Accurate prediction of ship's added resistance in waves, a second-order force exhibited due to periodic interactions between ship's hull and incoming wave, has increased substantially in the last two decades. Opposed to this, ship propulsion prediction has in many ways been more restricted to experimental approaches rather than numerical ones. Main reason for this is the difficulty of numerically capturing high speed flows and corresponding phenomena characteristic for ship propellers while at the same

time trying to enforce a free surface flow, i.e., modelling of the sea surface. In some specific cases, free surface flow can be neglected in ship propulsion assessment.

For example, ship operating at a lower Froude number where the viscous part of the resistance strongly dominates over the pressure component arising from wave-making resistance. This condition, combined with sufficient propeller immersion such that the free surface effects are negligible, enables the use of double-body calculations in preliminary ship design. This approach is however, more common for performing full-scale assessment of the viscous resistance, bypassing the issue of skin friction line approximations. Nevertheless, propulsion assessments in seaways require complex numerical methods that are able to model accurately ship dynamics, propulsion integral quantities (thrust and torque) and hull-propeller interactions in order to provide a comprehensive understanding. In the light of the ecological aspects mentioned earlier, a logical consequence of having a solid understanding of ship performance in seaway is indeed reduced fuel consumption which is tied directly to the lower harmful Greenhouse Gas (GHG) emissions. Ship propulsion systems in realistic environmental conditions should ideally be treated comprehensively, including engine dynamics and control systems. Nevertheless, the hydrodynamic aspects of ship propulsion in seaways, which constitute the core of this work, represent a crucial element of the overall system performance.

In this thesis, main research objective is to quantify different numerical modelling approaches of ship propulsion and their specific performance in waves. The adopted numerical methodology is based entirely on viscous, turbulent flow implemented in an open-source code OpenFOAM. Within the thesis, two numerical models are developed. First model, based on the Actuator Disk (AD), represents a simplified and idealized model of a ship propeller. The model neglects actual propeller geometry, converting it into a volumetric disk, in which the thrust and torque are distributed based on the Goldstein optimum concept. Second numerical model is based on a full spatial discretization of the propeller geometry where the motion of the propeller is coupled with ship rigid body dynamics through Arbitrary Mesh Interface (AMI) numerical interpolation. Due to the coupling between sliding mesh and rigid body dynamics, the model is tagged with an abbreviation Coupled Sliding Mesh (CSM). The relationship between accuracy and computational load in these two models offer a comprehensive and versatile modelling of ship propulsion; AD model, with its main advantage of being computationally fast,

opposed to the CSM that is inherently restricted with lower maximum time-step due to differing ship flow and propeller time scales, thus yielding higher Central Processing Unit (CPU) costs.

## 1.1 Literature Review

This chapter provides an extensive review of the numerical modelling of ship propulsion within the framework of CFD. It is, however, appropriate to begin with a general overview of the use of RANS approach for ship hydrodynamics, which have served as the foundation for most contemporary CFD studies in naval architecture. The pioneering application of RANS to ship flows was presented by Stern et al. (1988), who introduced a viscous flow approach to capture hull-propeller interactions more realistically than potential flow methods. A few years later, (Tahara and Stern, 1996) developed an approach for predicting ship boundary layers and wake characteristics, establishing an important basis for later propulsion and resistance studies. Subsequently, Hino (1997) performed a comprehensive comparison of different RANS-based formulations, highlighting the sensitivity of flow predictions to turbulence closure models and numerical schemes. Further refinements of turbulence modelling were introduced in early implementations by Deng et al. (2005), improving predictive capability in separated and vortical flows. RANS applications in ship hydrodynamics have grown substantially over the past two decades. For ship propulsion specifically, the focus of this work, several modelling approaches exist within the RANS framework.

The simplest method within RANS is to mimic the propeller thrust and torque by virtual forces without the presence of propeller blades. Such methods belong to the category of Body Force methods, also known as Actuator Disk (AD) or Virtual Disk methods. The main idea of the method is to somewhat accurately distribute the forces in the propeller region, as it is reasonable to assume that the distribution is to be similar for different type of propellers. This similarity has been investigated almost a century ago by Goldstein (1929) and it has prevailed as a standard model within the mentioned group methods. Wang et al. (2023) tried to improve this approach for ducted propellers. In the Finite Volume Method (FVM) framework, additional forces are traditionally modelled as a volumetric source terms on the right-hand side of the momentum equation. In the Naval Hydro Pack (Jasak et al., 2019), an advanced CFD software developed for ship

hydrodynamics (Vukčević et al., 2017b; Gatin et al., 2017), forces are modelled as a boundary condition on a selected control volumes.

Some of the earliest work using AD method for propeller action in a simple maneuvering conditions has been presented by Simonsen and Stern (2005). Different types of AD models have been extensively investigated by Villa and Gaggero (2012) who compared traditional actuator disk approaches with a viscous-inviscid coupled method that combines RANS for hull flow with an unsteady panel method for propeller hydrodynamics. In the literature, the application of the AD method is predominantly investigated under calm water conditions, with limited studies addressing its performance in wave conditions.

(Bakica et al., 2020) investigated loadings in regular waves on an Energy Saving Device (ESD) while utilizing actuator disk for propeller action. Also, thrust losses are reported with ship being appended with ESD but without comparison with experimental data. Recently, (Đurasević et al., 2024) investigates a newly developed, partially rotating grid method for ship propulsion on an Office of Naval Research Tumblehome (ONRT) hull. In their work, the newly developed method outperforms AD in maneuvering condition while being unexplored in wave conditions. The most comprehensive and relevant study is done by Yu et al. (2023) in which three types of their in-house AD models are investigated in calm water and waves against a fully discretized propeller using overset approach. Their finding suggests the applied AD model can successfully predict speed loss in regular head waves but without any notion on the hull-propeller interaction in waves and validation with experimental data. Furthermore, the current AD model implemented within the framework of this thesis is conceptually different from the aforementioned study.

Moreover, the  $\lambda/L_{PP}$  ratio reported in the referenced study differs significantly from the ratios adopted in the present work, as values below 0.5 are considerably more probable for ships of this length. Therefore, a research gap is identified, with AD propulsion method based on corrective velocity and its effect on hull-propeller interactions being unexplored in realistic environments, both in model and full scale. In general, AD methods have proven valuable for accurate predictions of integral values in ship propulsion, which are in most cases, sufficient for successful powering predictions in ship design. Main limitation of this method is the loss of local flow features upstream and downstream of the propeller. This can be crucial for accurate hull-propeller interaction assessment, or, for example, when evaluating hydrodynamic performance on an ESD (Đurasević et al.,

2023). Although the AD method has demonstrated strong performance for predicting integral propulsion quantities in steady and calm water conditions, its behavior under unsteady, wave-induced environments remains insufficiently investigated. Existing studies that employ AD models in waves are generally limited in scope, often lacking systematic validation against experimental data and without any notion on hull-propeller interaction. It is reasonable to expect that these shortcomings may become even more pronounced in realistic seaways, where large-amplitude ship motions and rapidly varying inflow conditions dominate the propeller hydrodynamics.

To address these open questions, higher-fidelity numerical strategies, such as the CSM approach with a fully resolved propeller geometry provide the means to capture the inherently unsteady and three-dimensional flow phenomena with greater physical accuracy. However, this improvement comes at the cost of substantially higher computational time. The present thesis focuses on a systematic comparison of both modelling strategies, with particular emphasis on their predictive capability in regular wave conditions, where unsteady effects are most significant. Both numerical models are validated against a free-running model experiments to ensure a consistent and physically grounded assessment of their predictive performance.

However, all the propeller modelling developments and their application in waves have exclusively been validated at *model scale*, where experiments provide controlled conditions for comparison. Extending these methods to full-scale applications represents a separate challenge, one that has only recently begun to receive attention. (Ponkratov and Zegos, 2015) and (Jasak et al., 2019) did pioneering work in the context of using CFD for predicting full-scale ship performance in calm water. Lately, the most significant advancement in full-scale CFD application in ship hydrodynamics has been through the Joint Industry Project (JIP) JoRes. As stated on the JoRes website, "the main objective of the project is to join the industry efforts and gather the full set of the ship performance data (model test results, CFD calculations and full-scale measurements) and increase knowledge on the important hull-propeller interaction effects to better understand the ship efficiency potential".

Several benchmark cases have been established, for which some of the results can be seen in (Lopes et al., 2025) and (Krasilnikov et al., 2023). One of the benchmark cases even served as a set of guidelines for simulating full-scale CFD in calm water,

proposed by Huang et al. (2023). Also, (Mikulec and Piehl, 2023) performed extensive Verification&Validation studies on predicting power for a full-scale research vessel. These studies demonstrate that full-scale CFD has reached a reasonable level of maturity for calm water applications, though validation in waves remains incredibly limited. The challenge of validating simulations in waves at full scale lies in obtaining reliable experimental data, since the onboard measurements face considerable uncertainty due to uncontrolled sea states, weather variations, and operational conditions.

Regarding the literature on full-scale simulations in waves, the sources are very scarce. (Shenwei et al., 2025) simulated a full-scale free-running ship in head waves but without validating the results. Orihara and Tsujimoto (2018) validated full-scale ship performance predictions in actual seas through on-board monitoring of a large bulk carrier. Their predictions were based on model basin tests and the Resistance and Thrust Identity Method (RTIM) method, combined with theoretical calculations for environmental effects.

While their work successfully validated traditional prediction methods against full-scale data, CFD simulations were not employed in their study. Most recently, Orych et al. (2023) developed a hybrid prediction method combining unsteady potential flow for added resistance with steady RANS coupled to body force propeller models for full-scale self-propulsion in waves. While they achieved reasonable agreement with extrapolated performance from ITTC 1978 data and statistical databases, their approach has two critical limitations that define the present research gap. Firstly, they had no direct full-scale validation data in waves, relying entirely on model-scale extrapolation and statistical comparisons rather than onboard measurements from the actual ship. Secondly, their steady-state coupling approach adds wave resistance as a constant external force rather than resolving the fully coupled unsteady hull-propeller interactions in waves.

The lack of full scale CFD studies in waves, validated against high-quality onboard measurements, therefore represents a critical gap in understanding actual operational performance. In summary, while full-scale CFD validation in calm water has matured through initiatives like the JoRes consortium, and methods for performance prediction in waves have been proposed using hybrid approaches and validated against onboard integral measurements, a critical validation gap remains: existing full-scale CFD simulations in waves have not been benchmarked against high-quality onboard measurements that include both integral performance metrics and hull-propeller interactions. This gap prevents

assessment of whether simplified propulsion models such as AD adequately capture propeller behavior under realistic operational conditions. Understanding the fidelity and limitations of these computationally efficient models against actual measurements is critical for their reliable application in performance prediction and design optimization.

## 1.2 Objectives and Main Hypotheses

The main motivation of this thesis lies in the development and systematic assessment of two distinct numerical propulsion models within the OpenFOAM environment, with a particular focus on their performance in wave conditions. The accurate numerical representation of propeller action in unsteady environments remains a critical challenge in computational ship hydrodynamics, as the coupling between ship motions, incoming waves, and propeller-induced flow fields introduces strong temporal and spatial variability. The first propulsion model, based on the Actuator Disk (AD) theory, provides a computationally efficient approach for representing propeller action through distributed body forces without explicitly resolving propeller blade geometry. Despite its widespread use in steady-state and calm-water simulations, its predictive accuracy in unsteady wave environments has not yet been systematically investigated.

Addressing the limitations of AD with thorough validation further expands the understanding of simplified propeller modelling within CFD. Therefore, the first objective of this thesis is to examine the performance and limitations of the AD model in waves. This effort represents a meaningful contribution to the field, as it provides new insights into the applicability and accuracy of simplified propulsion models under realistic seaway conditions. The second propulsion model, the CSM approach, explicitly resolves the propeller geometry and its unsteady interaction with the surrounding flow. Its implementation within the OpenFOAM libraries represents a significant methodological improvement for ship hydrodynamics simulations, enabling high-fidelity predictions of hull-propeller interactions and transient loading in waves.

The second objective of this thesis is to establish and validate this coupled CSM model as a high-resolution numerical tool for propulsion analysis in unsteady flow conditions. Considering full-scale applications, the current state-of-the-art in computational ship hydrodynamics remains largely confined to calm water analyses, with limited evidence on the performance of propulsion models under realistic sea states. Thus, an additional

objective of this thesis is the extension and validation of the AD model for a full-scale containership, supported by systematic comparison with high-quality onboard measurements. Strong emphasis is placed on the experimental validation of both propulsion models using data from model and full scale sources to ensure their physical reliability and practical relevance. The full-scale data in this thesis offers a unique possibility for comparison with CFD solutions, whereas the model-scale data offers more robust option for validating propulsion models due to its lower experimental uncertainty. Based on these objectives, two primary research hypotheses are formulated:

The first hypothesis reads:

*An actuator disk method with corrective velocity term can accurately predict integral propulsion characteristics (thrust, torque, and power) of full-scale ships operating in representative sea states.*

The second hypothesis is formulated as:

*The accuracy of actuator disk method in capturing unsteady propeller loading and hull-propeller interaction deteriorates with increasing sea-state severity. In contrast, propeller-resolved modelling retains predictive fidelity under such conditions, although at significantly higher computational expense.*

### 1.3 Organization of the Thesis

Based on the research objectives outlined in the previous subchapter, this thesis comprises seven main chapters, whose structure and content are outlined below. In Chapter 1, a literature review is given, indicating the associated research gaps. Following the literature review, the main objectives and hypotheses of this thesis are presented. Since the core of this thesis is based on numerical modelling of fluid flows, applied mathematical model and discretization method is given in Chapter 2.

Chapter 3 presents the two numerical propulsion models developed within the OpenFOAM framework: the Actuator Disk (AD) model and the Coupled Sliding Mesh (CSM) model, detailing their mathematical formulations and implementation specifics. Chapter 4 establishes the theoretical framework for propulsive coefficients, including their definitions, physical interpretations, and the methodology for their estimation in wave conditions. The full-scale application is presented in Chapter 5, which begins with onboard measurements from a Post-Panamax containership, followed by open water propeller simulations, sea trial simulations, and concludes with simulations in a representative sea state with comprehensive validation against measurements.

Chapter 6 covers the model scale investigation, presenting experimental data from the Duisburg Test Case (DTC) containership model, self-propulsion simulations in calm water, self-propulsion simulations in regular head waves, and propulsive coefficient analysis. Chapter 7 provides a thorough discussion of results from both scales, including a comparative analysis between full and model scale findings. Finally, Chapter 8 presents conclusions and scientific contributions drawn from the research. Also, directions for future work are outlined. The thesis concludes with a list of abbreviations, lists of figures and tables, list of publications and Curriculum Vitae.

## 2 NUMERICAL MODEL OF FLUID FLOW

Modelling and predicting fluid flows encompasses certain physical phenomena that are still not fully understood. Therefore, a whole range of approximations in the model are necessary in order to yield satisfactory results in a reasonable time frame. In the context of modelling flows in ship hydrodynamics, an incompressible, isothermal, multiphase flow model with the fluid considered as a Newtonian, is in most cases considered acceptable.

However, compressibility effects should be considered in the evaluation of slamming loads, as stressed in (Gatin et al., 2020). For capturing turbulent characteristics of the flow, additional approximations in the numerical model are needed. Several levels of modelling turbulent fluctuations in the fluid have been developed over the years, where Navier-Stokes equations followed by the concept of Reynolds averaging have been the dominant numerical model for problems in ship and offshore hydrodynamics.

This chapter is dedicated to the numerical model used in this thesis, which is, in its core, based on the RANS equations. Mathematical model is followed by its appropriate numerical discretization using the FVM. The mathematical model is implemented in an open-source CFD toolbox, OpenFOAM. For the details of the toolbox, reader is referred to (Weller et al., 1998). In the code, through object-oriented paradigms, partial differential equations are reliably implemented, as seen in (Jasak, 2009).

### 2.1 Mathematical Model

The governing equations describing the mathematical model of the fluid flow are briefly described in this subchapter. As the numerical model in the thesis assumes multiphase (water and air) flow combined with moving, dynamic mesh, equations are outlined correspondingly. Among governing equations, RANS procedure for mathematically capturing turbulent flow with chosen turbulence model is depicted.

#### 2.1.1 Governing Equations

The continuity equation, considering constant density reads:

$$\nabla \cdot \mathbf{u}_r = 0 \tag{1}$$

where the  $\mathbf{u}_r$  term accounts for relative fluid velocity to mesh points velocity. The momentum equation, or the Navier-Stokes equation is defined as:

$$\frac{\partial \mathbf{u}}{\partial t} + \nabla \cdot (\mathbf{u}_r \mathbf{u}) - \nabla \cdot (\nu_e \nabla \mathbf{u}) = -\frac{1}{\rho(\alpha)} \nabla p + \mathbf{g}, \quad \mathbf{x} \in \Omega(t) \quad (2)$$

The local fluid velocity field  $\mathbf{u}$  is decomposed into mean and fluctuating components, forming the essence of RANS concept. The equation's left-hand side comprises three distinct terms: temporal acceleration  $\frac{\partial \mathbf{u}}{\partial t}$ , while the second term is the convective acceleration term, adapted for the moving mesh. The last term on the left-hand side is the viscous diffusion term.

On the right-hand side,  $\nabla p$  represents pressure forces in which  $\alpha$  encompasses distinct phase for which the density is evaluated. Gravitational effects are accounted for in  $\mathbf{g}$ . The effective kinematic viscosity is denoted by  $\nu_e$ . As multiphase flow is considered, the interface between air and water is captured using the Volume of Fluid (VOF) methodology, which introduces the phase indicator function  $\alpha$ . This scalar field modifies both the density  $\rho$  and effective kinematic viscosity  $\nu$  for both fluids in the RANS formulation, as shown in Eqs. (3) and (4).

$$\rho = (1 - \alpha)\rho_{\text{air}} + \alpha\rho_{\text{water}} \quad (3)$$

$$\nu = (1 - \alpha)\nu_{\text{air}} + \alpha\nu_{\text{water}} \quad (4)$$

where the indexes "air" and "water" represent the values for corresponding fluids. In order to track the evolving interface between air and water, phase transport equation is needed:

$$\frac{\partial \alpha}{\partial t} + \nabla \cdot (\mathbf{u}_r \alpha) + \nabla \cdot [\mathbf{u}_c \alpha (1 - \alpha)] = 0 \quad (5)$$

where  $\mathbf{u}_c$  stand for artificial compression velocity in order to sharpen the interface between phases. In this work, evaluating interface position is modelled using the concept of isosurfaces, ensuring its sharpness and continuity. The details of the model are thoroughly explained in (Roenby et al., 2016).

Within this thesis, rigid body displacements are taken into account; therefore, the

mesh motion is governed by the time evolution of the mesh point coordinates as:

$$\frac{\partial \mathbf{x}_m}{\partial t} = \mathbf{u}_m, \quad (6)$$

where  $\mathbf{x}_m$  denotes the position vector of the mesh points, and  $\mathbf{u}_m$  represents the corresponding mesh velocity field. To ensure smooth and physically consistent deformation of the computational mesh in response to rigid body motion, a distance-weighted morphing approach is employed. In this method, the displacement of each internal mesh point is obtained by inverse-distance-weighted interpolation of the prescribed motion at the moving-body surface points:

$$\mathbf{x}'_m = \frac{\sum_{i=1}^N w_i(\mathbf{x}_m) \mathbf{T}_i(\mathbf{x}_i)}{\sum_{i=1}^N w_i(\mathbf{x}_m)}, \quad w_i(\mathbf{x}_m) = \frac{1}{|\mathbf{x}_m - \mathbf{x}_i|^p}, \quad (7)$$

where  $\mathbf{T}_i(\mathbf{x}_i)$  denotes the transformed position of boundary point  $i$  after the applied rigid-body translation and rotation, and  $w_i$  are the distance-based weights that decay with increasing distance from the moving surface. Rotational motion is smoothly propagated through the domain using Spherical Linear Interpolation (SLERP) of quaternions, (Shoemake, 1985) which provides a continuous interpolation of orientation between the rigid body and the stationary region. This formulation ensures that the mesh follows the rigid-body motion closely near the surface while gradually attenuating in the far field, thereby preserving mesh quality and preventing excessive distortion.

The outlined governing equations are closed through appropriate turbulence modelling. The Reynolds averaging introduces additional unknown terms representing turbulent fluctuations, which are modelled using turbulence models based on statistical approaches to the Navier-Stokes equations. The following subchapter describes the turbulence modelling framework employed in this work.

### 2.1.2 Turbulent Flow

The RANS equations form the foundation of turbulence modelling in ship hydrodynamics, providing a computationally reasonable approach to simulate the chaotic nature of turbulent flows. Numerous literature on the concept of RANS is available, such as in (Hinze, 1975;

B. Pope, 2000) or (Wilcox, 2006). The instantaneous flow variables are decomposed into mean and fluctuating components through Reynolds averaging, transforming the nonlinear Navier-Stokes equations into a system that describes the averaged flow field while introducing additional unknowns that require turbulence closure models. For the sake of clarity, continuity equation and the Navier-Stokes equations in their differential form read:

$$\frac{\partial u_i}{\partial x_i} = 0 \quad (8)$$

$$\frac{\partial u_i}{\partial t} + \frac{\partial}{\partial x_j}(u_i u_j) = -\frac{1}{\rho} \frac{\partial p}{\partial x_i} + \nu \frac{\partial^2 u_i}{\partial x_j \partial x_j} + g_i \quad (9)$$

where  $u_i$  represents the velocity components in the  $i$ -th direction,  $p$  is the pressure,  $\rho$  is the fluid density,  $\nu$  is the kinematic viscosity, and  $g_i$  denotes the gravitational acceleration components. In the Reynolds averaging approach, each instantaneous flow variable is decomposed into a time-averaged mean component  $\bar{u}_i$  and a fluctuating component  $u'_i$ :

$$u_i = \bar{u}_i + u'_i \quad (10)$$

with analogous nomenclature for time-averaged pressure  $\bar{p}$  and fluctuating part  $p'$ :

$$p = \bar{p} + p' \quad (11)$$

The Reynolds averaging operation is defined as:

$$\bar{f} = \frac{1}{T} \int_0^T f(t) dt \quad (12)$$

Where  $\bar{f}$  represents an instantaneous flow variable while  $T$  is the averaging time interval. Applying the Reynolds decomposition and averaging operation to the instantaneous Navier-Stokes equations yields the RANS equations. The continuity equation becomes:

$$\frac{\partial \bar{u}_i}{\partial x_i} = 0 \quad (13)$$

while the NS equations forms:

$$\frac{\partial \bar{u}_i}{\partial t} + \frac{\partial}{\partial x_j} (\bar{u}_i \bar{u}_j) = -\frac{1}{\rho} \frac{\partial \bar{p}}{\partial x_i} + \nu \frac{\partial^2 \bar{u}_i}{\partial x_j \partial x_j} - \frac{\partial}{\partial x_j} (\overline{u'_i u'_j}) + g_i \quad (14)$$

The term  $-\overline{u'_i u'_j}$  represents the Reynolds stress tensor, which arises from the nonlinear convective terms and embodies the effect of turbulent fluctuations on the mean flow. This additional unknown variables require closure models to achieve a mathematically closed system. The Reynolds stress tensor, usually represented as  $\tau_{ij}^{Re}$ , can be written in symmetric form as:

$$\tau_{ij}^{Re} = -\rho \overline{u'_i u'_j} = \tau_{ji}^{Re} \quad (15)$$

The introduction of these six additional unknowns (in three-dimensional flow) creates the closure problem of turbulence. The RANS momentum equation is commonly expressed as:

$$\frac{\partial \bar{u}_i}{\partial t} + \frac{\partial}{\partial x_j} (\bar{u}_i \bar{u}_j) = -\frac{1}{\rho} \frac{\partial \bar{p}}{\partial x_i} + \frac{\partial}{\partial x_j} \left[ (\nu + \nu_t) \left( \frac{\partial \bar{u}_i}{\partial x_j} + \frac{\partial \bar{u}_j}{\partial x_i} \right) \right] + g_i \quad (16)$$

where  $\nu_t$  is the turbulent or eddy viscosity, introduced through the Boussinesq hypothesis which relates the Reynolds stresses to the mean strain rate tensor. The closure of the RANS equations requires models to determine the turbulent viscosity  $\nu_t$  or directly compute the Reynolds stresses. Turbulence models in ship hydrodynamics can be broadly categorized into several approaches based on their complexity and computational requirements. The Boussinesq hypothesis assumes that the Reynolds stresses are proportional to the mean strain rate:

$$-\overline{u'_i u'_j} = \nu_t \left( \frac{\partial \bar{u}_i}{\partial x_j} + \frac{\partial \bar{u}_j}{\partial x_i} \right) - \frac{2}{3} k \delta_{ij} \quad (17)$$

where  $k = \frac{1}{2} \overline{u'_i u'_i}$  is the turbulent kinetic energy and  $\delta_{ij}$  is the Kronecker delta. Another approach is the Reynolds Stress Model (RSM), where transport equations are directly solved for each component of the Reynolds stress tensor without the Boussinesq hypothesis. Throughout the thesis, in order to achieve consistency in turbulence modelling,  $k-\omega$  SST is applied for achieving closure of the equations (Menter, 1994). Mentioned model is identified as the most versatile for problems in ship hydrodynamics, as noted in a comprehensive overview in Pena and Huang (2021). The primary reason for using the  $k-\omega$  SST is its capability of handling strong pressure gradients and separation of the flow, a phenomena that is present in ship hydrodynamics. Also, it combines near-wall accuracy of  $k-\omega$  along

with the free-stream capability of  $k - \epsilon$  turbulence model (Menter, 1994). The transport equation of the kinetic turbulent energy  $k$  reads:

$$\frac{\partial k}{\partial t} + \nabla \cdot (\mathbf{u}_r k) - \nabla \cdot \left[ \left( \nu + \frac{\nu_t}{\sigma_k} \right) \nabla k \right] = P_k - \beta^* k \omega \quad (18)$$

formulated in a similar manner as Navier-Stokes equation. The left-hand side contains temporal derivatives, followed by a convective and diffusive term respectively. Production of turbulent kinetic energy is denoted as  $P_k$  while the  $-\beta^* k \omega$  stands for dissipative term of the turbulent kinetic energy. The transport equation of the specific dissipation rate  $\omega$  is defined as:

$$\frac{\partial \omega}{\partial t} + \nabla \cdot (\mathbf{u}_r \omega) = \nabla \cdot \left[ \left( \nu + \frac{\nu_t}{\sigma_\omega} \right) \nabla \omega \right] + \alpha \frac{\omega}{k} P_k - \beta \omega^2 + 2(1 - F_1) \frac{\sigma_\omega}{\omega} \nabla k \cdot \nabla \omega \quad (19)$$

Again, following the same principle as a fundamental Navier-Stokes equations. The last, cross-diffusion term in the right-hand side is specific for this model. It activates when the blending function  $F_1$  approaches to zero (in free-stream regions). It helps transition from  $k - \omega$  behavior near walls to  $k - \epsilon$  behavior in the free stream by modifying the diffusion of  $\omega$  based on gradients of both  $k$  and  $\omega$ . Numerically, both variables are discretized and solved using iterative linear solvers, similar to the momentum and phase fraction equations. For the far field boundary conditions, turbulent kinetic energy  $k$  can be calculated as:

$$k = \frac{3}{2} (U_{fs} \cdot I)^2 \quad (20)$$

where  $U_{fs}$  is equal to the free stream velocity (ship initial velocity) while  $I$  is the turbulence intensity. In this work, the turbulence intensity for all calculations is assumed at 4%. (Eça and Hoekstra, 2008) developed guidelines for straightforward calculation of initial conditions of  $\omega$ , suited for ship flows. The guideline proposes equation:

$$\omega = 10 \frac{U_{fs}}{L_{PP}} \quad (21)$$

Another important aspect of modelling turbulent flows in ship hydrodynamics is the treatment of the wall-bounded turbulent flow behaviour. Achieving physically reasonable velocity profile in the proximity of the hull would require extremely dense spatial

discretization, thus increasing the computational costs significantly. This is especially demanding, if not impossible, in full-scale applications. To address this issue, a commonly adopted procedure is the use of wall functions. Using wall functions, the near-wall region is not explicitly solved but is approximated using semi-empirical relationships of the shear stress and velocity gradients (Tu et al., 2018). Consequently, the number of computational cells is lower while the accuracy is maintained. A critical parameter in the application of wall functions is the dimensionless wall distance  $y^+$ , which represents the dimensionless distance of the first mesh point from the rigid wall, normalized by the viscous length scale. The  $y^+$  value is significant because it determines the appropriate treatment of the near-wall flow: for  $y^+$  values in the range of 30 to 300, wall functions are valid, as the first mesh point lies within the logarithmic region of the boundary layer, whereas lower  $y^+$  values require resolving the viscous sub-layer directly. It is therefore necessary to properly select the  $y^+$ , so the wall functions accurately capture the near-wall turbulence and shear stress, crucial for reliable predictions of ship resistance and propeller thrust and torque. In this thesis, appropriate wall functions are employed, complemented by the  $k$ - $\omega$  SST turbulence model.

## 2.2 Discretization of the Mathematical Model

The governing equations presented in subchapter 2.1.1 have no general analytical solution for practical engineering problems. The Navier-Stokes equations form an elliptic system of Partial Differential Equations (PDE) for steady-state flows, while unsteady problems exhibit parabolic character due to the temporal derivative. To obtain numerical solutions, these continuous equations must be transformed into a system of discrete algebraic equations that can be solved iteratively.

### 2.2.1 Integral Formulation and Discretization

The momentum equation Eq. (2) can be rewritten in a more general form suitable for discretization:

$$\frac{\partial \mathbf{u}}{\partial t} + \nabla \cdot (\mathbf{u}_r \mathbf{u}) = \nabla \cdot (\nu_e \nabla \mathbf{u}) - \frac{1}{\rho(\alpha)} \nabla p + \mathbf{g} \quad (22)$$

To transition from this continuous differential form to a discrete algebraic system,

integration over a control volume is required. Integrating Eq. (22) over an arbitrary control volume yields:

$$\int_{V_P} \frac{\partial \mathbf{u}}{\partial t} dV + \int_{V_P} \nabla \cdot (\mathbf{u}_r \mathbf{u}) dV = \int_{V_P} \nabla \cdot (\nu_e \nabla \mathbf{u}) dV - \int_{V_P} \frac{1}{\rho(\alpha)} \nabla p dV + \int_{V_P} \mathbf{g} dV \quad (23)$$

The spatial derivative terms (convection, diffusion, and pressure gradient) can be transformed from volume integrals to surface integrals using Gauss's divergence theorem:

$$\int_{V_P} \nabla \cdot \mathbf{F} dV = \int_{\partial V_P} \mathbf{F} \cdot \mathbf{n} dS = \sum_f \mathbf{F}_f \cdot \mathbf{S}_f \quad (24)$$

where  $\mathbf{F}$  represents any vector field,  $\partial V_P$  denotes the surface enclosing the control volume,  $\mathbf{n}$  is the outward unit normal vector, and the summation extends over all faces  $f$  of the control volume. Applying this theorem to each term in Eq. (23) yields:

$$\begin{aligned} & \int_{V_P} \frac{\partial \mathbf{u}}{\partial t} dV + \sum_f (\mathbf{u}_r \mathbf{u})_f \cdot \mathbf{S}_f \\ &= \sum_f (\nu_e \nabla \mathbf{u})_f \cdot \mathbf{S}_f - \sum_f \left( \frac{p}{\rho(\alpha)} \right)_f \mathbf{S}_f + V_P \mathbf{g} \end{aligned} \quad (25)$$

The temporal term can be approximated using finite differences, Eq. (30), while face values must be interpolated from cell-centered values. This leads to the semi-discrete form:

$$V_P \frac{\mathbf{u}_P^{n+1} - \mathbf{u}_P^n}{\Delta t} + \sum_f (\mathbf{u}_r \mathbf{u})_f \cdot \mathbf{S}_f = \sum_f (\nu_e \nabla \mathbf{u})_f \cdot \mathbf{S}_f - \sum_f \left( \frac{p}{\rho(\alpha)} \right)_f \mathbf{S}_f + V_P \mathbf{g} \quad (26)$$

where superscripts  $n$  and  $n + 1$  denote the current and next time levels, respectively. For steady-state problems, the temporal derivative vanishes. The face fluxes depend on neighboring cell values, which introduces coupling between cells. After applying appropriate interpolation schemes for convection Eq.(31), and diffusion (33) terms, and collecting all contributions, the discretized momentum equation for cell  $P$  can be written in the general form:

$$a_P \mathbf{u}_P = \sum_N a_N \mathbf{u}_N + \mathbf{b}_P \quad (27)$$

where  $a_P$  is the central coefficient,  $a_N$  are the coefficients for neighboring cells  $N$ , and  $\mathbf{b}_P$  contains source terms including the pressure gradient and body forces. Similar discretization is applied to the continuity Eq. (1), turbulence transport Eqs. (18), (19), and phase fraction (5). The complete set of discretized equations for all cells and all transport variables forms a large system of coupled algebraic equations:

$$[A][x] = [b] \quad (28)$$

where  $[A]$  is a sparse coefficient matrix of dimension  $N \times N$  (with  $N$  being the total number of cells),  $[x]$  is the solution vector containing the unknown field values at all cell centers, and  $[b]$  is the source vector. The sparsity of  $[A]$  arises from the local nature of the discretization, each cell is directly coupled only to its immediate neighbors.

### 2.2.2 Finite Volume Method Framework

Among the available numerical approaches for discretizing partial differential equations, the Finite Volume Method (FVM) has become the most common discretization method in CFD for ship hydrodynamics. Its formulation is based on integral conservation laws applied over discrete control volumes, ensuring strict local and global conservation of mass, momentum, and energy. This conservative nature makes FVM particularly robust for handling complex geometries and boundary conditions typical ship hydrodynamic flows. The spatial and temporal discretization accuracy can be systematically improved by refining the mesh or increasing the order of interpolation schemes, allowing a balance between computational cost and numerical fidelity.

The discretization process within FVM involves three main components:

- Spatial discretization (computational mesh generation)
- Discretization of equations (selection of numerical schemes)
- Solution of the discretized system (linear solvers and algorithms)

Given the extensive literature on this topic (Ferziger and Perić, 2002; Versteeg and Malalasekera, 2007), a detailed derivation of FVM is omitted. Instead, the essential concepts relevant to the present work are highlighted. Figure 1 illustrates a generic polyhedral control volume used in the discretization.

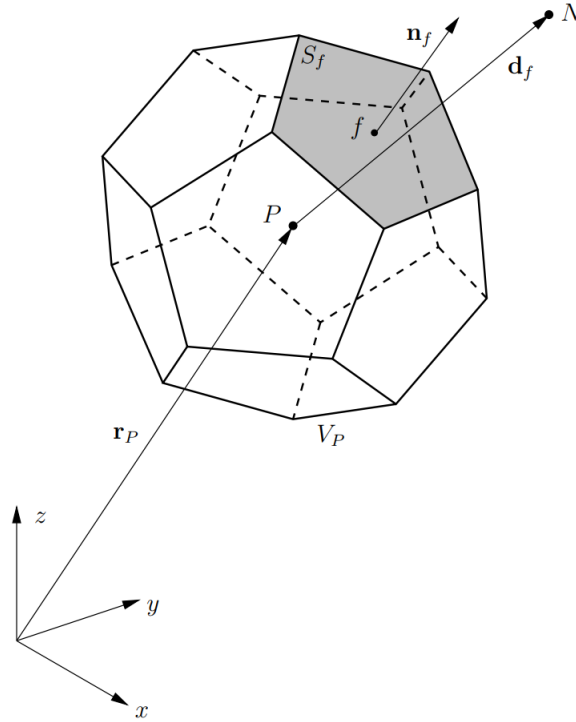


Figure 1: Polyhedral control volume with geometric notation

The fundamental requirements of FVM are that control volumes must neither overlap nor leave gaps, ensuring complete coverage of the computational domain. Point  $P$  denotes the cell center, while  $N$  represents the center of a neighboring cell. The vector  $\mathbf{d}_f$  connects these centers,  $S_f$  is the face area, and  $\mathbf{n}_f$  is the outward-pointing unit normal at face center  $f$ . For polyhedral cells with non-planar faces, each face is decomposed into triangles (Tuković, 2005). The total face area is computed as:

$$S_f = \sum_{t=1}^{N_t} S_t \quad (29)$$

where  $S_t$  is the area of triangle  $t$ , and  $N_t$  is the number of triangles composing the face. This decomposition is essential for accurate flux calculations across arbitrary polyhedral faces, as required by Gauss's theorem, Eq.(24).

### 2.2.3 Discretization Schemes

The transformation from the integral form, Eq.(25) to the algebraic system, Eq.(28), requires specification of interpolation and approximation schemes for each term. A wide variety of discretization schemes have been developed over the years (Jasak, 1996); only those employed in this thesis are described here.

**Temporal discretization:** For calm water simulations, a first-order Euler scheme is used. For simulations involving wave propagation in the domain, a second-order backward method is employed, thus reducing the numerical diffusion that is detrimental for achieving the targeting wave characteristics (Sulovsky et al., 2023b):

$$\frac{\partial \phi}{\partial t} \approx \begin{cases} \frac{\phi^{n+1} - \phi^n}{\Delta t} & \text{First-order Euler} \\ \frac{3\phi^{n+1} - 4\phi^n + \phi^{n-1}}{2\Delta t} & \text{Second-order backward} \end{cases} \quad (30)$$

A scalar field quantity is denoted as  $\phi$ . The Euler scheme uses two consecutive time-steps ( $n$  and  $n + 1$ ) which offers simplicity but yields lower accuracy. The second-order Backward scheme uses three time-steps ( $n - 1$ ,  $n$ , and  $n + 1$ ), providing higher accuracy by simply taking into account more temporal information. The drawback of this method is that it does not guarantee boundedness of the solution which can, in some cases, introduce spurious oscillations.

**Convective term discretization:** For all simulations, convective term is discretized using a linear upwind scheme with explicit gradient correction:

$$\sum_f [\phi_P + (\nabla \phi)_P \cdot \mathbf{d}_f] (\rho \mathbf{u})_f \cdot \mathbf{S}_f \quad (31)$$

where  $(\nabla \phi)_P$  is the gradient at cell center P. Gradients are computed using the Gauss linear scheme without limiters, which applies linear interpolation of cell-centered values to faces:

$$(\nabla \phi)_P = \frac{1}{V_P} \sum_f \phi_f \mathbf{S}_f \quad (32)$$

**Diffusion term discretization:** The diffusion term is discretized using a linear scheme with Gauss integration:

$$\int_{V_P} \nabla \cdot (\nu_e \nabla \mathbf{u}) dV = \sum_f (\nu_e)_f (\nabla \mathbf{u})_f \cdot \mathbf{S}_f \quad (33)$$

where the right-hand side represents discrete face summations of the diffusive fluxes, accounting for both normal and shear stress components.

**Turbulence transport variables:** Turbulence transport variables,  $k$  and  $\omega$  are discretized using a first-order upwind scheme:

$$\int_{V_P} \nabla \cdot (\rho \phi) dV = \sum_f \phi_{up}(\rho)_f \cdot \mathbf{S}_f \quad (34)$$

where  $\phi_{up}$  represents the upwind interpolated value.

**Phase fraction transport:** The convective term in the phase fraction transport, Eq. (5), van Leer scheme with compression for sharp interface capturing is used.

$$\nabla \cdot (\mathbf{u}_c \alpha) = \sum_f \alpha_f \phi_f \quad (35)$$

While the relative velocity flux  $\phi_{rb}$  is discretized using linear interpolation. For full details see (Rusche, 2002).

$$\nabla \cdot (\mathbf{u}_r \alpha) = \sum_f \alpha_f \phi_{rb,f} \quad (36)$$

**Laplacian terms and surface gradients:** Laplacian terms are discretized using Gauss linear scheme with correction for non-orthogonality. Interpolations between cell centers to face values is set to linear. Surface normal gradients are discretized using the corrected scheme that reads:

$$(\nabla \phi)_f \cdot \mathbf{n} = \frac{\phi_N - \phi_P}{|\mathbf{d}_f|} + \mathbf{k} \cdot (\nabla \phi)_f \quad (37)$$

where the correction term  $\mathbf{k}$  accounts for mesh non-orthogonality. The implementation of these numerical schemes in OpenFOAM is highly polymorphic, using runtime dictionaries.

#### 2.2.4 Solution of the Algebraic System

The solution methodology for the discretized system is briefly outlined her. Detailed descriptions of iterative solvers and preconditioning techniques are beyond the scope of this thesis and can be found in literature (Yousef, 2003; Jasak and Uroić, 2020). The mentioned discretization schemes set up a system of algebraic equations in a form given by in Eq.(2) and Eq.(28), where  $[A]$  is a sparse coefficient matrix,  $[b]$  is the source vector and  $[x]$  is the solution vector. For a mesh with  $N$  number of cells,  $A$  yields an  $N \times N$  matrix size, ready for solving.

The preliminary pressure correction is computed by the Preconditioned Conjugate Gradient (PCG) solver with Diagonal Incomplete Cholesky (DIC) preconditioning while

the pressure equation is solved using a Preconditioned BiConjugate Gradient Stabilized (PBiCGStab) solver, also with DIC preconditioning. Both pressure solvers are configured with an absolute and relative tolerance of  $10^{-6}$  and  $10^{-3}$  respectively, thus ensuring minimal influence of iterative errors. Velocity and turbulence quantities are solved using a symmetric Gauss-Seidel smoothing solver. Regarding the pressure-velocity coupling, for full-scale computations, three outer correction loops are employed with two inner correction loops and one non-orthogonal correction. In model-scale, two outer correction loops proved sufficient. For the fundamentals of pressure-velocity coupling within CFD, reader is referred to (Patankar and Spalding, 1972).

Having established the numerical framework, following chapter presents the implementation of propulsion models in OpenFOAM environment.

### 3 NUMERICAL PROPULSION MODELS IN OPENFOAM

This chapter is dedicated to the propulsion models that are implemented and used in this thesis. Firstly, an overview of the numerical model based on the Actuator Disk (AD) theory is given. The overview comprises of the main equations and specific numerical implementation. The second model is based on a sliding mesh approach with propeller geometry being fully resolved. The main improvement of the approach from the standard OpenFOAM implementation is coupling between propeller rotation with a rigid body motion of the ship hull while using the advantages of the AMI. For both models a pseudo-code is provided in order to ease the understanding of the numerical implementation in OpenFOAM environment.

#### 3.1 Actuator Disk (AD) Model

In this subchapter, an overview of using Actuator Disk (AD) model for ship propulsion assessments along with the details of the implemented AD model within OpenFOAM framework is depicted. The core idea of an AD is replacing the actual geometry of the blades with an idealized cylinder or a plane, upon which integral values of thrust and torque are imposed. The application of AD models in engineering range from wind turbine modelling, aviation, ship propulsion or Heating, Ventilation and Air Conditioning (HVAC) systems. Within computational ship hydrodynamics, using AD model has gained increased popularity due to dramatic reductions in computational overhead opposed to resolved propeller geometry simulations. However, the accuracy in the local flow field upstream and downstream of the propeller plane is somewhat reduced. For determining hull-propeller interaction in a preliminary design stage, this methodology proved to be accurate enough. In this work, AD model is based on a Goldstein optimum distribution of thrust and torque in the propeller plane, where the distributions are represented in a classical, dimensionless manner. Thrust coefficient  $K_T$  and torque coefficient  $K_Q$  read:

$$K_T = \frac{T}{\rho n^2 D^4} \quad (38)$$

$$K_Q = \frac{Q}{\rho n^2 D^5} \quad (39)$$

Propeller thrust is denoted as  $T$  and torque as  $Q$ . The diameter of the propeller is  $D$  while  $n$  is the propeller revolution rate. Fluid density is denoted as  $\rho$ . The advance coefficient  $J$  reads:

$$J = \frac{V_A}{nD} \quad (40)$$

where  $V_A$  is the incoming velocity into the propeller plane. The distribution of axial forces in the propeller plane is defined as:

$$F_{axial} = r' \sqrt{1 - r'^2} \quad (41)$$

while the distribution of tangential forces reads:

$$F_{tangential} = \frac{r' \sqrt{1 - r'^2}}{r'(1 - r_h) + r_h} \quad (42)$$

A non-dimensional radius  $r'$  is defined as:

$$r' = \frac{|R| - r_h}{r - r_h} \quad (43)$$

$|R|$  is the vector from the propeller origin up to the cell centroid, denoted as in absolute scalar value. Propeller radius is  $r$  and hub radius is  $r_h$ . The sampling of the fluid velocity is done in the cells of the enclosed AD volume using OpenFOAM embedded *cellZone* mesh manipulations. For accurate prediction of the effective wake, a corrective term for the incoming velocity is implemented as:

$$V_A = V_{AD} - \frac{T}{2\rho A_D V_{AD}} \quad (44)$$

where  $V_{AD}$  is the sampled velocity within the AD computational cells while the second term on the right-hand side is the correction for suction effect of the propeller. Surface area of the propeller is denoted as  $A_D$ . The implementation of the corrective term is the same as in (Bakica et al., 2019) with the main difference of the current AD model being implemented as a source term utilizing standardized `fvOptions` framework in OpenFOAM; a collection of run-time selectable options used to manipulate governing equations in solvers by adding

sources, sinks, imposing constraints, or applying corrections. The model is coupled with the `sixDoFRigidBodyMotion` OpenFOAM library in order to update the propeller origin and axis of rotation to match the current position of the ship. The related pressure jump in the AD cells is automatically computed through pressure-velocity coupling inside the PIMPLE algorithm.

Mentioned algorithm is a well-established coupling that relies both on Semi-Implicit Method for Pressure Linked Equations (SIMPLE) and Pressure-Implicit with Splitting of Operators (PISO) procedures within CFD. Hence, at least two outer correctors were needed in order to achieve convergence of the advance velocity. Typical mesh topology for the AD model is shown in Figure 2. Computational cells replacing the propeller geometry are embedded within yellow cylinder. As the value of the averaged inflow velocity into the disk is crucial for the accuracy, refinement of the mesh needs to be sufficient, particularly upstream of the disk.

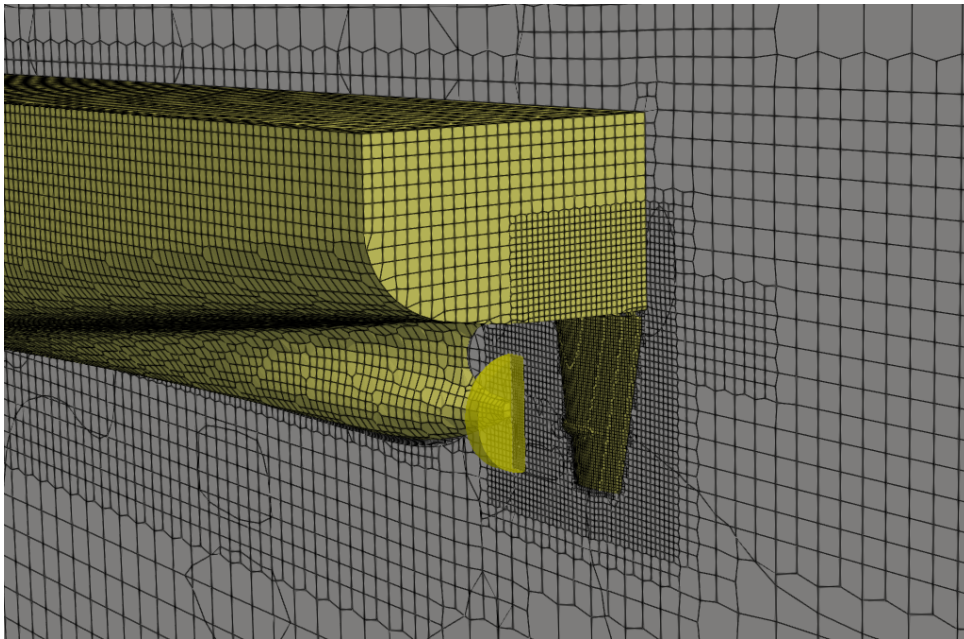


Figure 2: Typical mesh topology in self-propulsion simulations with AD

Within the C++ object-oriented framework, the implemented AD model is realized as a dedicated class named `actuatorDiskPropeller`. The class requires the user to define key parameters such as the propeller radius  $R$ , hub radius  $r_h$ , propeller axis orientation, and origin coordinates, as well as the corresponding open water performance data. To ensure numerical stability during initialization, the activation time of the AD model is also specified by the user as an arbitrary input parameter.

The computational workflow of the AD model within a single time step is depicted in Figure 3.

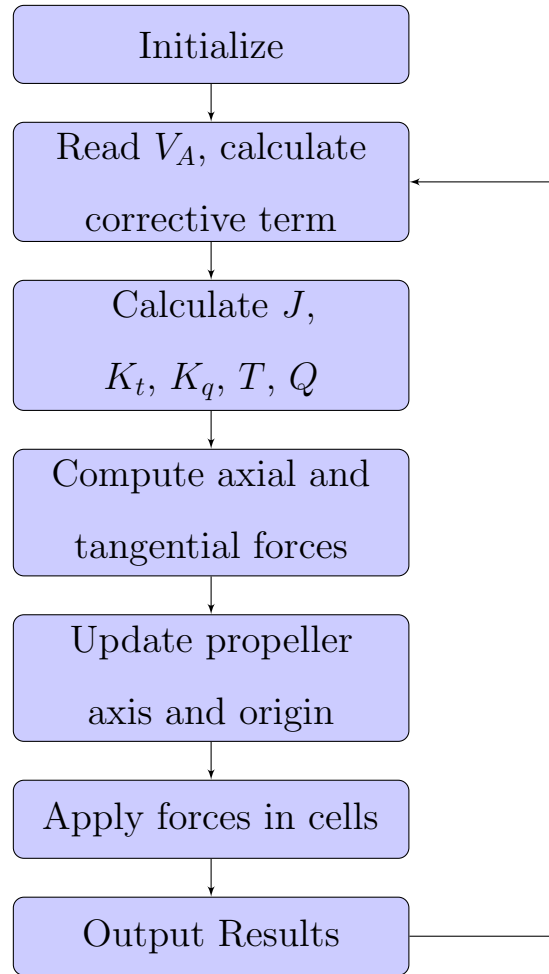


Figure 3: Computational workflow of the AD model

The main disadvantage of this numerical model is the fact that the propeller revolution rate is set constant under every circumstances. Adaptive revolution rate of the propeller would insist on matching the provided thrust with measured total resistance of the ship. In this way, self-propulsion point along with comprehensive assessment of propulsive efficiency could be obtained from a single run. Furthermore, the explicit requirement for open water data within the `actuatorDiskPropeller` class presents a minor limitation, as open water curves are not always available, particularly at full-scale.

The overall algorithmic structure of the implemented AD model is given as a pseudocode in Algorithm 1. The computed results are stored in a text-based format, thereby enabling straightforward post-processing and further analysis.

---

**Algorithm 1** actuatorDiskPropeller class

---

**Require:** radius  $r$ , hub radius  $r_h$ , disk thickness, propeller axis and origin, open water data

```

1: for each timestep do
2:   Calculate reference velocity  $V_{AD}$ 
3:   Update disk orientation and origin if rigid body motion enabled
4:   for each mesh cell do
5:     Calculate projection on disk axis
6:     if cell within disk thickness then
7:       Compute projection on disk plane
8:       Calculate current radius  $r_{curr}$ 
9:       if  $r_h \leq r_{curr} \leq r$  then
10:        Store cell index and radius
11:        Calculate scaled radius:  $r_{scaled} = \frac{r_{curr}/r - r_h/r}{1 - r_h/r}$ 
12:        Accumulate axial force volume:  $v_{FA+} = r_{scaled}\sqrt{1 - r_{scaled}}V_{cell}$ 
13:        Accumulate tangential force volume:  $v_{FT+} = \frac{r_{scaled}\sqrt{1 - r_{scaled}}}{r_{scaled}(1 - r_h) + r_h}V_{cell}r_{curr}$ 
14:       end if
15:     end if
16:   end for
17:   Calculate advance ratio:  $J = \frac{|V_{AD}|}{nD}$ 
18:   Calculate induced velocity correction and update  $J$ 
19:   Read  $K_T$ ,  $K_Q$  from open water data
20:   Calculate thrust  $T$  and torque  $Q$ 
21:   for each cell inside disk do
22:     Calculate axial and tangential force distributions
23:     Apply forces to momentum equation source term
24:   end for
25: end for

```

---

## 3.2 Coupled Sliding Mesh (CSM) Model

This subchapter describes the coupled sliding mesh model for hydrodynamic simulations utilizing both rigid body motions and discretized propeller rotation. Ali et al. (2024) recently presented a similar numerical approach for hull-propeller interaction. However, their work primarily focuses on results rather than numerical implementation details. This limits the ability to independently validate or reproduce their methodology. In contrast, the present work aims to discuss in detail the numerical implementation and coding challenges.

The main motivation for this numerical model is to avoid using overset mesh methodology which is based on volumetric interpolations of fields, opposing to the face-based interpolations that sliding mesh offers. Volumetric interpolations, as indicated in (Lemaire et al., 2023), are highly sensitive to the chosen interpolation procedure. Low-order interpolation scheme seem to cause mass imbalances within the domain which can have profound effects on the accuracy and validity of the simulations. High-order schemes perform slightly better, producing a smoother fields, but are still prone to errors. Also, using overset mesh will inherently require significantly higher cell count. The usage of overset methodology is in some sense required when the geometries are complex and AMI interfaces are difficult to obtain.

In this work, a numerical model is implemented that couples deforming mesh strategy along with prescribed rotation of the chosen cell zone. In that manner, high-fidelity propulsion assessments in waves are possible without strictly using overset approach. In order to understand the numerical model, it is necessary to briefly explain some of the existing classes in OpenFOAM that the model relies on. Within the `sixDoFRigidBodyMotion` class, a subclass `sixDoFRigidBodyMotionSolver` is responsible for applying point displacement on the mesh based on calculated forces on rigid bodies. The class uses a vector field `pointDisplacement` which stores new point positions of the mesh based on calculated displacements.

Therefore, the implementation of the CSM model is relying on the existing vector field used in simulations with dynamic meshes. The model is implemented in the `solve` function of the `sixDoFRigidBodyMotionSolver` class. The algorithm of the CSM model is given as a pseudocode in algorithm 2. The depicted algorithm workflow is as follows: If the propeller motion bool is active and the simulation time exceeds the activation

time scalar, the code identifies and manipulates the points within a specified rotating cell zone. The displacement of these points is calculated using quaternion-based rotation transformations. For the rest of the points, the code applies a general transformation based on the initial mesh configuration. Finally, the new displacements are constrained and boundary conditions are updated accordingly.

Appended stern region of the ship that embodies CSM model is shown in Figure 4. The purple cylinder represents rotating cell zone which encapsulates all the geometrical details of the actual propeller. Numerical procedure implemented in this work allows for AMI interfaces that depict the rotating cell zone to stay well preserved, irrespective of the rigid body motion amplitude.

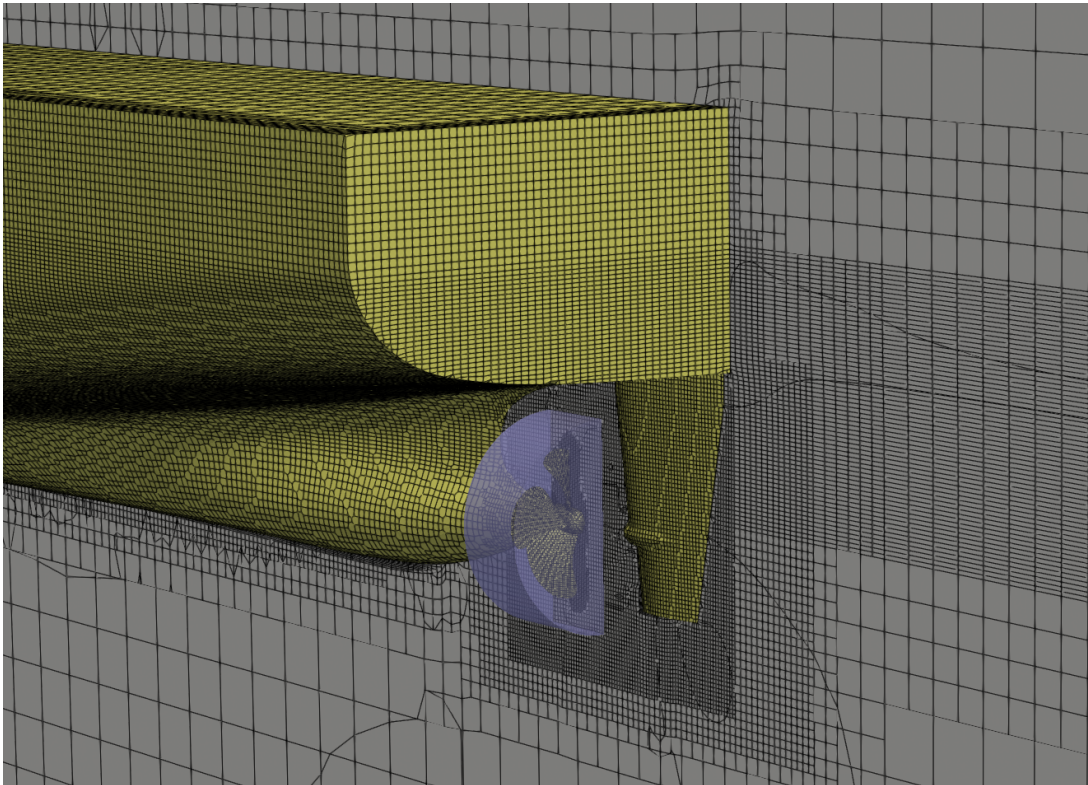


Figure 4: Typical mesh topology in propulsion simulations with CSM

The main limitation of the model is that it does not overcome the well-known computational requirements necessary for any fully-resolving rotating geometries in CFD where the time step is dictated by the angle increment of the propeller within one iteration. This increment is usually of the order of  $1^{\circ}$ - $5^{\circ}$ , depending on the propeller rate of revolution.

However, this numerical model still offer savings in computational time opposed to using overset methodology. Beyond that, the creation of proper AMI from background and propeller mesh requires additional care in the pre-processing phase. The similarity

can be achieved with conforming the both background and propeller mesh to the same geometrical characteristics.

Ensuring identical initial mesh size, mesh quality parameters and refinement levels is critical for setting geometrically similar AMI interface. Furthermore, since the rigid-body displacements of the hull are based on SLERP interpolation (Shoemake, 1985), the propeller cell zone must lie entirely within the inner distance region to ensure that the interpolation procedure fully captures the rigid body motion and maintains consistent mesh rotation across the interface. This requirement can be regarded as a numerical limitation of the model, which could be addressed in future work by implementing a "protected" propeller cell zone, ensuring that its points always move coherently with the rigid body, irrespective of the propeller position.

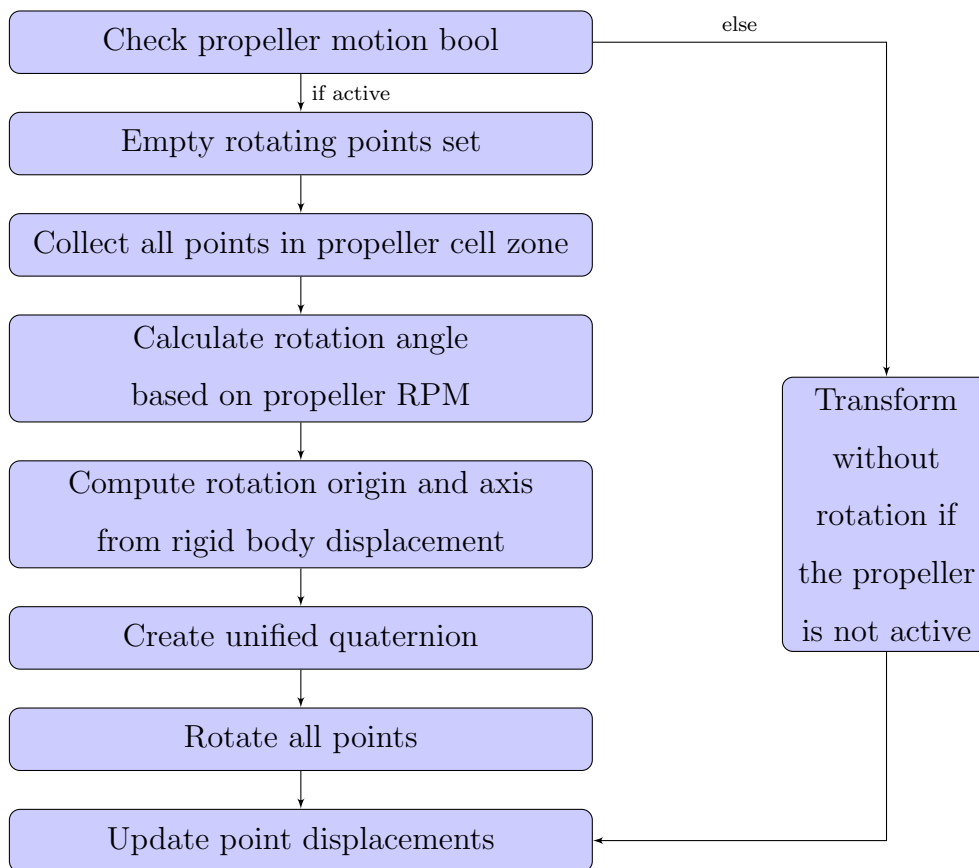


Figure 5: Computational workflow of the CSM model

Similar to AD subchapter, a pseudocode of the updated `sixDoFRigidBodyMotionSolver` class within the `sixDoFRigidBodyMotion` for additional propeller motion is given in Algorithm 2.

---

**Algorithm 2** sixDoFRigidBodyMotionSolver updated class for propeller motion

---

**Require:** cellZone, propeller axis and origin, activation time, revolution rate**Ensure:** Updated point displacements

```

if propellerMotion = TRUE  $\wedge$  time  $\geq$  activationTime then
  rotatingPointsSet  $\leftarrow$   $\emptyset$ 
  rotatingCellZone  $\leftarrow$  mesh.cellZones[rotatingZoneID]
  for all cell  $\in$  rotatingCellZone do
    cellPoints  $\leftarrow$  mesh.cellPoints[cell]
    for all point  $\in$  cellPoints do
      rotatingPointsSet.insert(point)
    end for
  end for
  localPoints  $\leftarrow$  rotatingPointsSet.toList()
  rotatingPoints  $\leftarrow$  rotatingPointsSet.toList()
  rotationAngle  $\leftarrow$  rotationRate  $\times$  time
  shipPosition  $\leftarrow$  motion.centreOfRotation()
  shipOrientation  $\leftarrow$  motion.orientation()
  rotationOrigin  $\leftarrow$  shipPosition + (shipOrientation  $\times$  (initialRotationOrigin -
initialShipOrigin))
  rotationAxis  $\leftarrow$  shipOrientation  $\times$  initialRotationAxis
  quaternion  $\leftarrow$  createQuaternion(rotationAxis, rotationAngle)
  rotationMatrix  $\leftarrow$  quaternion.toRotationMatrix()
  for all point  $\in$  rotatingPoints do
    currentPos  $\leftarrow$  points0[point] + pointDisplacement[point]
    rotatedPos  $\leftarrow$  rotationOrigin + transform(rotationMatrix, currentPos - rotationOrigin)
    pointDisplacement[point]  $\leftarrow$  rotatedPos - points0[point]
  end for
else
  pointDisplacement  $\leftarrow$  motion.transform(points0, scale) - points0
end if

```

---

This concludes the chapter on implemented propulsion models in OpenFOAM. Next chapter deals with the established methodology for estimating propulsive coefficients in both calm water and waves.

## 4 PROPULSIVE COEFFICIENTS

The most comprehensive approach for studying ship propulsion inherently implies the need for taking into account efficiencies in ship propulsion system. Therefore, in this thesis, propulsive coefficients are calculated in both full and model scale across calm water and wave conditions. This chapter outlines the theoretical foundations, definitions and physical interpretations of ship propulsive coefficients. Furthermore, methodology for estimating propulsive coefficients in waves is explained in detail.

### 4.1 Definition and Physical Interpretation

The most common definition of efficiency is the ratio between useful and total power expended (Birk, 2019). In this thesis, only the hydrodynamic component of propulsion efficiency is studied, i.e., the quasi-propulsive efficiency, which hereafter is referred to simply as propulsive efficiency. Losses in the mechanical systems (shafting and gears) are thus not taken into account. The very first factor involved in the propulsive efficiency of ships is usually the **open water propeller efficiency**, noted as  $\eta_0$ . This coefficient represents a ratio between the thrust power and the power absorbed by the propeller operating in open water conditions. In other words, open water efficiency serves as the baseline efficiency of the propeller in isolation, neglecting the presence of the hull in its entirety.

It represents a reference measure of how much shaft power can ideally be used to push the ship forward, but without the presence of the ship itself. This ambiguity leads to the definition of second, if not most important, factor in ship efficiency studies, namely the **hull efficiency**  $\eta_H$ . Hull efficiency comprehensively quantifies hydrodynamic interactions between the ship's hull and the propeller. It expresses how the propeller's presence and the resulting flow field around the hull modify the effective propulsion power required compared to the hull resistance in a pure towing condition. Two key terms are central to understanding hull efficiency. The first is the **thrust deduction fraction**, traditionally noted as  $t$ . Thrust deduction fraction represents the portion of the propeller's thrust that is effectively lost due to the increased pressure between the propeller and the hull. This phenomenon leads to an apparent rise in hull resistance when the propeller is operating, meaning that not all of the generated thrust contributes directly to overcoming the ship's

resistance.

Closely related to the thrust deduction fraction is the **wake fraction**  $\omega$ , which describes how the flow approaching the propeller is influenced by the hull. As the ship moves forward, the hull creates a region of slower-moving water behind it, known as the wake, which is caused by viscous effects and flow separation along the hull surface. The propeller operates within this wake rather than in the undisturbed freestream flow, meaning it experiences a lower inflow velocity than the ship's actual forward speed. **Nominal wake** describes the flow deceleration in the propeller plane but without presence of the propeller while the **effective wake** is measured in the propeller plane, with the propeller placed (Molland et al., 2011). In simple terms, wake fraction determines the deceleration of water due to the specific hull shape. Taken together, the thrust deduction fraction and the wake fraction capture the complex interaction between the hull and the propeller.

Another aspect in hull efficiency concerns how the propeller itself performs when operating in the non-uniform wake field behind the ship. This aspect is captured by the **relative rotative efficiency**  $\eta_R$ , which compares the propeller's actual performance behind the hull with its behavior in ideal open-water conditions. In the recent decade, various ESD have been developed in order to enhance this efficiency. Now that the physical interpretations of propulsive coefficients are outlined, next subchapter presents the methodology for their estimation in waves.

## 4.2 Methodology for Estimation of Propulsive Coefficients in Waves

For clarity and reproducibility purposes, it is necessary to give a detailed methodology for calculation of propulsive coefficients that are in this thesis applied in both main chapters. Conforming to the ITTC nomenclature, quasi-propulsive efficiency  $\eta_D$  is defined as:

$$\eta_D = \eta_0 \cdot \eta_H \cdot \eta_R \quad (45)$$

Open water propeller efficiency,  $\eta_0$ , is defined as:

$$\eta_0 = \frac{T \cdot V_A}{2 \cdot \pi \cdot n \cdot Q_0} \quad (46)$$

Advance velocity  $V_A$  and  $Q_0$  are determined using thrust identity method. Hull efficiency,  $\eta_H$ , is defined as:

$$\eta_H = \frac{1 - t_w}{1 - w_{eff}} \quad (47)$$

which comprehensively represents the hull-propeller interactions, both from the standpoint of thrust deduction fraction and effective wake fraction, as noted in subchapter 4.1. In the simulations in waves, determining the exact mean self-propulsion point was not sought both in full and model scale. Such approach is noted in many experimental and numerical studies (Turnock et al., 2024; Yu et al., 2023). As will be shown later, no corrections of the operating point of the propeller is needed in mild sea state. Therefore, thrust deduction fraction in waves is defined as:

$$t_w = \frac{\overline{R_{TAP}} - \overline{R_{T_{towed}}}}{\overline{R_{TAP}}} \quad (48)$$

where  $\overline{R_{TAP}}$  stands for the overall averaged resistance with a running propeller while  $\overline{R_{T_{towed}}}$  represents towed resistance at the same speed. In the model-scale chapter, both  $\overline{R_{TAP}}$  and  $\overline{R_{T_{towed}}}$  are averaged over one wave encounter period while for the full-scale case in irregular waves, components are averaged over the entire simulation. With this approach, it is possible to isolate the propeller-induced component of the overall added resistance in waves exhibited from both the CSM and AD method, particularly significant for the model-scale part. The effective wake fraction,  $w_{eff}$  is determined as:

$$w_{eff} = 1 - \frac{V_A}{V_S} \quad (49)$$

where thrust identity method is utilized to determine  $V_A$  while  $V_S$  stands for ship speed. Similar approach for the experimental determination of thrust deduction fraction and effective wake fraction is noted in (Saettone et al., 2021). The mentioned study is to be used for comparing the propulsive coefficients in waves in model scale since in the original experimental study from (Rabli as, 2022) propulsive coefficients were not studied. Relative rotative efficiency  $\eta_R$ , is defined as a ratio between the propeller torque in open water condition  $K_{Q_0}$  and in behind condition  $K_Q$ , for the same produced thrust:

$$\eta_R = \frac{K_{Q_0}}{K_Q} \quad (50)$$

It is important to stress that the AD method inherently reads the values from the open water diagram thus, the relative rotative efficiency for the AD method is to always be unity. This is, later on, emphasized as one of the main limitations of this method in propulsion efficiency assessments. This methodology of calculating propulsion coefficients is to be established both for calm water and wave conditions, thus yielding a valid comparison between these two environmental conditions. This is summarized in Figure 6.

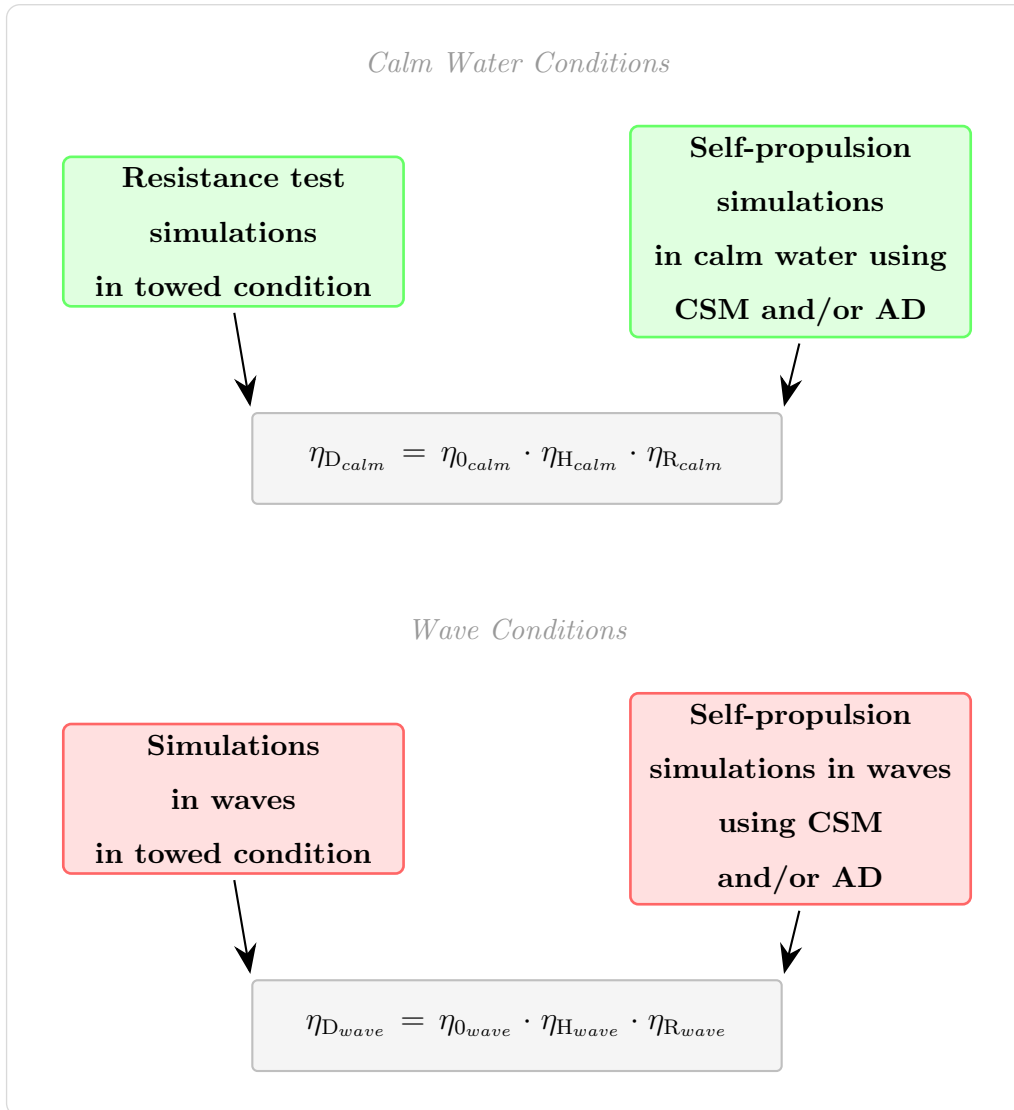


Figure 6: Methodology for calculation of propulsion coefficients in waves

The preceding chapters have established the implementation of propulsion models in OpenFOAM and the methodology for calculating propulsive coefficients in waves. The following chapters apply these models and methodology to both full-scale and model-scale.

## 5 NUMERICAL MODELLING OF SHIP PROPULSION IN FULL SCALE

This chapter deals with the application of the implemented AD model on a full scale case study, a 14,000 TEU Post-Panamax containership from which onboard measurements during navigation along with sea trial data are used for validation of the numerical model. This chapter is organized as follows. First, a brief depiction of the subject ship used in the study and corresponding onboard measurements are given. It is followed by CFD simulations of a propeller operating in open water conditions, as the open water curves are necessary for the AD model. For open water simulations, verification study is performed for one advance coefficient in order to determine and quantify the discretization errors, as the rest of the full scale investigation is based on these computed values.

After obtaining thrust and torque curves of the full-scale propeller, AD model is used for the simulations of sea trials. Sea trial simulations are performed for three mesh densities in order to determine the sufficient cell size for obtaining accurate results in foregoing simulations in waves. The last part of the chapter covers full scale simulation in a representative sea state where the numerical results are directly compared to the onboard measurements, which embodies one of the main contributions in this thesis. Great attention is given to numerical wave modelling, which is depicted in the specific subchapter. After determining correct wave spectrum shape, simulation in irregular, long-crested waves are performed and compared with onboard measurements, complemented with the assessment of propulsion coefficients in waves.<sup>1</sup>

### 5.1 Post-Panamax Containership and Full-Scale Data

This section presents a 14,000 TEU Post-Panamax containership that serves as the full-scale case study, for which onboard measurements along with sea trial data were available. Firstly, main dimensions and details of the ship are given, followed by full-scale measurements collected onboard as a part of the *DigitShip* project. The measurements provide spatially and temporally high-resolution data on ship operations, propulsion performance, and

---

<sup>1</sup>Part of this chapter has been published in I. Sulovsky, S. Mewes, O. el Moctar, and J.Prpić-Oršić. CFD study on a full-scale ship performance in a representative sea state. *Ocean Engineering*, 333:121519, 2025. ISSN 0029-8018. doi: 10.1016/j.oceaneng.2025.121519

environmental conditions during actual sea voyages. The ship is equipped with a single five-bladed propeller fitted with a Propeller Boss Cap Fins (PBCF) and an asymmetrical rudder with a modified NACA section.

Both environmental parameters such as wave characteristics and wind speed, as well as navigational data including ship dynamics captured by an Inertial Motion Unit (IMU), are recorded at a sampling frequency of 1 Hz. These measurements represent a unique opportunity to study full-scale ship performance and validate computational methods under real operating conditions. Acquiring such comprehensive onboard measurements from operational commercial ships presents substantial challenges that are not so common in academic research and data collection. Ship operators are typically reluctant to install extensive instrumentation systems due to concerns about operational disruptions, installation costs, and potential interference with commercial activities. Access to full-scale ships for research purposes requires establishing long-term collaborative relationships with ship owners and operators, often involving complex contractual agreements and liability considerations.

Furthermore, the harsh marine environment imposes stringent requirements on measurement equipment durability and reliability, necessitating specialized sensors capable of withstanding prolonged exposure to saltwater, vibrations, and extreme weather conditions. The continuous operation of commercial ships limits opportunities for equipment installation and maintenance to brief port calls, significantly complicating the technical implementation of monitoring systems. Additionally, the proprietary nature of operational data and competitive sensitivities within the maritime industry create barriers to data sharing, making publicly available full-scale datasets exceptionally rare and valuable for the broader research community.

### 5.1.1 Post-Panamax Containership

The ship used in this thesis originates from the *DigitShip* project (Jabary et al., 2022, 2023). The main project objective is to collect spatially and temporally high-resolution ship operation data (e.g., propulsion and manoeuvring relevant data) as well as environmental conditions with different systems: onboard, via satellites and ashore, their processing and provision via a cloud-based IT infrastructure (distributed Big Data Management). The ship is equipped with a single propeller that has a PBCF, an energy saving device with a

purpose of recovering the hub vortex energy into additional thrust and torque. The rudder is of an asymmetrical type with modified NACA section. Main dimensions of the ship along with propeller features are listed in Table 1. 3D model of the aft section of the ship is given in Figure 7.

Table 1: Main features of the ship and propeller

Parameter	Unit	Symbol	Value
Length between perp.	m	$L_{PP}$	349.5
Breadth	m	$B$	51.2
Design draught	m	$T$	14
Displaced volume	m <sup>3</sup>	$\nabla$	173893
Transversal mass moment of inertia	m <sup>2</sup> kg	$I_{44}$	$6.13 \cdot 10^{10}$
Longitudinal mass moment of inertia	m <sup>2</sup> kg	$I_{55}$	$1.84 \cdot 10^{12}$
Service speed (slow steaming)	kn	$V_S$	16
Diameter	m	$D$	9.4
Num. of blades	-	$z$	5
Expanded blade area ratio	-	$A_E/A_0$	0.43
Rotation direction	-	-	right-handed

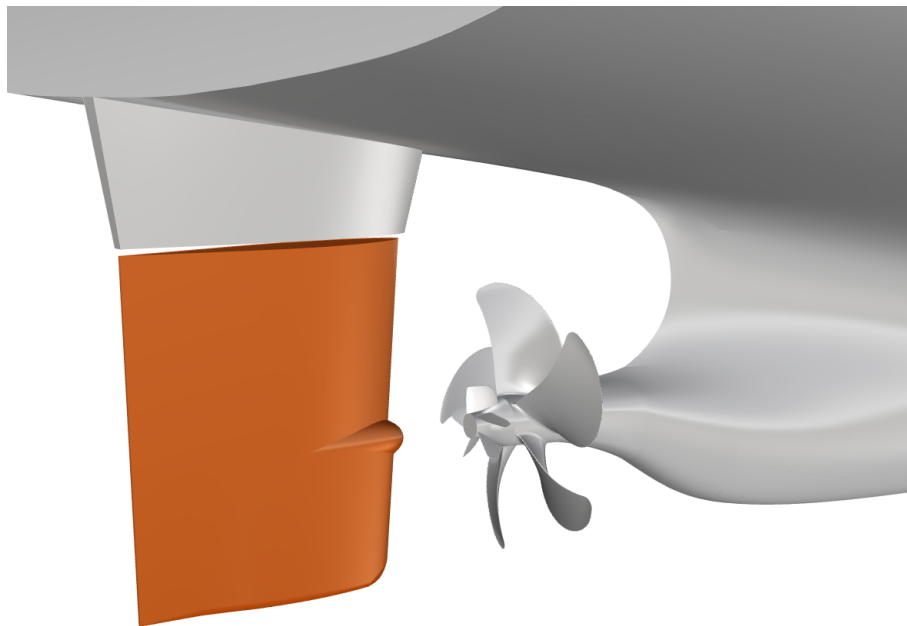


Figure 7: The asymmetrical rudder and the propeller with PBCF

### 5.1.2 Onboard Measurements

The full-scale numerical investigation conducted in this work is complemented with high-quality measurements onboard a 14,000 TEU Post-Panamax containership. In this chapter, environmental and meteorological measurements conducted onboard are depicted. As the ship data is proprietary, the hull lines plan is not shown. The onboard measurements include both environmental and ship measurements, as shown in an excerpt from a ten-day measurement span in Figure 9 and 10. The excerpt involves the ship's passage across the Pacific Ocean, starting its voyage from the port of Busan, South Korea to the port of Seattle, Washington, USA. The ship track obtained via Global Positioning System (GPS) can be seen in Figure 8.

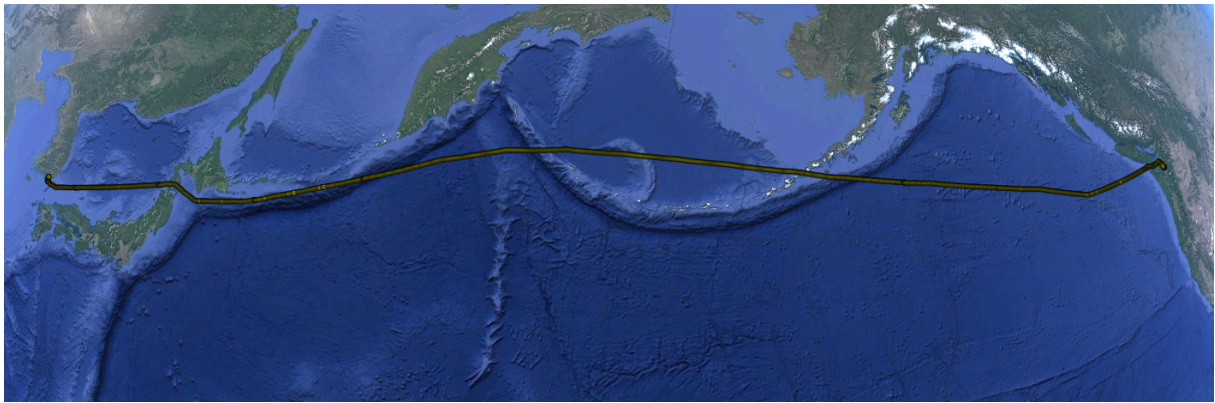


Figure 8: GPS trail of the Post-Panamax Containership

Obtaining such high-quality data comes with several challenges. From the practical point of view, sensors and equipment need to be properly installed, calibrated and connected to network without disruptions. Ensuring redundancy of the measurements due to potential switching to shore-based electrical power and power losses require careful attention.

Once the installment is finished, there is always a risk of potential unforeseen failure in the measurements during voyage. Nevertheless, collected data represent a unique opportunity to study ocean-going ships, particularly in the field of computational ship hydrodynamics, as the full-scale calculations are gaining more and more attention.

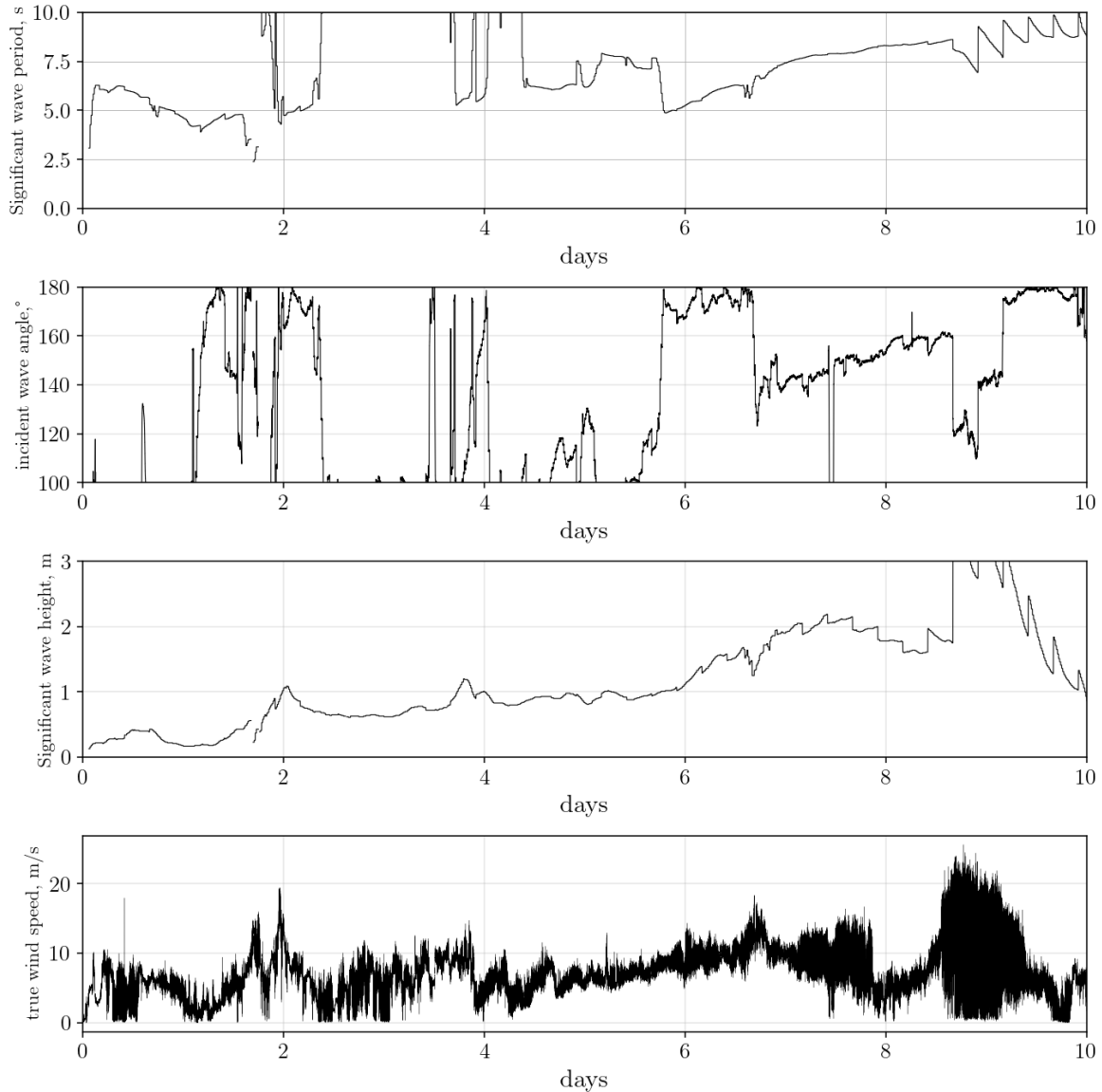


Figure 9: Environmental onboard measurements

Wave parameters are not measured in-situ, but rather this data is provided by external weather service providers. The resulting wave characteristics are derived from using different tools such as buoy measurements, satellite altimetry, wave modelling software etc.

Therefore, the provided values correspond to the latest available technologies in predicting ocean waves. Wind speed, shown in the bottom plot in Figure 9, is measured using an anemometer. Furthermore, navigational and ship parameters are measured using various GPS-based sensors while the ship dynamics are captured using an IMU with a sampling frequency of 1 Hz, i.e., one sample per second.

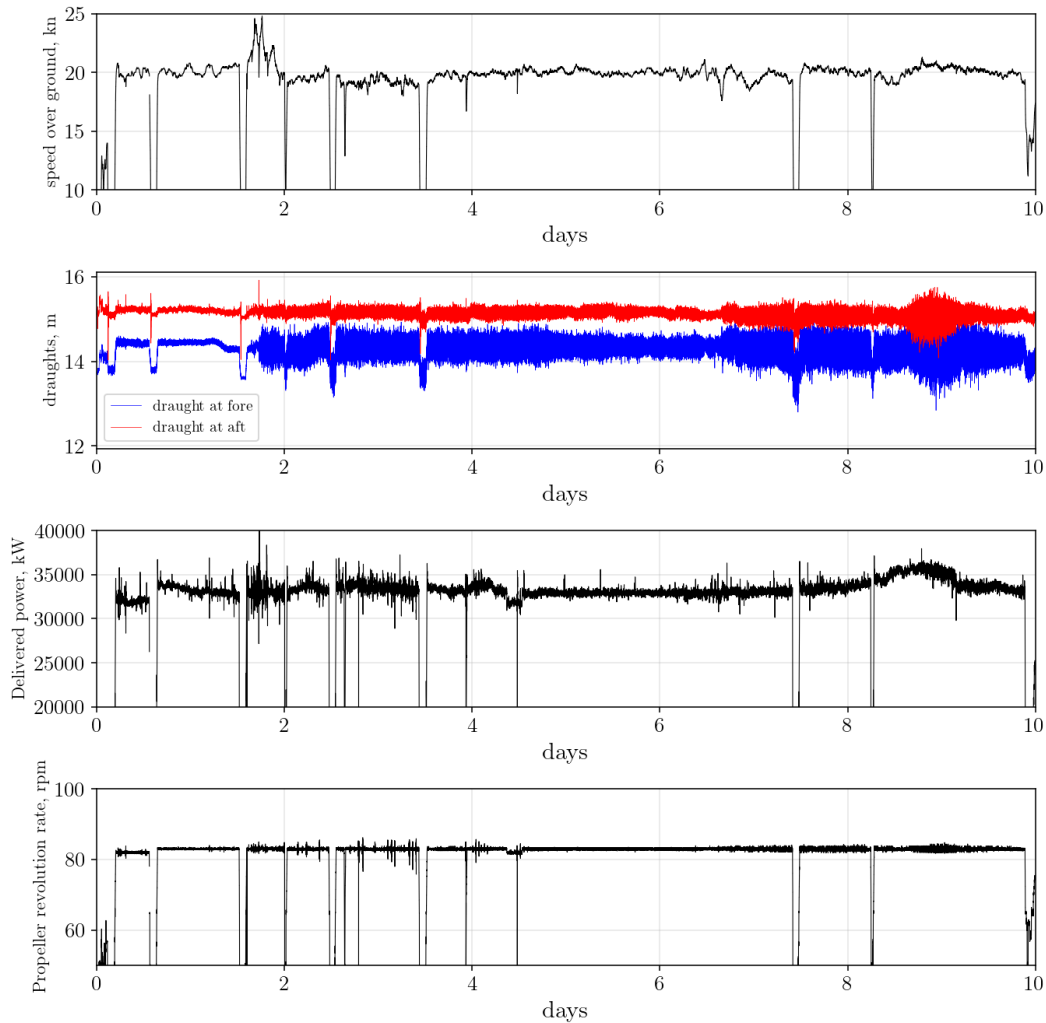


Figure 10: Navigational onboard measurements

In the next chapter, CFD simulations of a propeller operating in open water conditions are presented.

## 5.2 Open Water Propeller Simulations

As the AD model requires propeller thrust and torque coefficients from open water test, CFD simulations in full scale are conducted. OpenFOAM is also employed while using *pimpleFoam* solver. Propeller geometry is fully discretized while for the rotation effect the AMI method is imposed. Turbulence is modelled using a  $k - \omega$  SST model with wall functions including roughness of a  $100 \mu\text{m}$ . Topology of the computational domain is given in Figure 11 with gray zone encompassing rotating propeller cell zone. The inlet boundary is positioned 3D upstream of the propeller center, while the outlet is positioned

13D downstream. As the propeller is equipped with a PBCF, a reverse open test shown in Figure 12 is designed in order to take the effects of PBCF into account (Kawamura et al., 2013).

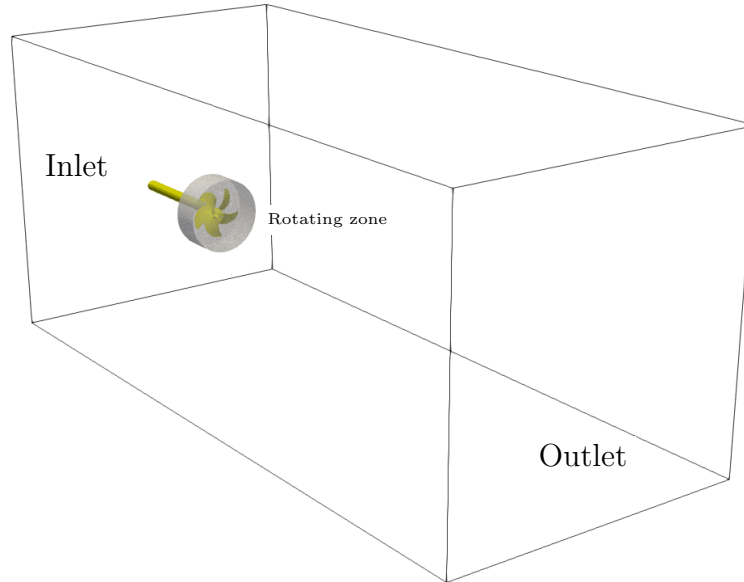


Figure 11: Computational domain for open water simulations

At the inlet boundary, a Dirichlet boundary condition is imposed, i.e., a constant uniform flow of 10 m/s while at the outlet a Neumann type boundary condition is set. On the propeller boundary, treated as patch in OpenFOAM, constant rate of revolution is imposed which was varied for different advance coefficients. At the rest of the boundaries, slip condition is set. Temporal discretization is second-order accurate, with two outer and inner corrections for pressure-velocity coupling. Computational mesh in the vicinity of the propeller is shown in Figure 13.

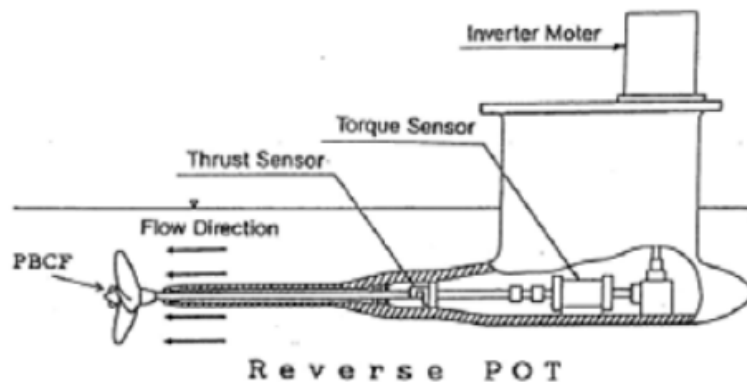


Figure 12: Reverse open water test from (Kawamura et al., 2013)

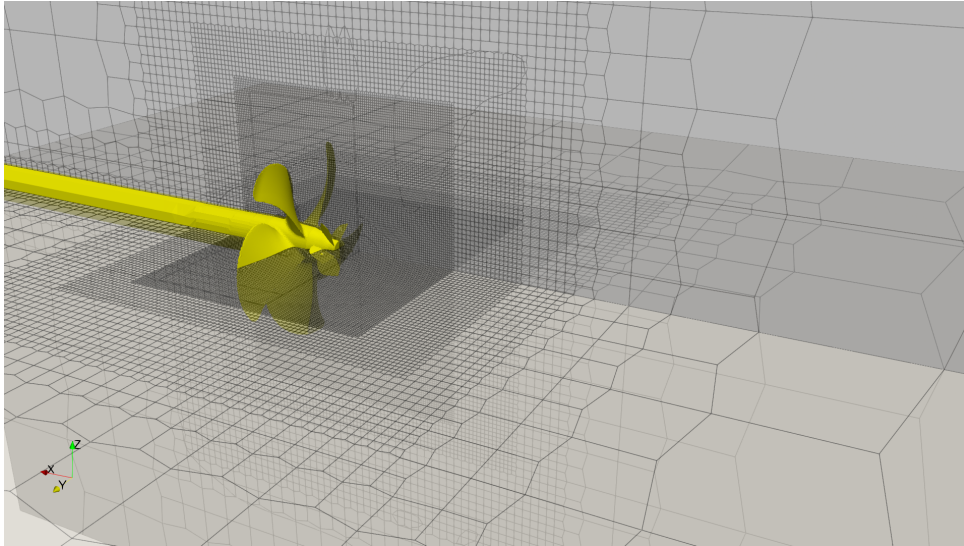


Figure 13: Mesh for open water simulations

Propeller-induced velocity in the symmetry plane is shown in Figure 14. The velocities are normalized with free stream velocity value.

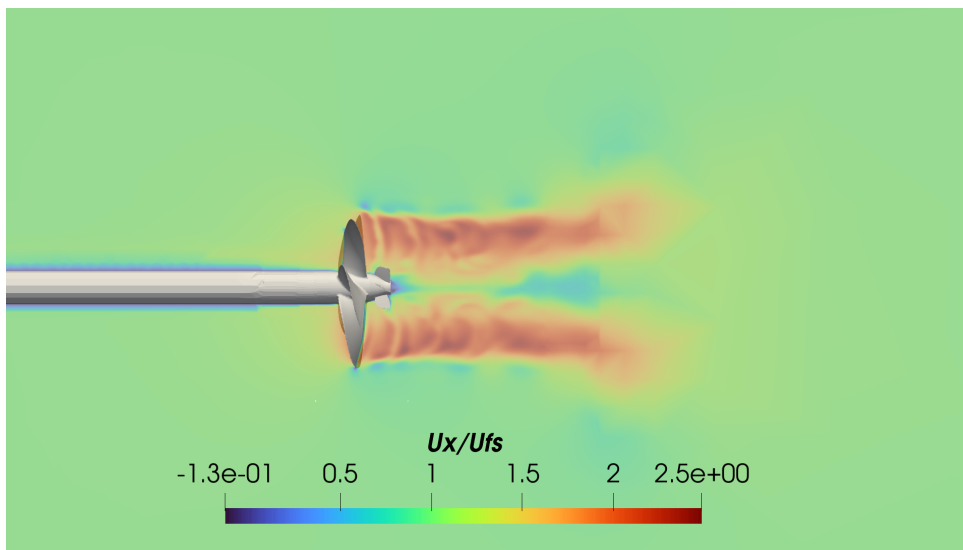


Figure 14: Velocity field in the open water simulation for  $J = 0.5$

To verify the simulations, grid converge study is conducted. The study is employed for a propeller's operating condition in sea trials which is assumed to an advance coefficient of 0.7. The simulations are performed on three successively finer grids, refined via a constant refinement ratio of  $\sqrt{2}$ , and then examined by comparing the Grid Convergence Index (GCI) (Roache, 1998), as suggested by International Towing Tank Conference (ITTC) in (ITTC, 2017a). The apparent order of convergence  $p$  is calculated as follows:

$$p = \ln((\phi_3 - \phi_2)/(\phi_2 - \phi_1))/\ln(r) \quad (51)$$

where  $\phi_i$  takes the value of the observed variable with an index that corresponds to the grid size. Grid refinement ratio is denoted as  $r$ . Furthermore, GCI index between medium and fine, and coarse and medium grids are calculated as:

$$\text{GCI}_{2,3} = 1.25 \cdot \left| \frac{\phi_3 - \phi_2}{\phi_3} \right| / (2^p - 1) \cdot 100\% \quad (52)$$

$$\text{GCI}_{1,2} = 1.25 \cdot \left| \frac{\phi_2 - \phi_1}{\phi_2} \right| / (2^p - 1) \cdot 100\% \quad (53)$$

Finally, it is necessary to check the convergence within the asymptotic range following the criterium:

$$\frac{\text{GCI}_{2,3}}{r^p \cdot \text{GCI}_{1,2}} \approx 1 \quad (54)$$

Results of the study are given in Table 2. Criterium for asymptotic convergence from Eq. (54) is satisfied for both thrust and torque coefficients as the computed values are 0.979 and 0.964, respectively.

Table 2: Verification study for open water propeller simulations

<b>Grid</b>	<b>cell number</b>	<b>Index <math>i</math></b>	$K_T, \phi_i$	$K_Q, \phi_i$
coarse	961337	3	0.18257	0.0318
medium	2647999	2	0.1743	0.0296
fine	7188067	1	0.1708	0.0286

Additionally, GCI indexes for both coarse and fine grids are given in Table 3:

Table 3: Calculated GCI indexes for thrust and torque coefficients

<b>GCI</b>	$K_T$	$K_Q$
GCI <sub>1,2</sub> (fine grid)	0.019	0.043
GCI <sub>2,3</sub> (coarse grid)	0.044	0.086

Thrust and torque coefficients along with open water efficiency curve is given in Figure 15.

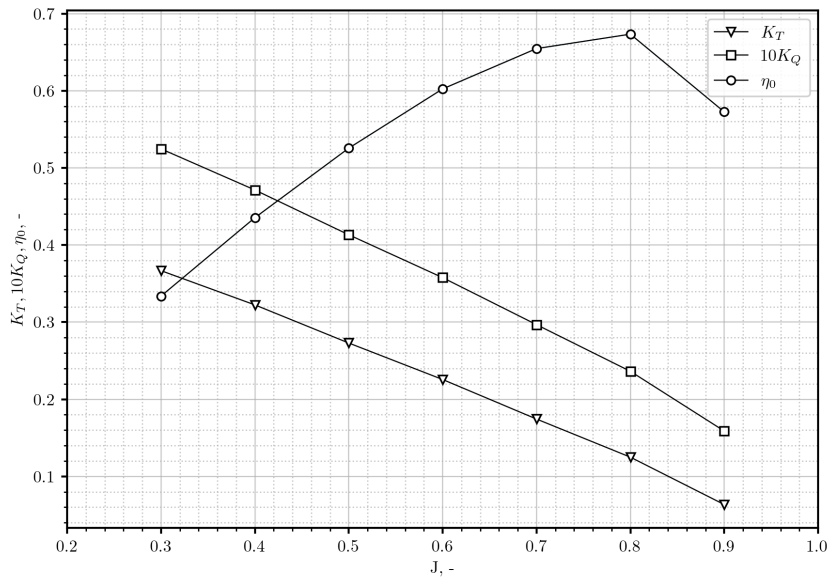


Figure 15: Open water propeller curves

This study demonstrates not only the dependence of certain variables on grid size, but it also indicated the trend of their change towards asymptotic values. The grid verification study shows favourable results and convergence of the solution. The difference between medium and fine grid results are in the range 2-3 % which implies that the results for all advance coefficients calculated with medium grid size are sufficiently accurate.

Therefore, the results shown in Figure 15 are successfully adopted into the AD model. It is of great importance of knowing in advance the margin of error coming from open water simulations as the AD model directly reads the values in propulsion simulations. With grid verification study, this chapter is concluded. After implementation of the AD model and calculating necessary open water curve, now is the time to test the performance of the model in full-scale, conducting sea trial simulation, which is the subject of the next chapter.

### 5.3 Sea Trial Simulations

This chapter covers CFD simulations in a sea trial condition in calm water of the 14,000 TEU containership. The main goal of these simulations is to compare the delivered power from CFD using Eq. (55) with sea trial measurements value which will give an indication of the performance of the implemented AD model in full scale. In the sea trials, two speed

runs have been conducted for the same engine speed and propeller revolution rate of 87 rpm. The loading condition in sea trials significantly differs from the design condition.

Reading of the draught mark at the aft equals to 9.5 m while at the fore is 5.2 m. The position of the longitudinal center of gravity is slightly corrected to achieve hydrostatic equilibrium for the reported draughts. In the simulations, the ship is allowed one translational degree of freedom (sinkage) and one rotational degree of freedom (trim), with inertial properties obtained from the trim and stability booklet. Starting conditions for sea trial simulations are given in Table 4.

Table 4: Ship parameters for a sea trial condition

Parameters	Unit	Symbol	Value
Draught at aft	m	$T_A$	10.5
Draught at fore	m	$T_F$	7.5
Displacement	t	$\Delta_{st}$	34301
Longitudinal mass moment of inertia	kgm <sup>2</sup>	$I_{55}$	$1.21 \cdot 10^9$
Achieved speed	knots	$V_{st}$	21.908
Propeller revolution rate	rpm	$n_{st}$	87
Delivered power	kW	$P_{Dst}$	38200

During the trials, torque is measured by a torsion meter after which it is straightforward to estimate the delivered power with a relation:

$$P_D = 2\pi nQ \quad (55)$$

Where  $n$  is the propeller revolution rate and  $Q$  is the torque. Same relation is used for estimating calculated delivered power from CFD simulations in which the torque  $Q$  is calculated by the AD model from open water propeller curve. Simulations are performed on three grids with different grid spacing in order to determine numerical uncertainties. The level of refinement between three grids is uniform and approximately equals  $\sqrt{2}/1.15$  which yields an approximate 25% increase in initial grid size.

Such refinement ratio is chosen since the conventional value recommended from the ITTC of  $\sqrt{2}$  would yield exceptionally long computational times. Coarse grid consists of  $1.31 \cdot 10^6$  cells, medium grid of  $2.69 \cdot 10^6$  while the finest grid has  $7.18 \cdot 10^6$  cell count. Geometry of the superstructure is not included in order to further reduce the cell count

without endangering the quality of the results. Regarding the computational domain, their extents are in line with the recommendations given by (ITTC, 2017a).

The origin of the coordinate system is located at the intersection between the aft perpendicular of the ship and the free surface. Inlet boundary is situated at a distance of  $L_{PP}$  from the fore perpendicular of the ship; the outlet boundary at a distance of  $3L_{PP}$  from the aft perpendicular. Side walls are set to  $1.5L_{PP}$  from both the ship's port and starboard sides. Figure 16 shows a schematic representation of the domain.

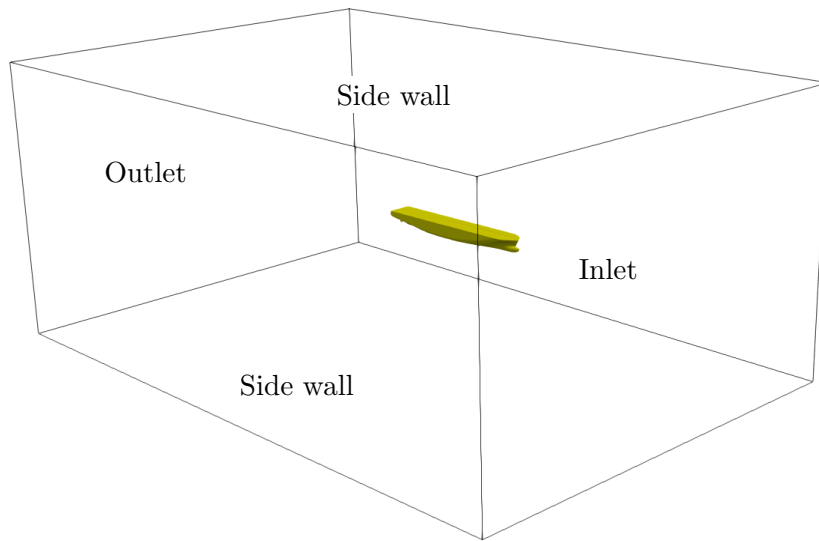


Figure 16: Boundaries of the computational domain for sea trial simulations

The *olaFlow* package is used for wave generation and absorption at domain boundaries. Within this thesis, boundary conditions stemming from initial *olaFlow* are rewritten to account for uniform wind speed, regardless of a concurrently acting current speed. This is an improvement of the current *olaFlow* open-source implementation.

At the inlet, waves are generated using the specific `waveVelocity` condition for velocity and `waveAlpha` for the volume fraction, while the outlet is set the same but for absorption. Boundary condition on the domain sides and bottom are modelled as symmetry planes, while the atmosphere boundary (top patch) uses `pressureInletOutletVelocity` and `inletOutlet` condition. For turbulent quantities, zero gradient conditions are applied at the outlet while fixed values are imposed on the inlet patch. On the hull and rudder modelled as walls, wall function are employed.

Gradual refinement of the grid for free surface capturing is seen in Figure 17, while the region of the refined grid for actuator disk is shown in Figure 18.

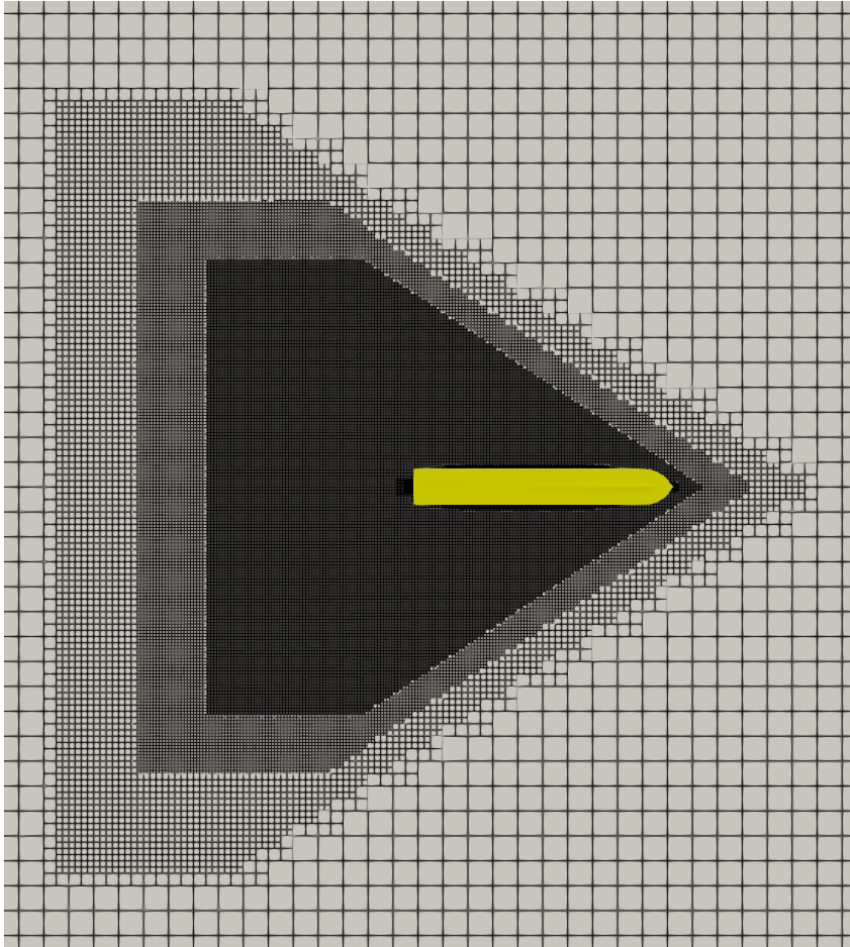


Figure 17: Kelvin wake refinements

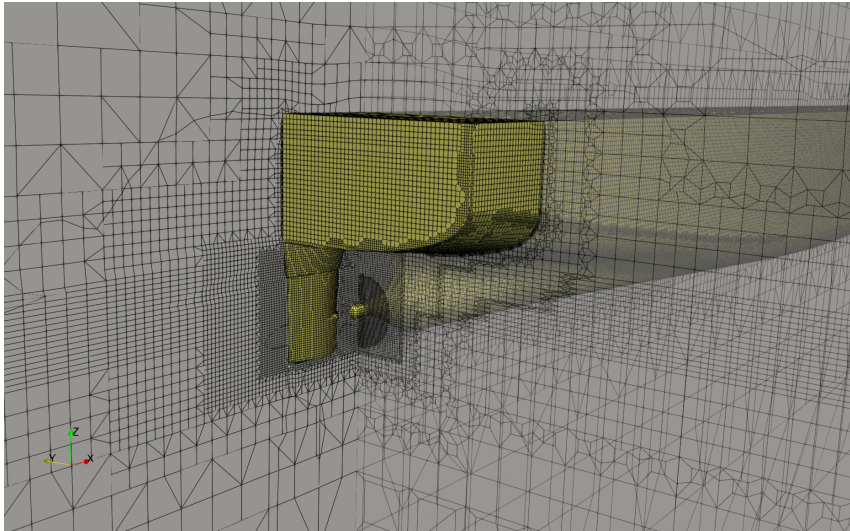


Figure 18: Cross section at propeller plane and center line

Boundary layer is discretized with 9 prism layers using an expansion ratio of 1.12. The thickness of the first cell adjacent to the hull is set to 20 mm yielding a value of dimensionless distance to the wall  $y^+$  between 2000 and 3500. Extremely high values of

$y^+$  are seen across full scale ship simulation. For example, (Jasak et al., 2019) reported values of  $y^+$  around 900 and 1100 with CFD prediction differing no more than 0.3% for two full scale cases.

Roughness is modelled using wall functions, with an equivalent sand grain roughness set to 100 microns, which is consistent with the thorough investigation conducted by Orych et al. (2022). Generated grid consists predominantly of hexahedral cells with approximately 7% of the cells being polyhedral. Maximum non-orthogonality of the cell for all grids is approximately 67.6.

### 5.3.1 Results of Sea Trial Simulations

Simulation strategy of sea trial speed test consist of dividing the simulation in two; Firstly, propeller rotation is omitted while setting a maximum possible time step  $\Delta t$  of  $2.5 \cdot 10^{-2}$ . After stabilization of the free surface and convergence of forces on the hull, AD is activated and set to a fixed rotation rate of 87 rpm, as per sea trial report.

In this manner, there is no need for separate towed and self-propulsion simulations since the AD is activated during the simulation runtime. Resulting signals of the absolute value of total ship resistance and propeller thrust achieved on a medium dense grid are given in Figure 19. Magnification of the signals is also shown which indicates a tight convergence of the simulation within 2% oscillations around mean value.

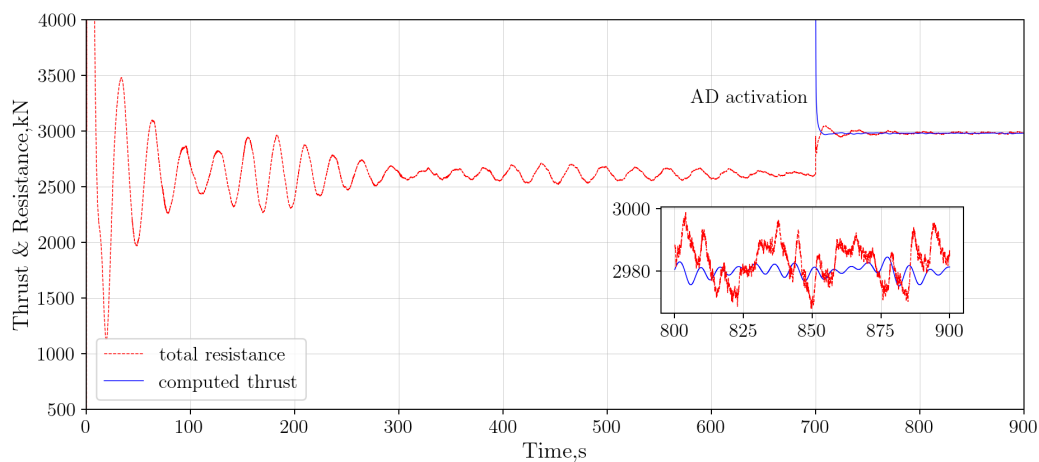


Figure 19: Resistance and thrust signals from the sea trial simulation

As seen in Figure 19, the self-propulsion point is correctly captured. Overall results for three grids are given in Table 5.

Table 5: Results of sea trial simulations

	<b>Unit</b>	<b>Symbol</b>	<b>Coarse</b>	<b>Medium</b>	<b>Fine</b>
Resistance	kN	$R_T$	3011.58	2977.63	3012
Thrust	kN	$T$	3004.39	2979.09	3000.17
Delivered power	kW	$P_{D,CFD}$	40507.94	40257.80	40466.62
CFD/sea trials	%	$E$	5.69	5.11	5.60
Sinkage	m	$z$	-0.254	-0.251	-0.252
Pitch	°	$\theta$	+0.390	+0.391	+0.391

As the grid refinement study is showing very low variability of the observed variables, it suggests that the principal parameters of thrust, torque, resistance and ship dynamics are relatively insensitive to the mesh resolution. Although the refinement ratio used is smaller than in open water propeller simulations, even the variability among coarse and fine mesh is negligible.

(Eça and Hoekstra, 2014) defined oscillatory convergence as a condition where successive grid refinements produce solutions that fluctuate around an asymptotic value without settling into a consistent monotonic pattern. Similar finding can be seen in a full scale sea trial simulations in (Jasak et al., 2019). Following the same principle as in (Larsson and Stern, 2015), uncertainty quantification is defined as:

$$U = 0.5 \cdot F_S(\phi_{min} - \phi_{max}) \quad (56)$$

where  $\phi$  is the observed variable with corresponding minimum and maximum values across multiple grids. Safety factor is denoted as  $F_S$ , taking the value of 3. Therefore, the calculated numerical uncertainty for the resistance is at 51.5  $N$  or 1.7% while for the thrust at 31.5  $N$  or 1.05%.

The calculated delivered power exhibits uncertainty of 0.9%, or 375 kW. Based on the calculated results, medium grid size is adopted for further numerical simulations in waves. Sea trial simulation results presented above address the performance of the AD model in calm water. Observing Table 5, CFD results of the delivered power, calculated via Eq. (55) across all mesh refinements exhibit approximately 5% underprediction with

respect to sea trial data. Two main reasons that might influence this small difference are hull roughness and air resistance exhibited from the superstructure. Ship-induced wave elevations are shown in Figure 20 where typical loading condition of the ship in sea trials can be seen.

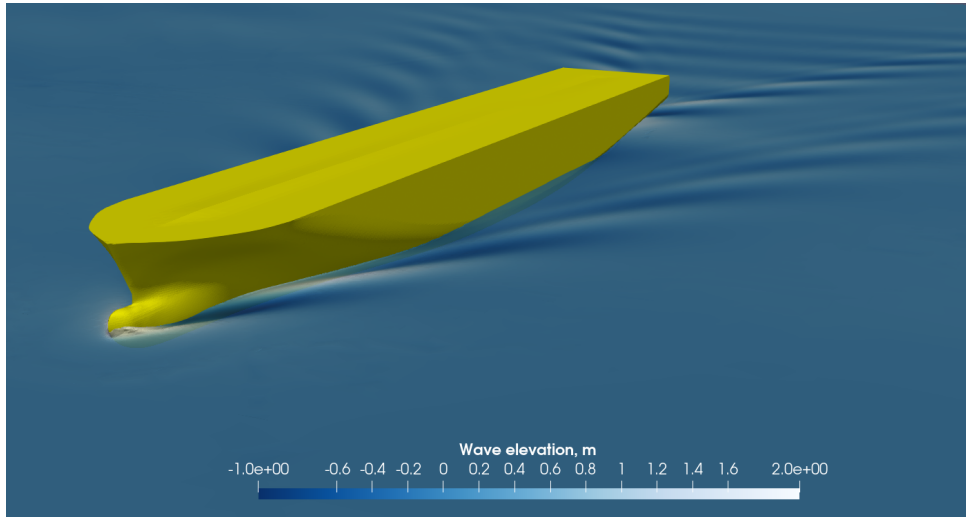


Figure 20: Wave elevations from sea trail simulations

The influence of the air resistance stemming from the superstructure is a subject of the next chapter.

### 5.3.2 Influence of the Superstructure's Air Resistance in Sea Trial Simulations

As stated, separate simulation is conducted in order to determine up to which extent does the air resistance exhibited from the superstructure influences sea trial simulation. Numerical simulation is based on a steady-state, incompressible RANS model where the superstructure 3D geometry is modelled from general arrangement plans. Due to proprietary reasons, general arrangement plans cannot be shared within this thesis. To achieve consistency in turbulence closure,  $k-\omega$  SST model is also employed. The concept of computational domain and boundary conditions are practically the same as in subchapter 5.2, where open water propeller simulations are conducted. The main difference is in the flow speed, where in this assessment a flow speed equal to the ship's velocity  $V_{st}$ , recorded in sea trials is set.

The logarithmic profile of the inlet velocity boundary condition is omitted, since the atmospheric wind loads are not of interest, as represented for example in (Prpić-Oršić et al., 2020; Valčić and Prpić-Oršić, 2016) or (Degiuli et al., 2025; Grlj et al., 2023). The ship's

operational condition in sea trials allows for using simple, steady velocity profile across the domain. Furthermore, to achieve consistency in the comparison with sea trials, medium mesh size from the sea trials is adopted. Opposed to the full scale sea trials, in this air resistance assessment it is insisted on  $y^+$  values being in the classical region of 30-300, as emphasized and explained in 2.1.2. The computational grid consist of approximately  $10^6$  control volumes where the boundary layer is discretized with 10 layers with first adjacent layer near the wall stretched for 2.5 mm.

The resulting signal of total resistance induced by the superstructure, showing sharp convergence, is shown in Figure 21. Above the plot, typical RANS-smoothed fields are shown with color scale indicating the air velocity drop normalized with ship's sea trial speed.

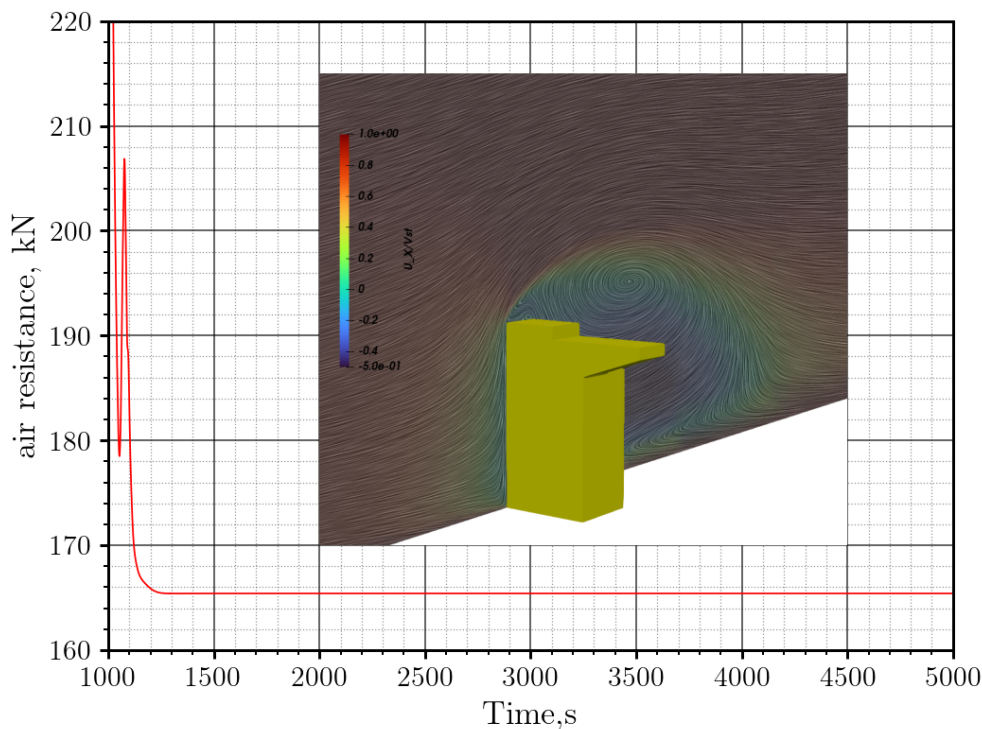


Figure 21: Air resistance signal and velocity field over superstructure

Since the containership's structure above waterline presumes two distinct superstructures, one positioned at the midship and one at the aft part of the ship, total resistance is simply taken as a double value. Possible influence on midship superstructure's wake on the resistance of the one positioned in the aft is omitted. The resulting force of 165.5 kN holds approximately 5.5% of the ship resistance from sea trials for medium grid, seen in Table 5.

In this part, grid sensitivity study is not conducted since the purpose of this simulation is to, in a simplified manner, address the slightly underpredicted delivered power in sea trial simulations. The comprehensive sea trial simulations presented herein provide a rigorous foundation for the following simulation in irregular wave conditions. Important to note, air resistance is not taken into account in the following chapter.

## 5.4 Simulation in a Representative Sea State

In this chapter, full scale simulation of the subject Post-Panamax containership advancing in unidirectional irregular waves resembling the representative sea state conditions, with AD propulsion model is presented. The adopted sea state, from now on referred as Representative Sea State (RSS) is described as follows. Based on the long-term probability distribution of significant wave height and zero-crossing period shown in Figure 22 (from (Hogben and Lumb, 1967)):

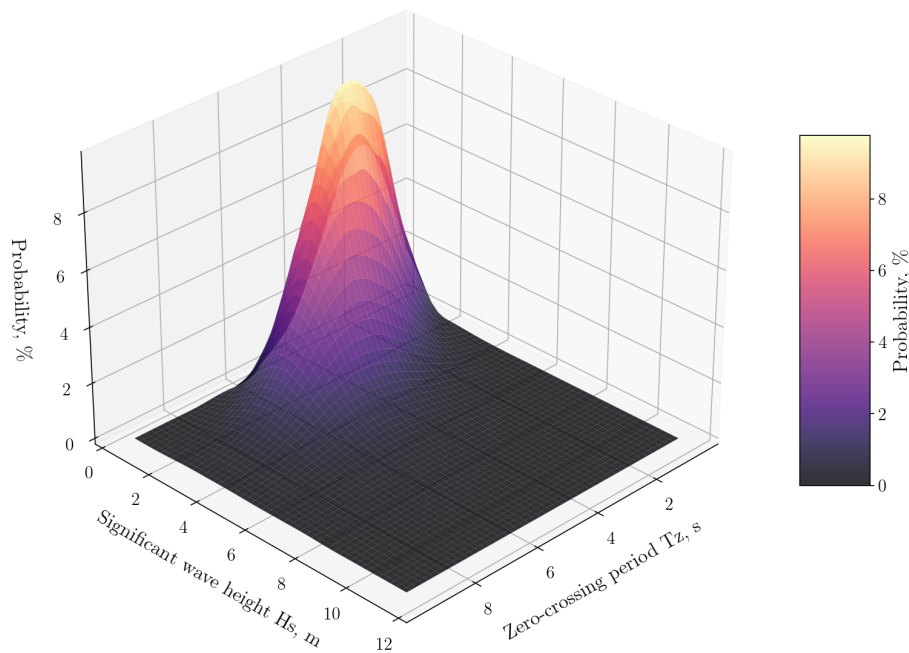


Figure 22: Wave Statistics from (Hogben and Lumb, 1967)

Highest probabilities occur at a significant wave heights of 1-3 meters with corresponding wave periods in range of 5-7 seconds. Therefore, in this study, representative sea state parameters were chosen within this narrow range of values. To further support the validity of the chosen wave parameters, similar values of the wave characteristics are

reported in (Dodet et al., 2010). Thus, RSS wave characteristics are selected based on the statistically dominant sea state.

#### 5.4.1 Assessment of Wave Spectrum in 2D

Before conducting full scale simulations of the containership advancing in irregular waves, validation of the appropriate wave spectrum used to model the representative sea state needs to be conducted. For validation purposes, a data segment is selected from the onboard measurements, corresponding to the beginning of day six, seen in Figure 9 and 10. For clarity, magnified plots depicting the validation dataset are shown in Figure 23 and 24.

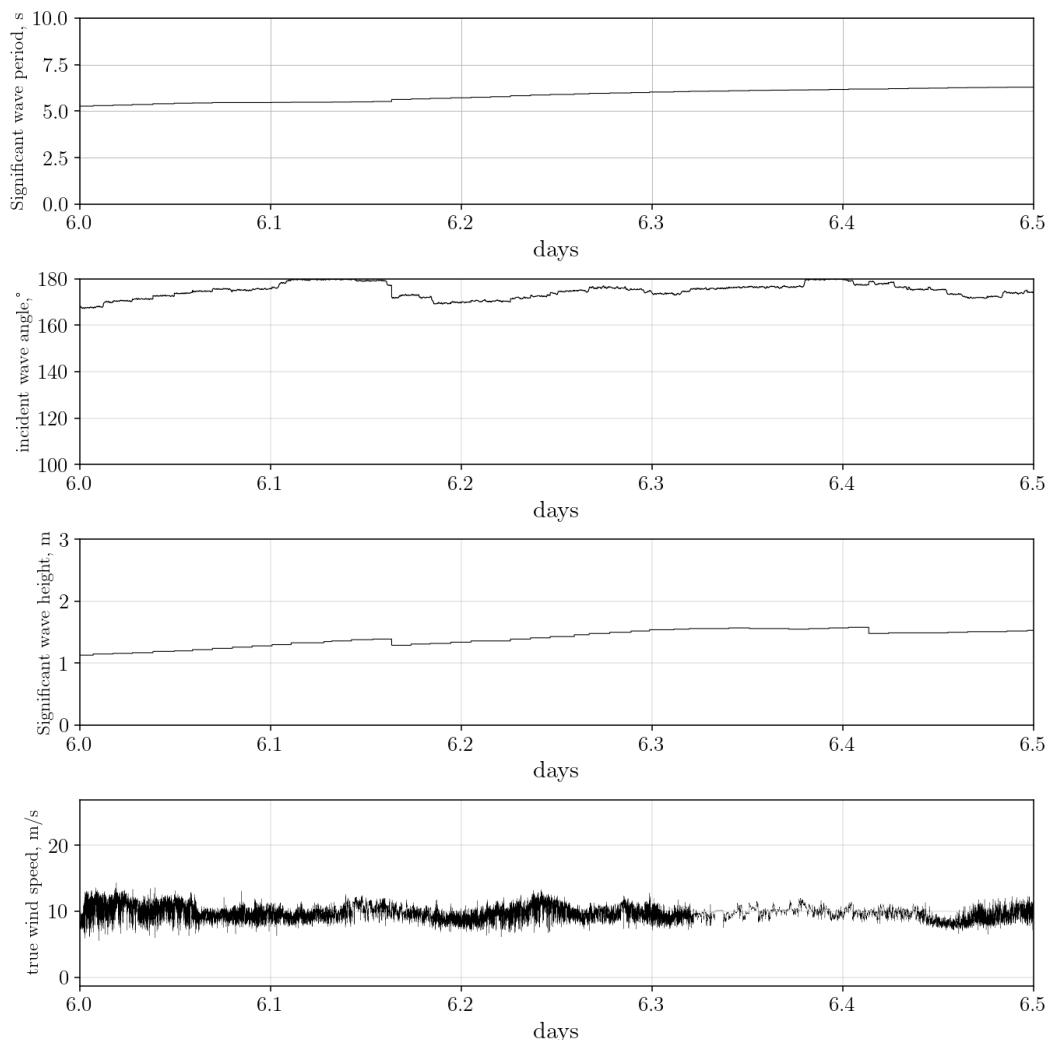


Figure 23: Validation dataset of shipboard measurements

Dataset shown in Figure 23 represent certain input data for CFD simulations. Significant wave height and period exhibit average values of 1.31 meters and 5.5 seconds, respecti-

vely, well within RSS range explained beforehand. Therefore, these values are taken for obtaining irregular wave spectrum, as shown later in the text. During this period of navigation, the ship encountered almost pure head waves with an average incident angle close to  $180^\circ$ . Therefore, spectrum waves are modelled as unidirectional.

Dataset shown in Figure 24 is consisting partly of input and validation data. For instance, value of speed over ground is taken as flow velocity in the simulations while the main engine power is the validation data, used for comparison with results from the AD propulsion model. Measured draughts showcase the loading condition of the ship.

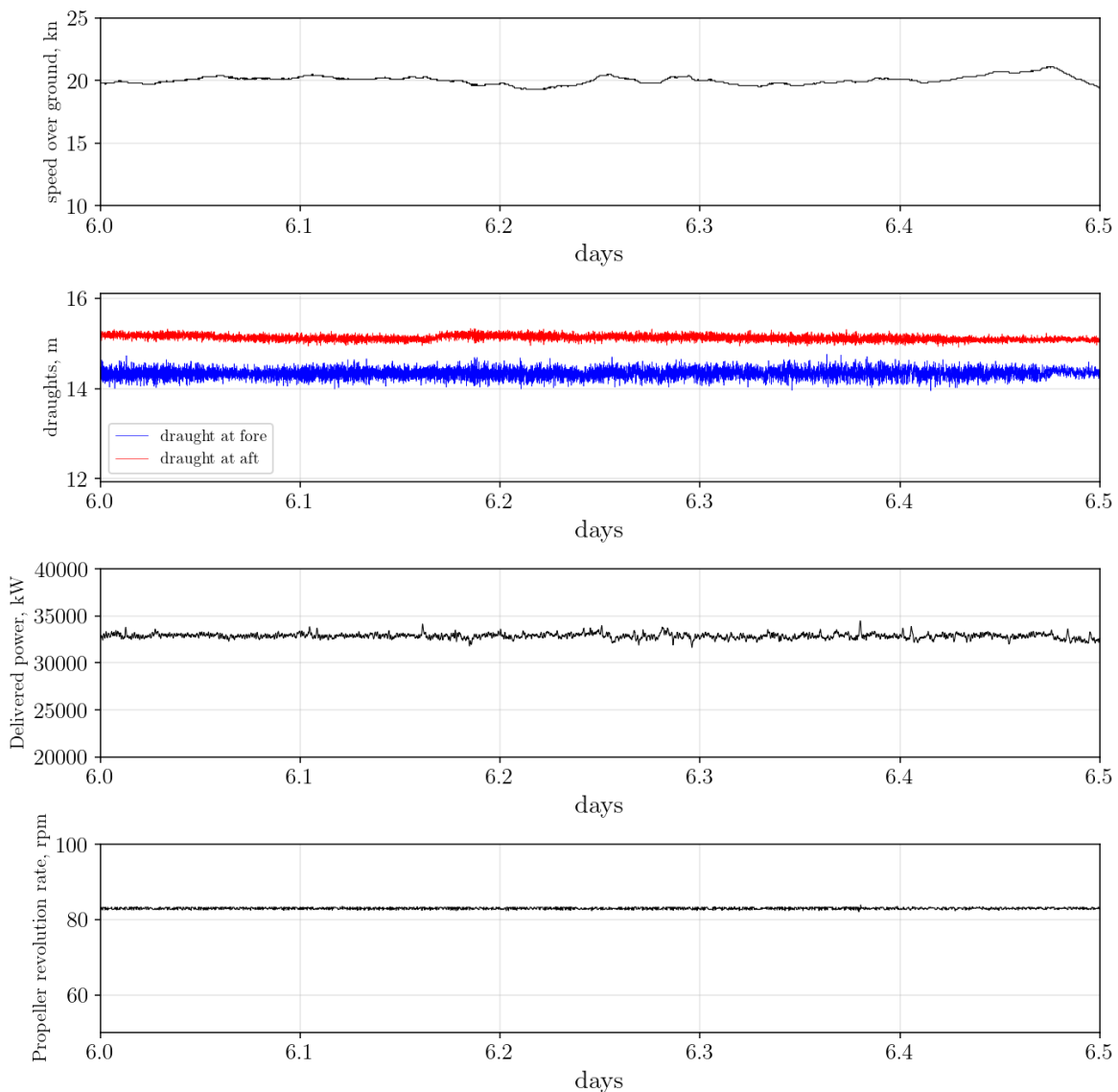


Figure 24: Validation dataset of environmental onboard measurements

The validation procedure is done in a similar manner as in (Kim and Tezdogan, 2022).

Two-dimensional computational grid is constructed with the same geometric attributes to be used in RSS simulations, where only one cell pointed in the transverse direction to significantly save computational time. Extents of the computational domain are also the same.

Wave height is tracked at a single position that corresponds to the ship fore perpendicular. As the ship is navigating in deep waters, following the assumption that the sea is fully developed, Pierson-Moskowitz Spectrum (PM) wave spectrum is chosen (Pierson and Moskowitz, 1964). The mathematical formulation of the spectrum is as follows:

$$S_{\zeta}(\omega) = \frac{\alpha_{\text{pm}} \cdot g^2}{\omega^5} e^{-\beta \left(\frac{g}{v_{\text{pm}} \omega^2}\right)^4} \quad (57)$$

with coefficients  $\alpha_{\text{pm}}$  and  $\beta$  as follows:

$$\alpha_{PM} = 4 \cdot \pi^3 \left( \frac{H_{1/3}}{g\overline{T}_z} \right)^2 \quad (58)$$

$$\beta = 16 \cdot \pi^3 \left( \frac{V}{g\overline{T}_z} \right)^4 \quad (59)$$

Where  $\overline{T}_z$  is the mean zero-crossing period and  $v_{\text{pm}}$  is the wind speed measured at a standard height of 19.5 m above sea level. Individual wave components that are necessary for the boundary conditions in OpenFOAM are calculated following the standard spectral relations. Distribution of wave amplitudes is modelled as:

$$\zeta_a = \sqrt{2 \cdot S_{\zeta}(\omega) \cdot \Delta\omega} \quad (60)$$

where  $\Delta\omega$  is the constant difference between consecutive angular frequencies. For the random distribution of wave amplitudes in time domain, Equation 61 is used:

$$\zeta_i = \sum_{i=1}^N (\zeta_a \cos(\omega t + \phi)) \quad (61)$$

where  $N$  is the number of wave components, while  $\phi$  is the random phase shift, i.e., a random number in the range of  $[0 : 2\pi]$ . Computational grid in the vicinity of the free surface is refined, having a cell height of approximately 0.156 m and cell length of 1.25 m. Clearly, the duration of the irregular sea state is far to short to obtain the exact spectrum

shape. Considering the expected cell count in the 3D simulations, a balance between computational costs and wave spectrum accuracy needs to be accounted for.

Also, having in mind that the measurements provide only a single value of the  $H_{1/3}$ , insisting on a high resolution wave spectrum is not entirely justified. Nevertheless, it is necessary to obtain correct statistical values of the spectrum from CFD, measures that compared reasonably favorable to theoretical ones. Significant wave height and zero-crossing period are reproduced with Eqs. (62) and (63), respectively.

$$H_{1/3} = 4 \cdot \sqrt{m_0} \quad (62)$$

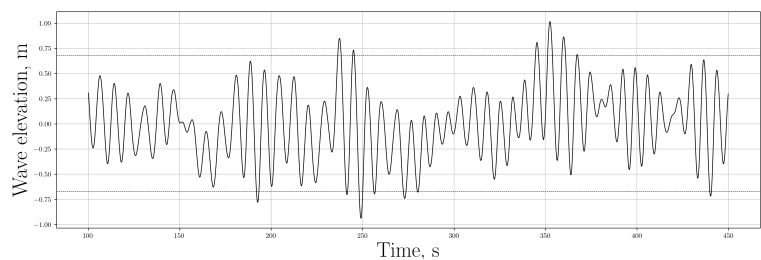
$$\bar{T}_z = 2\pi \sqrt{\frac{m_0}{m_2}} \quad (63)$$

where  $m_0$  and  $m_2$  are spectral moments, defined as:

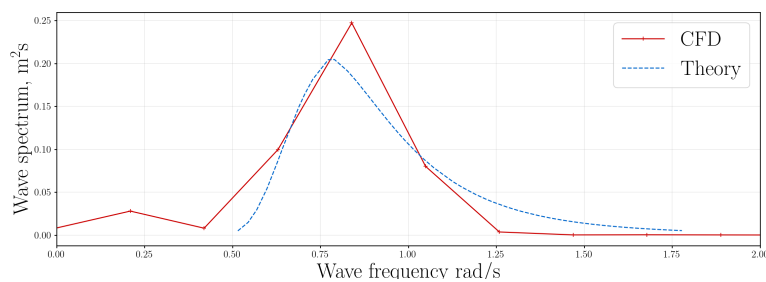
$$m_0 = \int_0^\infty S_\zeta(\omega) d\omega \quad (64)$$

$$m_2 = \int_0^\infty \omega^2 S_\zeta(\omega) d\omega \quad (65)$$

Wave elevations in time domain with corresponding wave spectrum are shown in Figure 25.



(a) Wave elevations in time domain



(b) Theoretical and CFD computed wave spectrum

Figure 25: Wave elevations in time domain with recreated wave spectrum

In Table 6 statistical measures of the wave spectrum from numerical results against theoretical value are given. The last column indicates the percentage of difference from numerical result from theory, denoted with  $E$ .

Table 6: Comparison of numerical and theoretical spectrum statistics

	$H_{1/3}$ , m	$\overline{T_z}$ , s
Theory	1.31	6.359
CFD	1.23	7.78
E, %	6.1	18.2

The computed significant wave height based obtained by CFD slightly differs from theory, while the zero-crossing period deviates by 18%. This is attributable to the grid being too coarse in the longitudinal direction. However, the computed wave period is well within the range of the representative sea state therefore, it is not an imperative to strictly insist on a close accuracy with theoretical values but rather with representative range. Also, a slight difference in the peak of the spectrum is a consequence of mesh resolution.

A somewhat larger low frequency content in the computed spectrum ( $\omega < 0.25$ ) might be a consequence of a negligible wave reflections from the domain's outlet boundaries. Besides, as only a limited number of wave components are considered, the energy at the spectrum's right side decayed faster. To resolve these discrepancies, extensive additional simulations would have been necessary, leading to a dramatic increase in computational time.

Therefore, a compromise between accuracy and limited computational resources is sought. After achieving satisfactory results in two-dimensional simulations, three-dimensional simulation in irregular sea state can be approached, which is the subject of the next chapter.

#### 5.4.2 Results of a Simulation in a Representative Sea State

The ship's loading condition, speed, propeller revolution rate, and main engine power during this period are summarized in Table 7.

Table 7: Features of the ship and propeller in navigation

Parameter	Unit	Symbol	Value
Draught at aft	m	$T_A$	15.35
Draught at fore	m	$T_F$	14.5
Displacement	t	$\Delta_{nav}$	191000
Longitudinal mass moment of inertia	$m^2kg$	$I_{55}$	$6.133 \cdot 10^{10}$
average speed	knots	$V_{nav}$	19.8
Propeller revolution rate	rpm	$n_{nav}$	83
average shaft power	kW	$P_{Dnav}$	33028

Comparison of the CFD results with onboard measurements of the delivered power, normalized pitch angle  $\theta$  and heave  $\eta_3$  at  $CoG$  is shown in Figure 26.

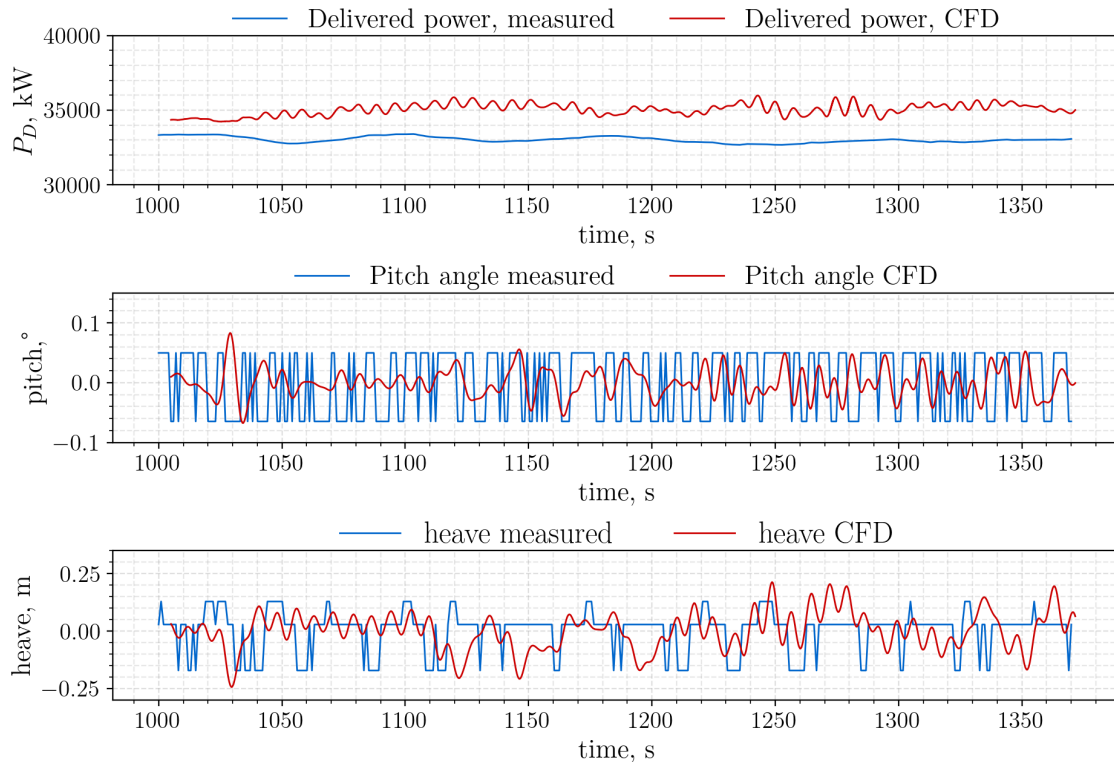


Figure 26: Comparison of CFD results and onboard measurements

The numerical simulation strategy consists of two phases. First, a calm water simulation is conducted for  $10^3$  seconds until forces and flow field reached steady convergence. After

that, the simulation continues with updated boundary conditions for inlet and outlet to generate and absorb irregular waves.

For the second phase, the temporal discretization scheme is switched to second-order backward differencing scheme, and the time step is reduced to  $1.5^{-3}$  seconds to better capture wave-hull interactions. For the purpose of the meaningful graphical representation, pitch  $\theta$  and heave  $\eta_3$  have been normalized with their mean value. Table 8 summarizes the results and corresponding statistical metrics. Alongside mean value, standard deviation is defined as  $\sigma$  while the amplitude range is denoted as  $A_{P-P}$  (peak-to-peak).

Table 8: Comparison of onboard measurements and CFD

<b>Parameter</b>	<b>Unit</b>	<b>Mean</b>	$\sigma$	$A_{P-P}$
Delivered power, measured	<i>kW</i>	33028.79	195.929	721.98
Delivered Power, CFD	<i>kW</i>	34388.79	386	1751.92
pitch $\theta$ measured	$^\circ$	1.481	0.056	0.114
pitch $\theta$ CFD	$^\circ$	0.153	0.023	0.1507
heave $\eta_3$ measured	m	1.883	0.091	0.300
heave $\eta_3$ CFD	m	0.272	0.089	0.456

The mean value of the signal offers a robust measure to capture the tendency of the time-averaged characteristics while the standard deviation provides insights in non-stationary nature of ship dynamics in waves. Amplitude range is selected as it can show potential extreme values in the signals although which are not explicitly expected in these RSS conditions. These statistical metrics provide direct physical interpretations of both numerical and measured signals. The comparison of the main engine power shows that while the CFD model captures the high-frequency fluctuations due to wave-induced inflow into the propeller plane, the measured data exhibits a more stable behaviour. The CFD results capture the general trend but overestimate the mean by approximately 4.1%.

Also, the CFD model exhibits significantly higher variability, with a standard deviation of 386 kW compared to the measured 195.929 kW. This is also reflected in the peak-to-peak range  $A_{P-P}$ , where the CFD predicts power fluctuations of 1751.92 kW, more than twice the measured range of 721.98 kW. The pitch angle predictions agreed reasonable well

with measurements in terms of frequency, though the CFD model produced smoother transitions compared to the more discrete measured data points. Both measured and predicted values oscillate within a range of approximately  $\pm 0.05^\circ$ . The measured mean pitch is  $1.481^\circ$ , while the CFD predicts  $0.153^\circ$ . The interpretation of the mean pitch angle can be deduced to the value of mean dynamic trim.

The measured pitch shows higher variability of ( $0.056^\circ$ ) compared to CFD ( $0.023^\circ$ ). However, the CFD model predicts a larger motion range of  $0.1507^\circ$  versus the measured  $0.114^\circ$ . Heave amplitude comparisons indicate that the CFD model captures the general magnitude of  $\pm 0.2\text{m}$ , although some phase differences occurred between predicted and measured heave values. The CFD results show more continuous motion patterns compared to the sharp discontinuities seen in the measured data. Regarding statistical analysis, there's a substantial difference in mean values, with measurements showing  $1.883\text{ m}$  compared to CFD's  $0.272\text{ m}$ .

The standard deviations are quite similar ( $0.091\text{ m}$  measured vs  $0.089\text{ m}$  CFD), indicating comparable motion variability. The CFD predicts a larger heave motion range of  $0.456\text{ m}$  compared to the measured  $0.300\text{ m}$ . As the measured values of ship dynamics have small absolute values, the stepped nature of the signals might be addressed to the IMU sensitivity, optimal sampling rate etc. It should be emphasized that the integrity of the measurements is ensured by using industry-certified sensors that undergo regular calibration with strictly known tolerances. Figure 27 shows computed free surface, with clear distinction of incident and radiated wave field.

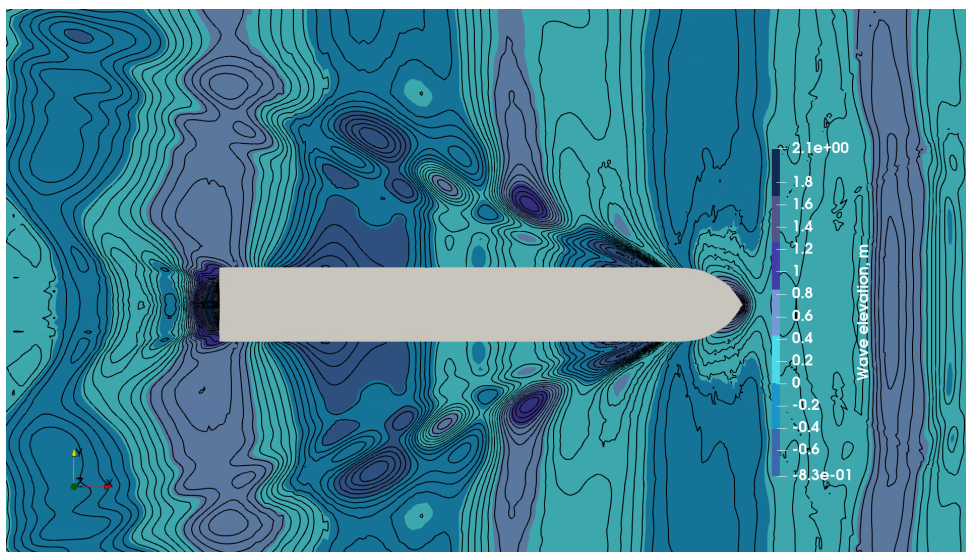


Figure 27: The surrounding wave field of the ship operating under RSS conditions

Until now, ship propulsion has been analyzed only in terms of delivered power. In order to obtain meaningful insights into full scale propulsive efficiency in waves, propulsion coefficients are calculated based on the methodology presented in Chapter 4.

The results of the propulsion coefficients in calm water and in RSS are presented in Table 9. It is important to emphasize that the values reported for RSS conditions are derived by averaging the instantaneous values over the entire simulation period of 360 s, which is determined to be sufficient to capture the mean propulsive characteristics in the given wave conditions.

Table 9: Propulsion coefficients comparison

<b>Parameter</b>	<b>Symbol</b>	<b>Calm Water</b>	<b>RSS</b>
Resistance, kN	$R_T$	2282.84	2316.17
Thrust, kN	$T$	2647.06	2721
Thrust deduction fraction	$t$	0.138	0.145
Wake fraction	$w$	0.208	0.259
Open water efficiency	$\eta_0$	0.651	0.6058
Hull efficiency	$\eta_H$	1.121	1.119
Quasi-propulsive efficiency	$\eta_D$	0.73	0.678

The resistance increased from 2282.84 kN in calm water to 2316.17 kN in RSS conditions, corresponding to a 1.5% increase. This increase is accompanied by a higher thrust requirement, rising from 2647.06 kN to 2721 kN (2.8% increase) in RSS. The wake fraction showed a notable increase from 0.208 in calm water to 0.259 in RSS, representing a 24.5% change. The thrust deduction fraction similarly increased from 0.138 to 0.148. The open water efficiency decreased from 0.651 to 0.6058, while the hull efficiency showed a minor reduction from 1.121 to 1.119.

These changes resulted in a reduction of total propulsive efficiency from 0.73 in calm water to 0.678 in RSS conditions, representing a 7.1% decrease in quasi-propulsive efficiency when operating in a representative sea state. This concludes the chapter on numerical modelling in full-scale. Next chapter deals with comprehensive assessment of propulsion characteristics in model-scale while using both AD and CSM propulsion models.

## 6 NUMERICAL MODELLING OF SHIP PROPULSION IN MODEL SCALE

This chapter presents numerical investigation of ship propulsion characteristics in model-scale using the Duisburg Test Case (DTC) container ship model. The work builds on experimental data from tests conducted at SINTEF in Trondheim, Norway, where the model was tested at 1:63.65 scale in both calm water and regular wave conditions. Two different numerical approaches for modeling the propeller are compared: the Actuator Disk (AD) method and the Coupled Sliding Mesh (CSM) method with fully resolved propeller geometry.

The chapter begins with a description of the experimental setup and test conditions, followed by self-propulsion simulations in calm water that establish a baseline for understanding propeller performance. The numerical methods are then applied to three regular wave cases with constant steepness but varying wavelengths, ranging from 0.19 to 0.46 times the ship length. Results are presented in terms of thrust and torque coefficients, including both mean values and oscillation amplitudes at the encounter frequency. The physical differences between the two propulsion modeling approaches are examined through flow field visualizations and frequency analysis. Finally, propulsive coefficients in waves are calculated and analyzed to provide insight into how hull-propeller interactions change in different wave conditions and how well each numerical method captures these effects.<sup>2</sup>

### 6.1 Experimental Data in Model Scale

The experimental model-scale setup used in this study originates from (el Moctar et al., 2012) in which the hull model is known by the acronym DTC. An extensive experimental campaign has been performed in SINTEF, Europe's largest independent research organization located in Trondheim, Norway. For details of the experiments, reader is referred to (Rabliås, 2022; Rabliås and Kristiansen, 2022). The Oqus position system is used for measurements of rigid body motions while the dynamometer is used for measuring thrust and torque. The white markers necessary for the Oqus system, along with the umbilical cord providing

---

<sup>2</sup>Part of this chapter has been published in I. Sulovsky, A. Bakica, and J. Prpić-Oršić. CFD assessment of ship propulsion and propeller-hull interactions in waves using low and high fidelity approach. *Ocean Engineering*, 346:123843, 2026. ISSN 0029-8018. doi: doi.org/10.1016/j.oceaneng.2025.123843

power and data transfer, are presented in Figure 28. The model, at a scale of 1:63.65, is equipped with a 5-bladed fixed-pitch propeller and a twisted rudder with Costa bulb, as seen in Figure 29a. To prevent potential water overflow, a breakwater section is mounted on the model, Figure 29b. The experiments are carried out in a free-running manner, utilizing an autopilot system for the correction of the rudder angle to keep the model on course. The experimental configuration is the same for calm water and wave conditions.

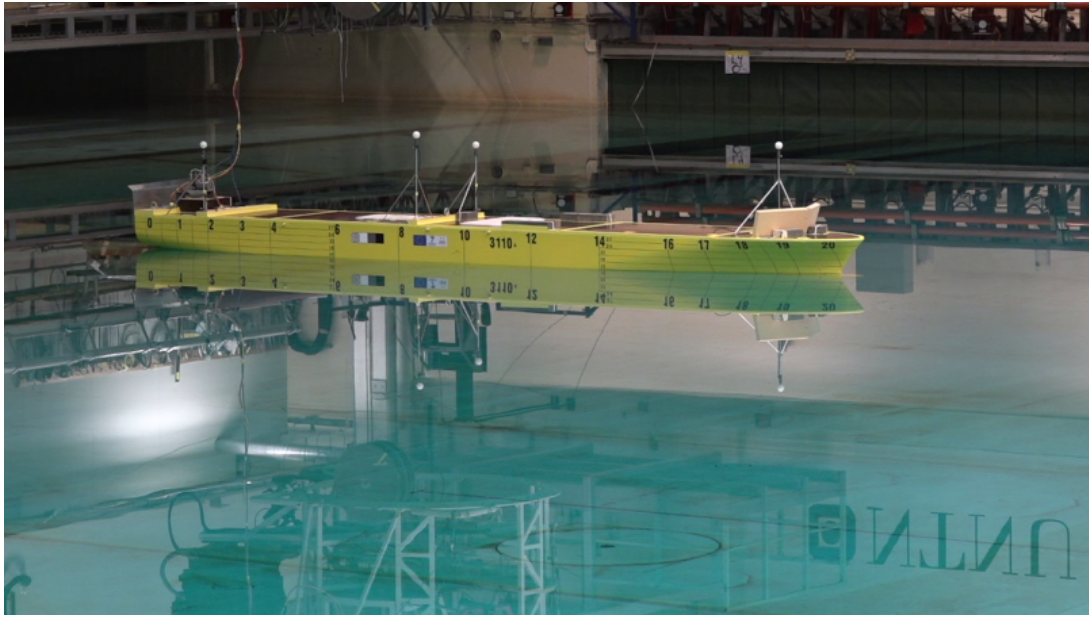
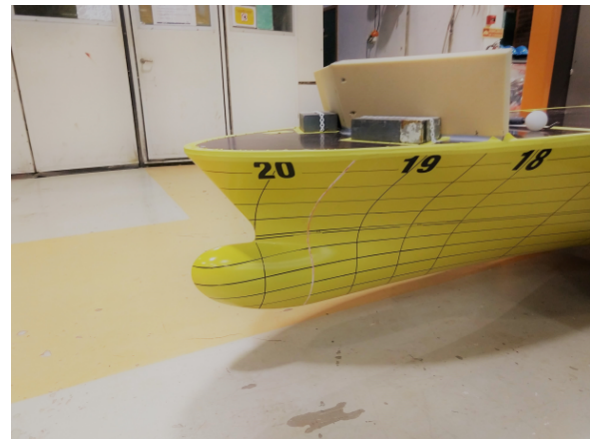


Figure 28: Experimental DTC model. Reprinted from (Rabli s, 2022) with permission of the author



(a) Model appendages at the aft



(b) Bulbous bow with breakwater section

Figure 29: Aft and bow sections of the model. Reprinted from (Rabli s, 2022) with permission of the author

Main particulars and inertial characteristics of the model are listed in Table 10.

Table 10: DTC model particulars

Particulars	Unit	Symbol	Model
Length between perp.	m	$L_{PP}$	5.577
Breadth	m	$B$	0.801
Draft	m	$T$	0.228
Displacement	kg	$\Delta$	672.6
Block coefficient	-	$C_B$	0.661
Longitudinal centre of gravity	m	$LCG$	2.721
Transverse centre of gravity	m	$TCG$	0
Vertical centre of gravity	m	$VCG$	0.314
Metacentric height	m	$GM$	0.078
Transversal moment of inertia	kgm <sup>2</sup>	$I_{44}$	45.43
Longitudinal moment of inertia	kgm <sup>2</sup>	$I_{55}$	1266.330
Vertical moment of inertia (yaw)	kgm <sup>2</sup>	$I_{66}$	1268.4

As propeller open water data is required both for the AD propulsion model and for overall assessment of the hull-propeller interaction, open water curves are shown in Figure 30.

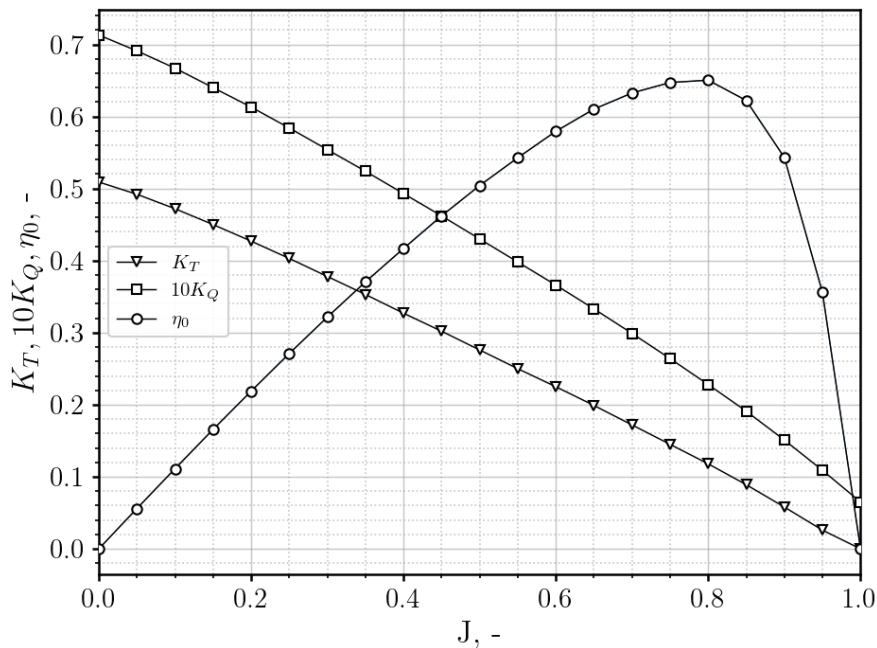


Figure 30: Open water curves of the DTC propeller

Self-propulsion tests in calm water are performed at a relatively low Froude number of 0.139, with constant propeller revolution rate at 11.5 rpm. Self-propulsion tests in regular waves are performed for three wave characteristics with constant wave steepness, as shown in Table 11. Such test matrix allows for systematic investigation of ship propulsion performance in waves along with corresponding hull-propeller interactions.

Table 11: Experimental test matrix for regular waves

Case	1	2	3
Wave height $H$ , m	0.060	0.087	0.119
Wave period $T_w$ , s	0.82	1.24	1.49
$H/L_{PP}$ , -	0.011	0.0157	0.0214
$\lambda_e/L_{PP}$ , -	0.187	0.303	0.46

## 6.2 Self-Propulsion Simulations in Calm Water

In the experimental campaign, self-propulsion tests in regular waves are preceded by self-propulsion tests in calm water. Therefore, numerical investigations are to follow the same approach. In this chapter, self-propulsion simulations in calm water with AD and CSM propulsion models are presented and compared with experimental data. Simulations are performed on two distinct mesh resolutions for both methods in order to address the uncertainties of the spatial discretization.

As computational resources are limited, the traditional Richardson extrapolation approach with three mesh densities is skipped. Using two mesh densities enabled to save computational time with having reasonable confidence in the results. Also, it is practically impossible to achieve mesh similarity between CSM and AD method due to their inherent requirements for the mesh in the stern region.

However, regions where high flow gradients are expected (free surface, bow, boundary layer) have the same topology in both CSM and AD simulations. Meshing is conducted using an embedded tool within OpenFOAM package, *snappyHexMesh*. Due to the coarser mesh in the stern region for the AD model, rudder geometry is slightly adjusted in order to properly discretize the boundary layer. Similar to previous chapter, computational domain is given in Figure 31, also following the geometrical differences of the domain extents from (ITTC, 2017a).

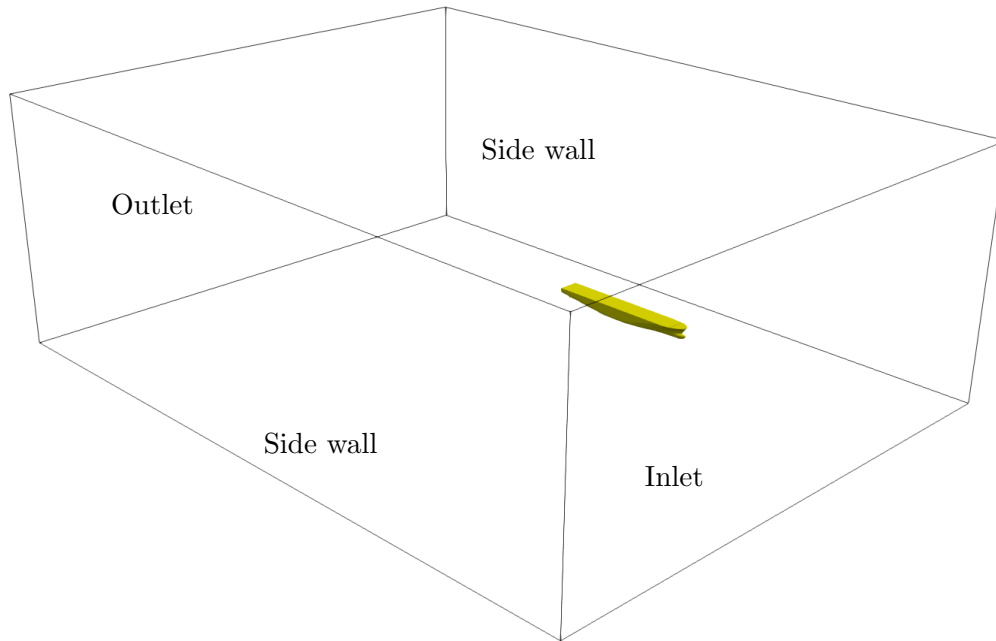
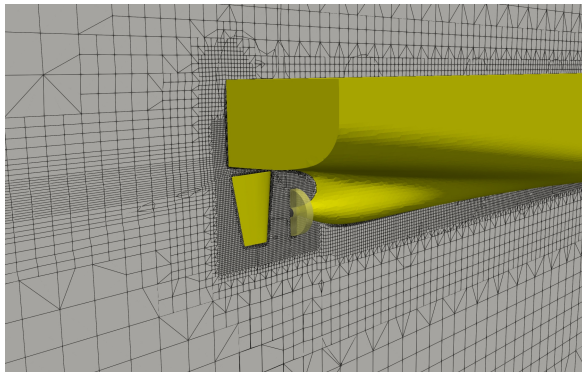
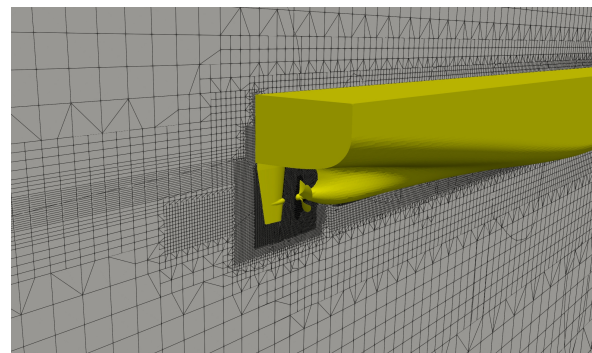


Figure 31: Boundaries of the computational domain for sea trial simulations

Stern regions for both methods are shown in Figure 32. The yellow cylinder in Figure 32a represents only a graphic visualization of the AD.



(a) Stern mesh region for the AD model



(b) Stern mesh region for the CSM model

Figure 32: Mesh regions for propulsion models

Extents of the computational domain are following the ITTC recommendations (ITTC, 2017a). For the AD model, coarse mesh consists of approximately  $2.2 \cdot 10^6$  computational cells while for the CSM model, mesh accounts with total of  $2.8 \cdot 10^6$  cells. For both models, boundary layer is discretized with 8 prism layers with an expansion ration of 1.1, while the height of the first adjacent cell to the hull is 0.8 mm.

Such geometry of the mesh in the boundary layer yielded a  $y^+$  of around 30. The discretized boundary layer at the bilge area of the hull is given in Figure 33.

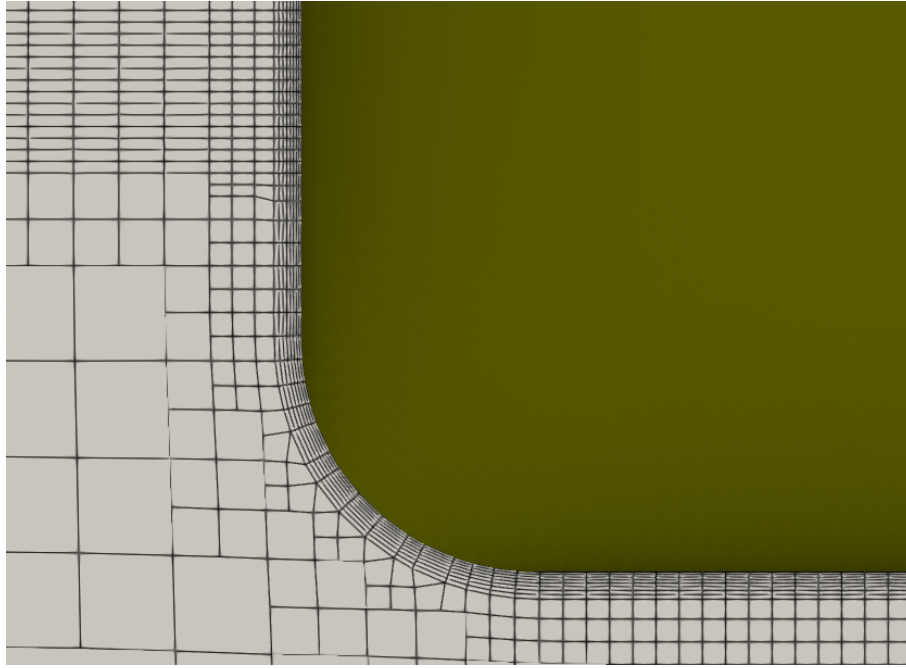


Figure 33: Discretized boundary layer at the bilge area of the DTC hull

Both meshes consist of 90% of the cells being hexahedral while the rest is mostly polyhedral.

Table 12: Results of self-propulsion simulations in calm water

	Experiment	CSM		AD	
		coarse	fine	coarse	fine
thrust $T, N$	14.126	14.965	14.321	13.903	14.116
resistance $R_T, N$	/	15.029	14.697	14.567	14.043
torque $Q, N_m$	0.323	0.327	0.311	0.320	0.3073
sinkage $\Delta T, m$	-0.0029	-0.0021	-0.0019	-0.0019	-0.002
trim $\theta, ^\circ (+ \text{bow up})$	-0.019	-0.042	-0.043	-0.041	-0.041

Observing the first row of the Table 12, it is evident that both CSM and AD method predict the thrust reasonably well. Fully discretized propeller yields a negligible over-prediction which can be attributed to the unstructured mesh type in the propeller region. Actuator disk shows slight underprediction of thrust opposed to experimental data, but with sufficiently small deviation.

Self-propulsion points are sufficiently accurate for both methods. Regarding the dynamic sinkage and trim, experimental values exhibit incredibly low sinkage amplitude

and trim angle. This can be attributed to a low Froude number of the model, well within displacement range. This is well supported by previous researchers (Roshan et al., 2020; Mahmoodi et al., 2023). This simulations demonstrated the effectiveness and accuracy of both propulsion models implemented in OpenFOAM in the context of self-propulsion tests in calm water. In the following chapter, self-propulsion tests in waves are presented.

### 6.3 Self-propulsion Simulations in Regular Head Waves

In this chapter, self-propulsion simulations in regular head waves with both AD and CSM model are presented. Self-propulsion simulations are preceded by simplified two-dimensional assessment of regular waves that conform to the experimental ones, in order to determine the sufficient grid size. Since there are three self-propulsion test in different wave heights, an attempt is made to perform the simulations on a single grid size, which significantly saves time in terms of manual workload needed for mesh creation.

#### 6.3.1 Assessment of Regular Waves in 2D

The accuracy of numerical seakeeping assessments within VOF framework is, among other factors, strongly dependent on obtaining the necessary wave height within the domain (Sulovsky et al., 2023b). Therefore, a simplified, time-affordable 2D simulations are conducted in order to determine the necessary grid size in the vicinity of the free surface. Height of the cell in vertical direction is approximately 3.9 mm while in the longitudinal direction is set to 30 mm. In this way, number of cells per characteristic wave height and wave length are given in Table 13.

Table 13: Grid characteristics for wave propagation study

Wave height, m	Encounter wavelength, m	Number of cells per wave height	Number of cells per wavelength
0.06	1.043	14	31
0.087	1.69	22	50
0.112	2.52	29	74

The proposed grid topology is well in line with recommendations given by (el Moctar et al., 2021). Stokes first order theory is set as the default wave model where the boundary

conditions, based on *olaFlow* package from (Higuera et al., 2013), are adapted to account for arbitrary current and wind speed. Successful implementation of such wave modelling is presented in (Sulovsky et al., 2025).

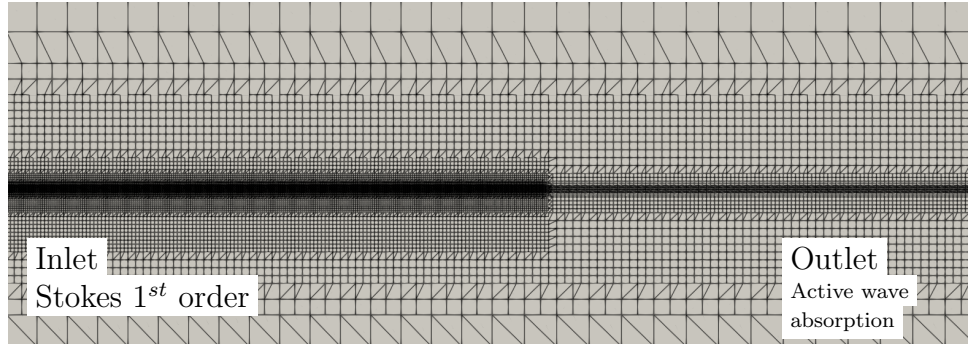


Figure 34: Computational domain for 2D wave propagation study

The mean Courant number is limited to 2, while the Courant number for the free surface advection is reduced to 1. This numerical restriction is satisfied by setting the time-step to  $5^{-3}$  s. Wave height is numerically tracked at the position of the ship's forward perpendicular. Achieved wave signal is shown in Figure 35.

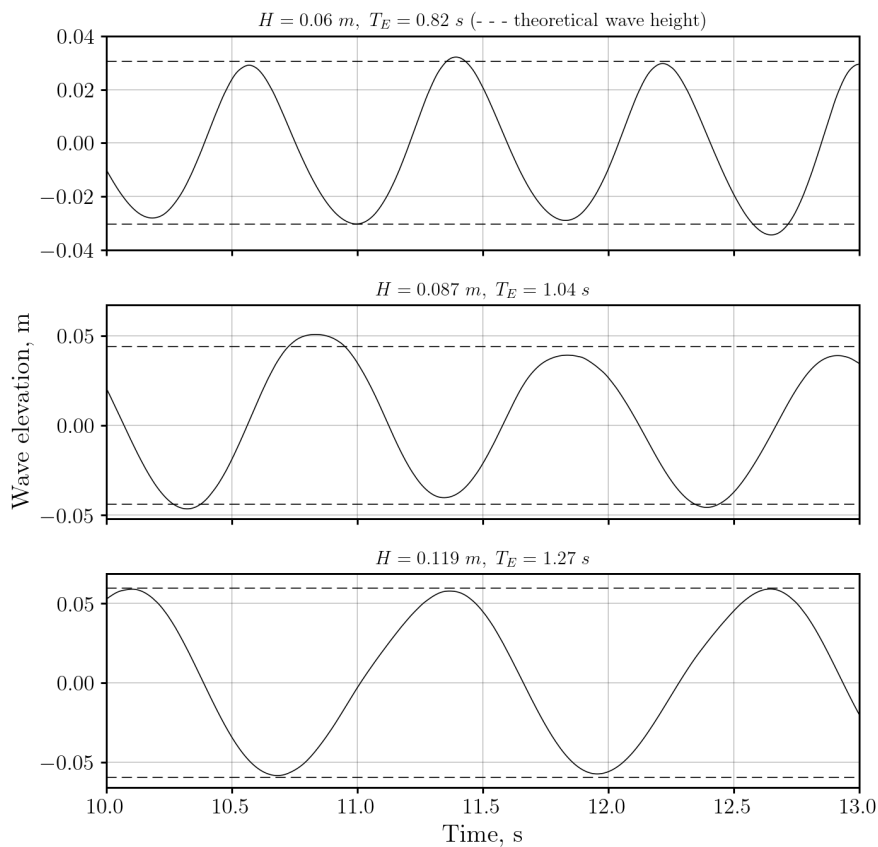


Figure 35: Results from the 2D wave propagation study

A mild oscillation of the wave trough and crest can be seen for the first case ( $H = 0.061\text{ m}$ ,  $\lambda_e/L_{PP} = 0.187$ ) which can be attributed to the active wave absorption. Also, as indicated in (Halder and Liu, 2025), numerical noise in CFD and even experimental difficulties are reported for short wave propagation.

Other two cases are showing consistent and sharp wave characteristics. This study showed that the complex, self-propulsion simulations in regular waves can be conducted on a single grid topology which significantly saves computational time. More details on this is followed in the next chapter, where the main results are presented.

### 6.3.2 Results of the Simulations

After having identified an adequate grid size, three-dimensional simulations can be conducted. Bottom and side views of the final computational grid, adequate for wave simulations are shown in Figure 36 and 37.

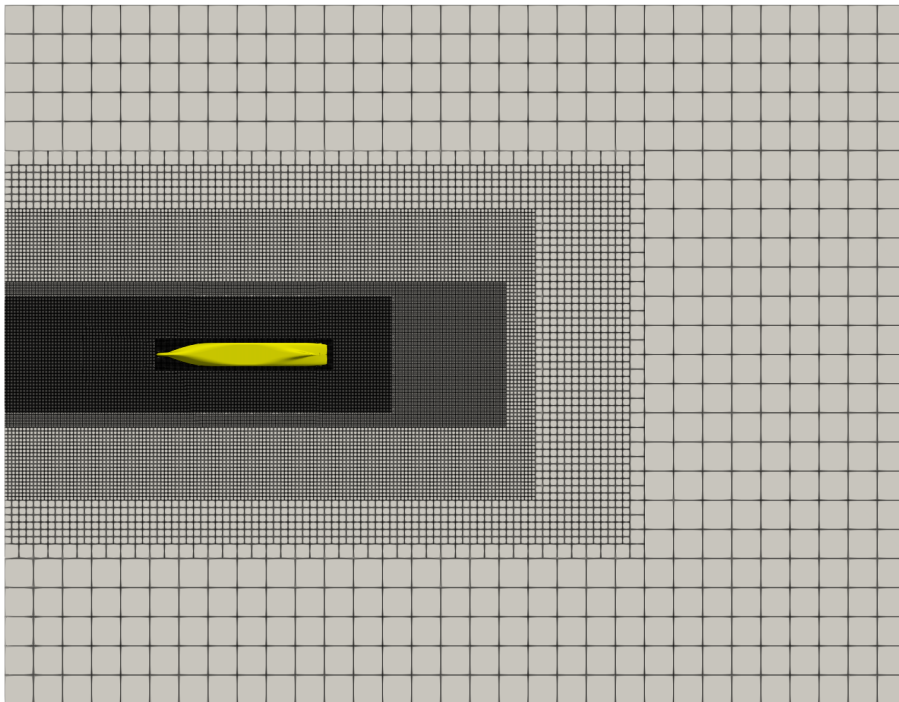


Figure 36: Computational grid for wave simulations - bottom view

Dense grid refinements are necessary in the proximity of the model for proper computations in waves. Anisotropic refinements of the grid in the free surface area necessary on both ends of the domain, due to numerical procedure of active wave absorption. Also, the domain extents in front of the model can be reduced since the corrective velocities from the wave boundary conditions are applied, if necessary.

The total cell count for the CSM grid is approximately  $7.2 \cdot 10^6$  while for the AD is  $6 \cdot 10^6$ . Besides the specific grid requirements, simulation conditions require added attention. In cases with rotating propellers and waves, two sets of motions need to be properly computed that have extremely different convergence times. For instance, the propeller motion, rotating at 11.5 rps and wave periods in the range of 1 s. Therefore, the simulation approach is as follows.

Firstly, the calm water conditions are initiated until flow field and forces converge without rotating the propeller. In the second step, head waves are initiated until ship motions stabilize. Only after that the propeller is set to motion with reduced time step in the CSM case, opposed to the previous step without rotating propeller. By doing so, reliable comparison between these two propulsion models is ensured. The similarity of the Courant number is also satisfied for both AD and CSM solution by adjusting the time step accordingly.

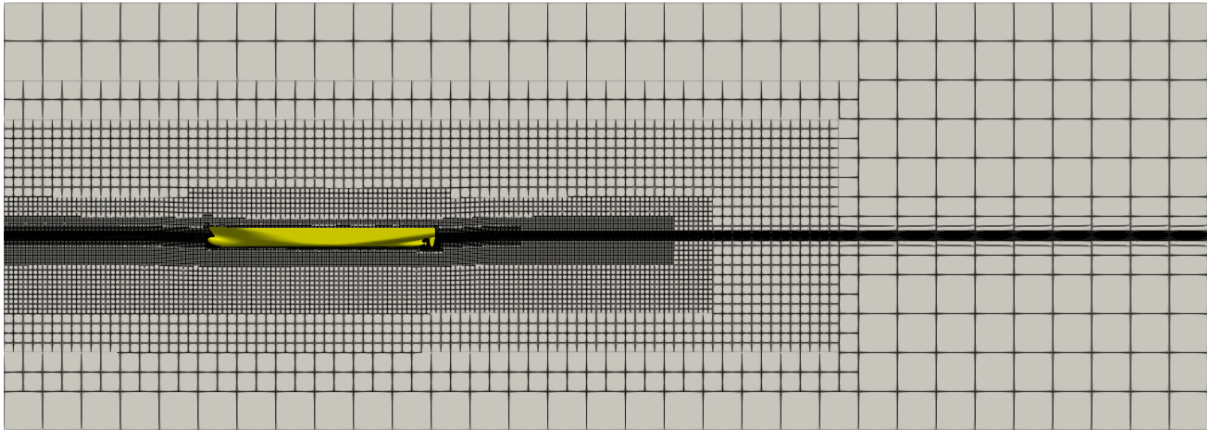


Figure 37: Computational grid for wave simulations - transversal view

In contrast with irregular waves, seakeeping results in regular waves are to be traditionally presented as Response Amplitude Operator (RAO). In general, RAO values represent the ratio between the ship's motion amplitude with respect to wave amplitude, showing which wave condition is causing the strongest response.

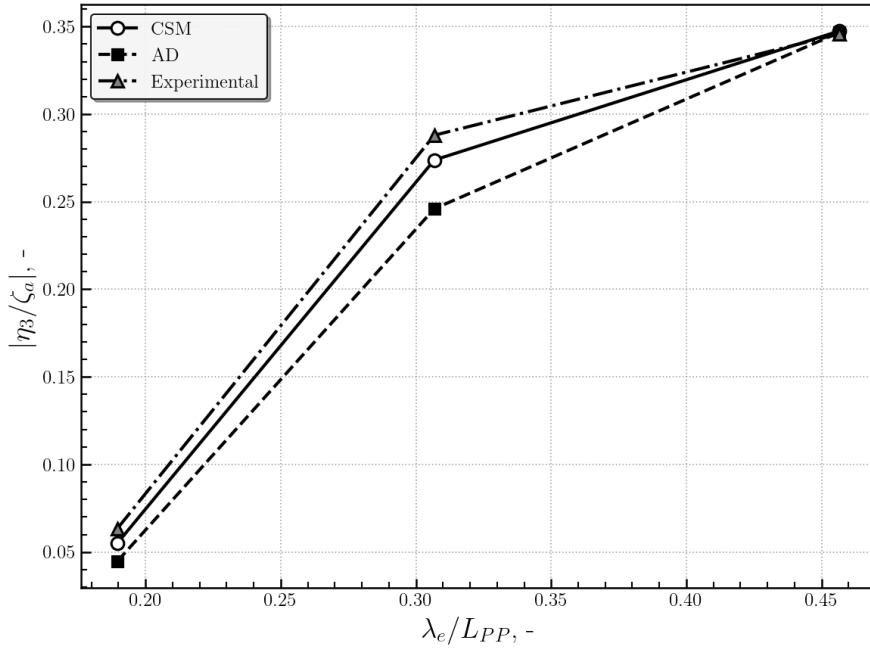
The literature is extensive on this matter; for more details on this, reader is referred to (Rawson and Tupper, 2001) and (Faltinsen, 1990). Values of RAO for heave and pitch are given in Figure 38, respectively. RAO for heave is calculated traditionally:

$$\text{RAO}_{\text{heave}} = \frac{\eta_3}{\zeta_a} \quad (66)$$

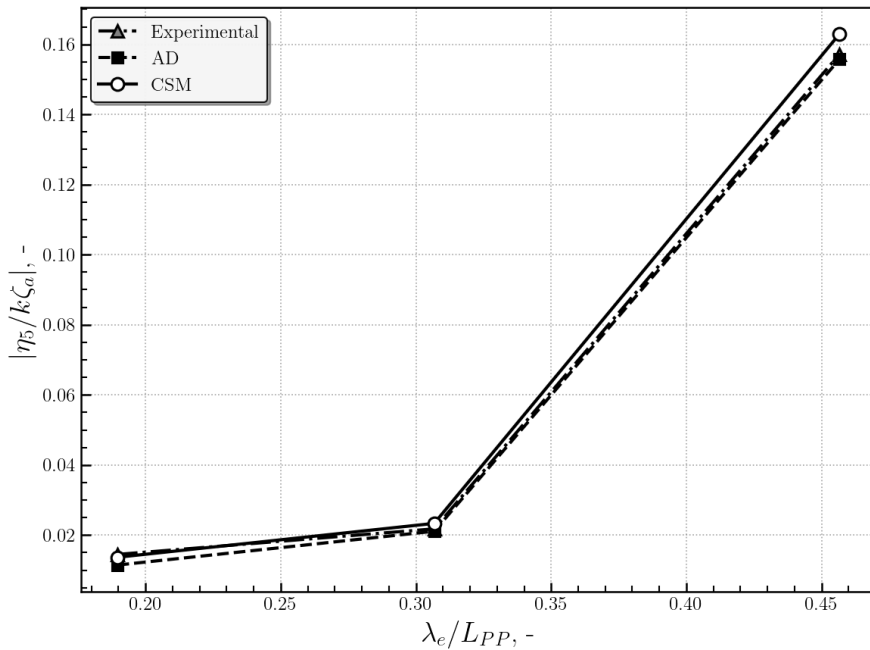
where  $\eta_3$  stands for heave amplitude. Pitch RAO is calculated similarly, with a normalization as follows:

$$\text{RAO}_{\text{pitch}} = \frac{\eta_5}{k\zeta_a} \tag{67}$$

where  $\eta_5$  refers to pitch amplitude while  $k$  is the wave number.



(a) Heave motion



(b) Pitch motion

Figure 38: RAO for heave and pitch motion

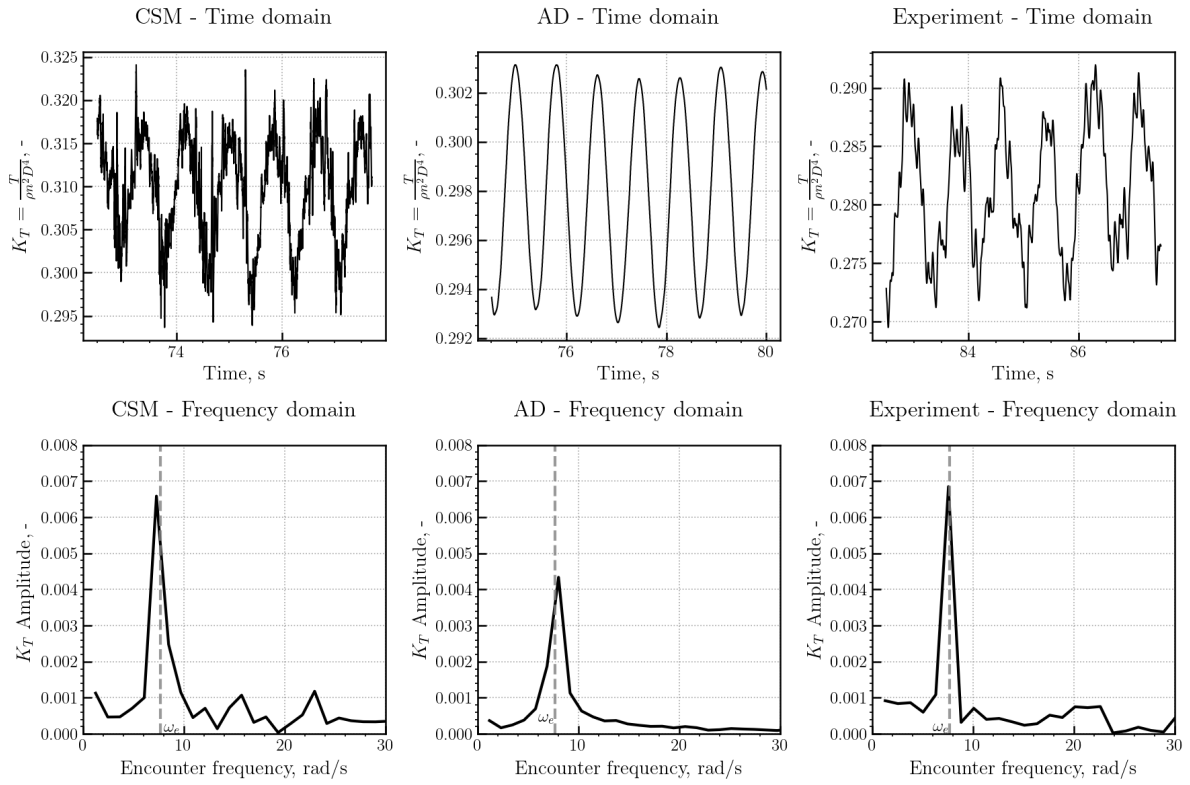
The dynamic response of the DTC model in head waves is similar on both AD and CSM grids while the strongest discrepancy can be seen for heave motion in the second wave case. This can be attributed to a relatively small absolute values of heave amplitudes that are approximately one centimeter for this case. Thus the difference between heave amplitude from AD grid and experimental heave is no more than 1.5 millimeters.

Also, the difference between CSM and experimental is the highest among other cases. The comparable RAO predictions between numerical models and experiments provide confidence in the overall simulation fidelity for subsequent detailed analysis. However, while the ship motion response validates the global hydrodynamic behaviour, the subtle differences in propeller modelling approaches become more pronounced when examining the unsteady loading characteristics.

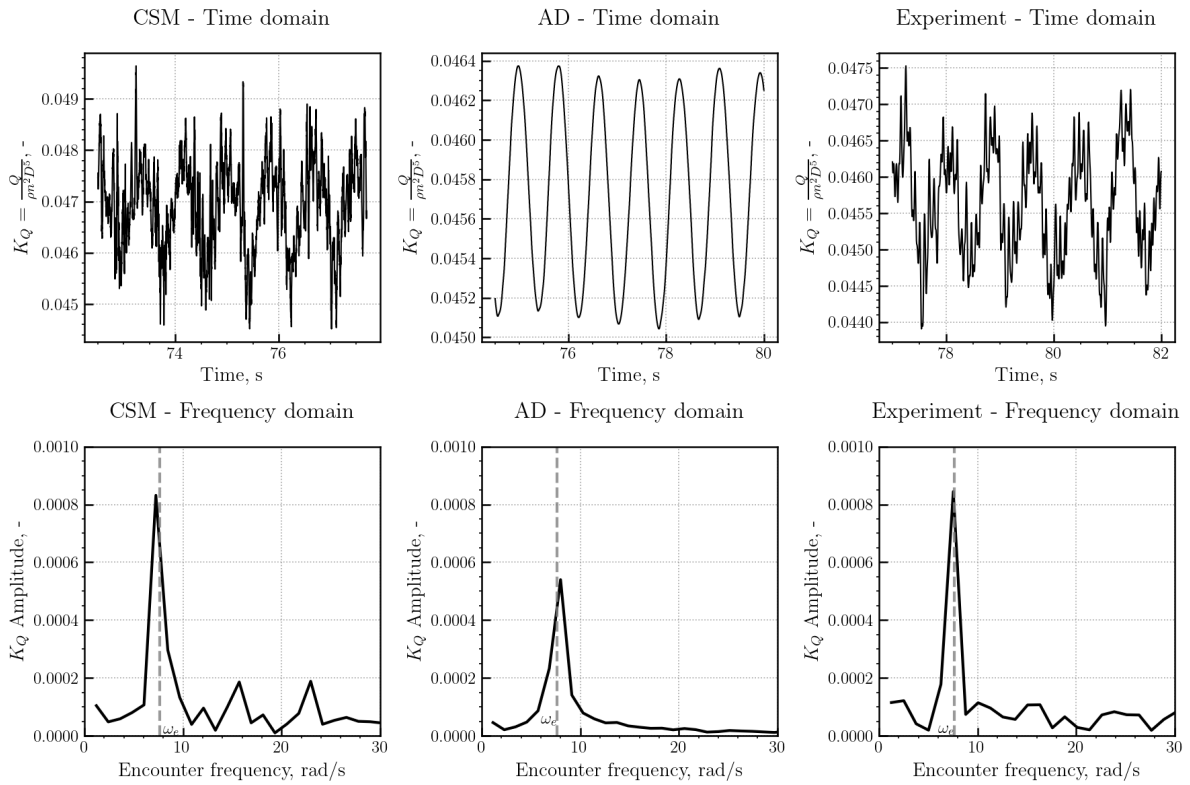
Therefore, a spectral analysis of the propeller thrust and torque time series are performed to reveal the harmonic content and frequency-dependent phenomena that distinguish the fully discretized CSM from the simplified AD representation. Time domain signals with corresponding frequency content for computed thrust with CSM and AD are shown in Figure 39a, 40a and 41a. Torque values are shown in the same manner, in Figure 39b, 40b and 41b.

On the frequency content plots, theoretical wave encounter frequency is indicatively plotted as  $\omega_e$ . Also, the scaling of the vertical axis in frequency plots is the same, as it is indicative of the amplitude range from both numerical models and experiment. Across all three datasets, numerical and experimental, a weak filtering of the time signals is employed. The Savitzky-Golay filter window is selected as 1/20th of the wave encounter period to preserve wave-induced propulsion oscillations while removing high-frequency numerical noise. This window is sufficiently small relative to the encounter frequency to maintain the physical wave-propeller interaction effects, while being large enough to smooth CFD numerical artifacts above the blade passing frequency of 11.5 rps.

Computed wave fields are given respectively in Figure 42a, 42b and 42c. Beyond its illustrative purpose, the wave elevation scale demonstrates satisfactory agreement with the target wave amplitude values, indicating that the simplified two-dimensional assessment provides a reasonable validation of the implemented approach.

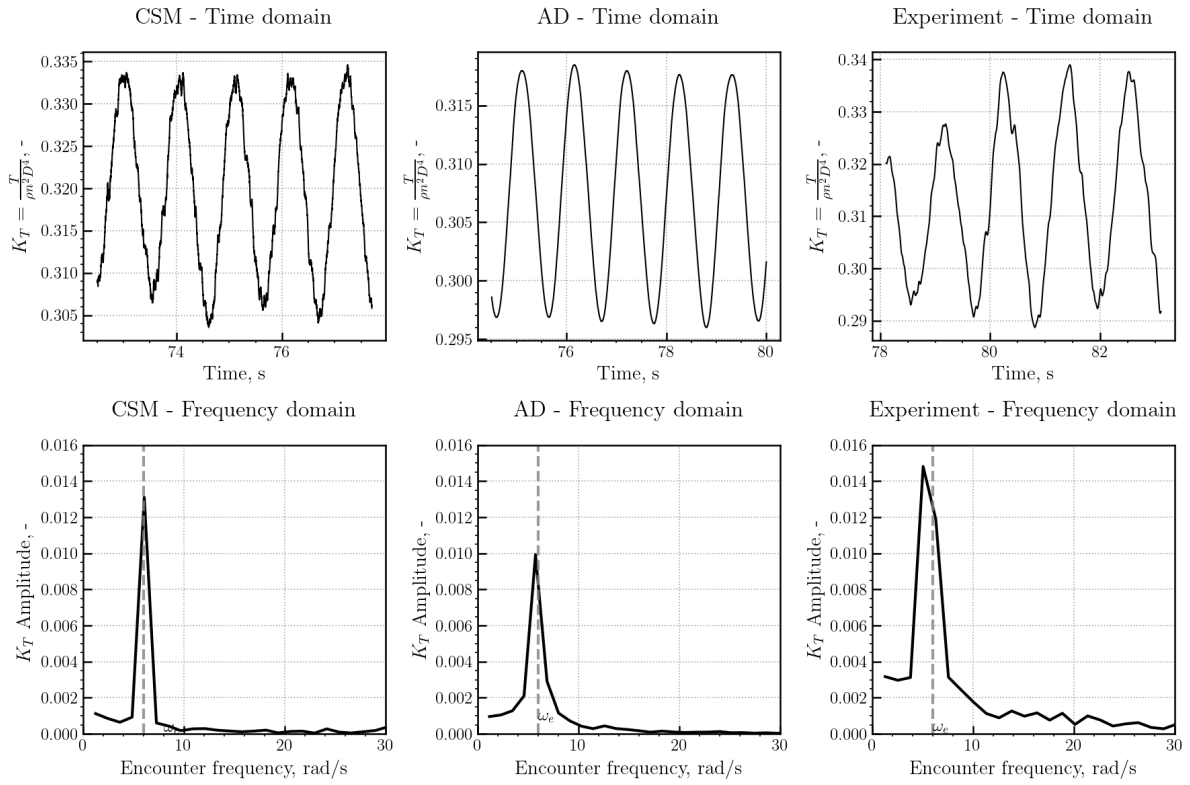


(a) Thrust

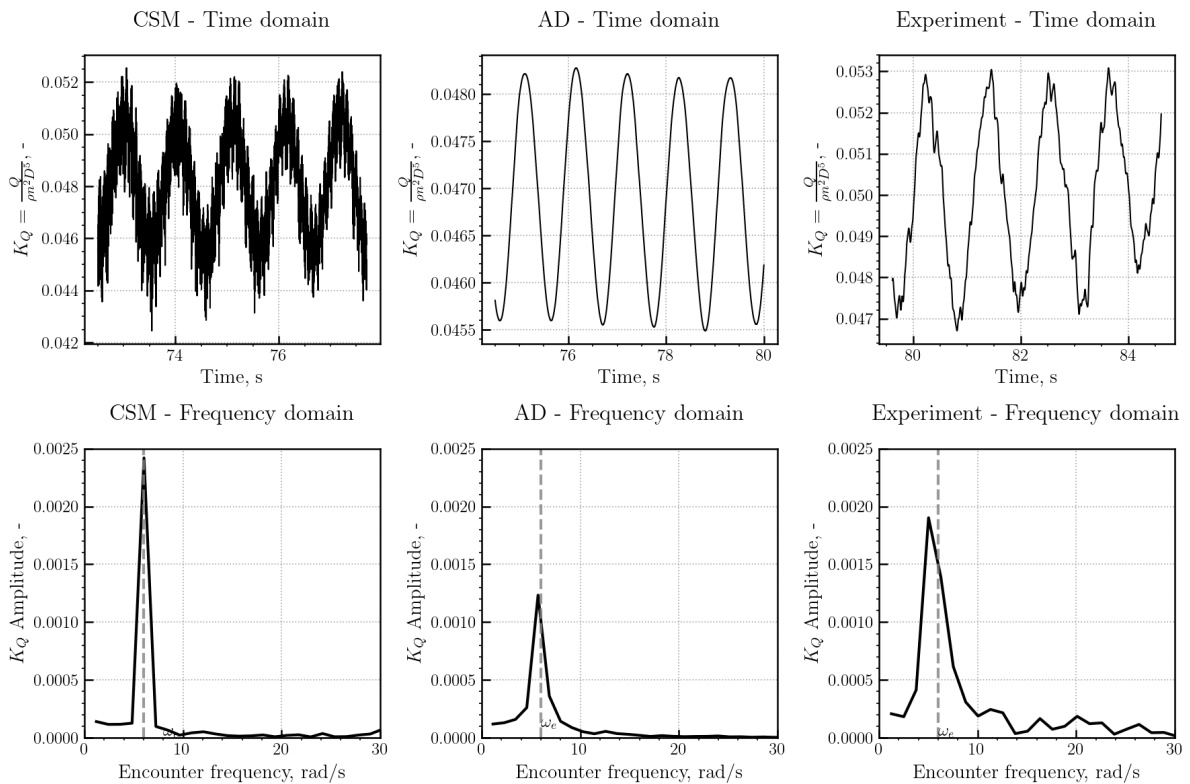


(b) Torque

Figure 39: Comparison of FFT results for  $H = 0.061 m$ ,  $\lambda_e/L_{PP} = 0.187$

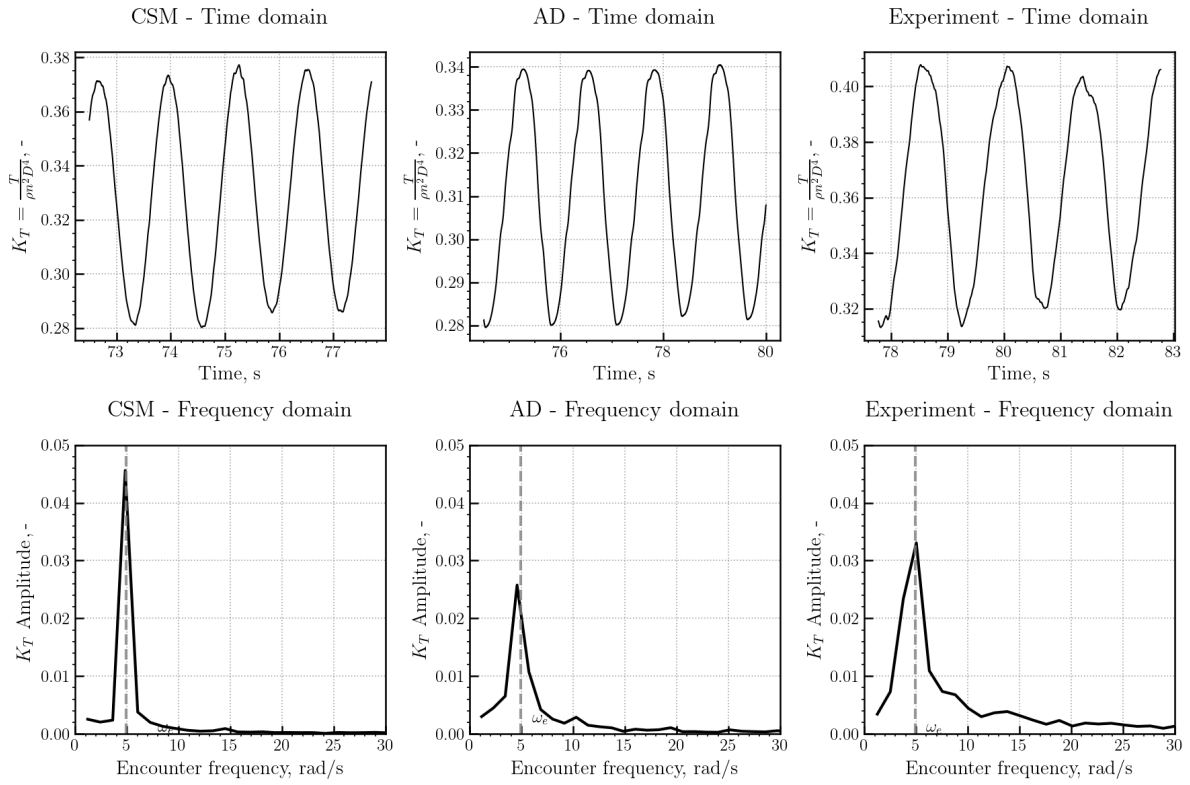


(a) Thrust

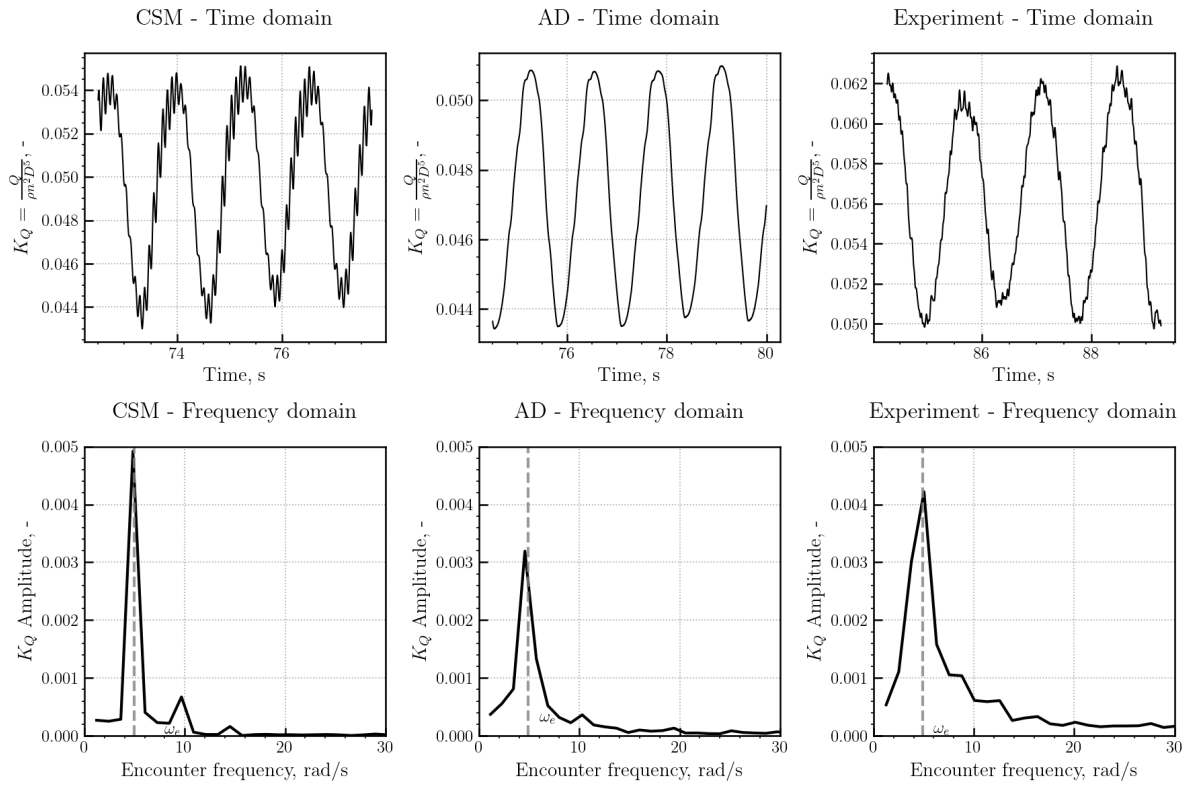


(b) Torque

Figure 40: Comparison of FFT results for  $H = 0.087 m$ ,  $\lambda_e/L_{PP} = 0.3$

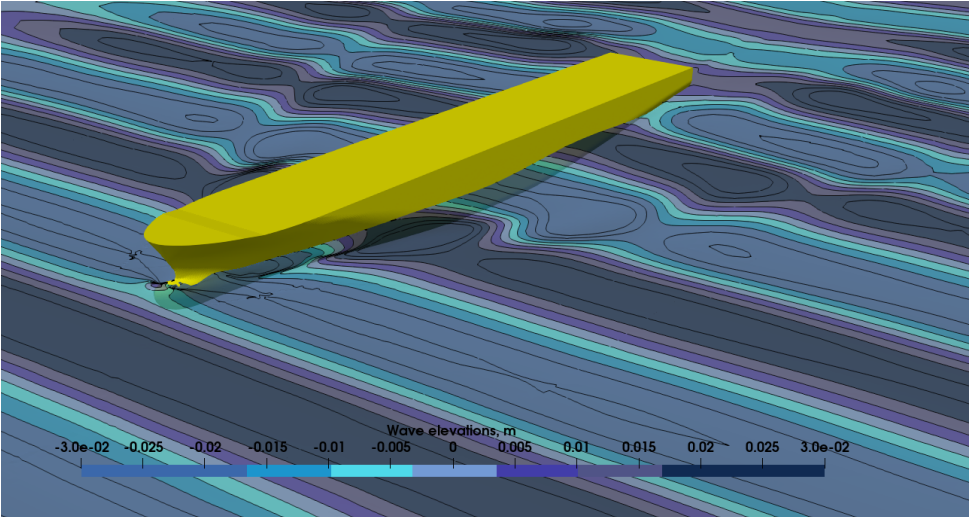


(a) Thrust

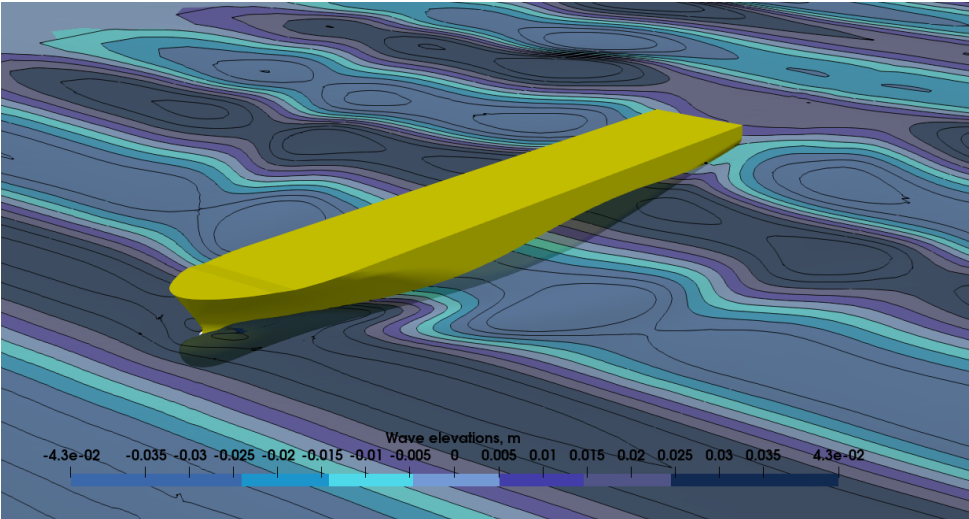


(b) Torque

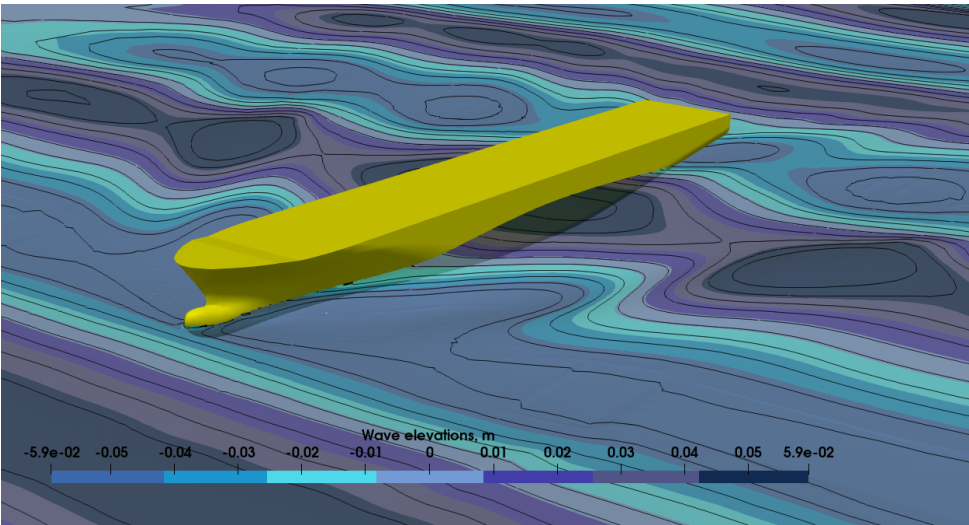
Figure 41: Comparison of FFT for  $H = 0.112 m$ ,  $\lambda_e/L_{PP} = 0.46$



(a)  $H = 0.061\text{ m}$ ,  $\lambda_e/L_{PP} = 0.187$



(b)  $H = 0.087\text{ m}$ ,  $\lambda_e/L_{PP} = 0.3$



(c)  $H = 0.112\text{ m}$ ,  $\lambda_e/L_{PP} = 0.46$

Figure 42: Computed wave fields for different wave conditions

For clarity, value of the first harmonic computed with Discrete Fourier Transform (DFT) from CSM, AD and experimental measurements of the thrust and torque coefficients are given in Figure 43.

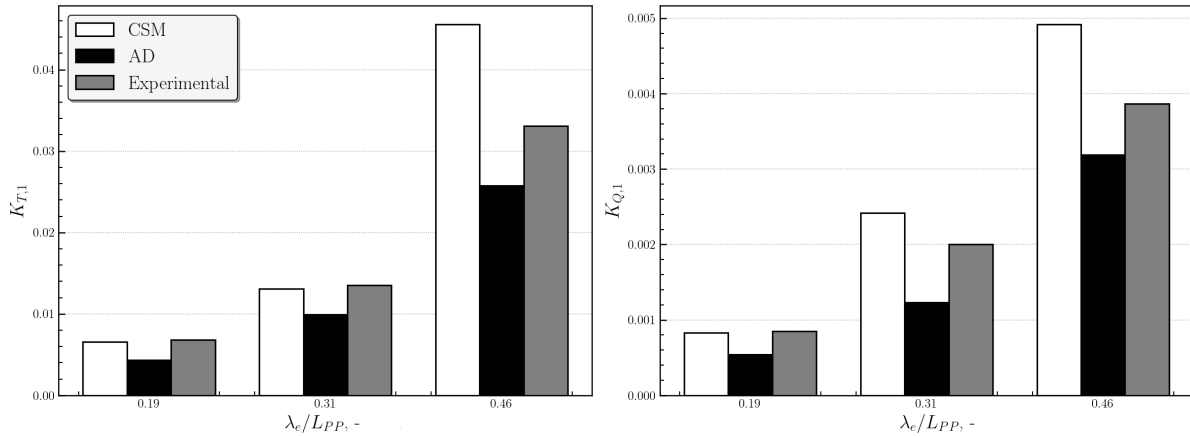


Figure 43: Value of the first harmonic for thrust and torque coefficients

The first harmonic analysis reveals patterns in the mean propeller loading across different wave conditions and modelling approaches. For the 1<sup>st</sup> harmonic of the thrust coefficient  $K_{T,1}$  (left), both numerical models demonstrate relatively consistent amplitudes across wavelengths, with magnitudes of  $K_T$  ranging from approximately 0.004 to 0.042. The CSM model consistently predicts the thrust amplitude more similar with the experiment, but with slight overprediction at the longest wavelength ratio ( $\lambda_e/L_{PP} = 0.46$ ) where it reaches 0.042. The AD model consistently shows lower values than the experimental ones, while experimental measurements exhibit the lowest thrust amplitude at shorter wavelengths but increase significantly at  $\lambda_e/L_{PP} = 0.46$ .

The 1<sup>st</sup> harmonic of the torque coefficient  $K_{Q,1}$  (right) displays more pronounced variations between methods and wavelengths. At the shortest wavelength ( $\lambda_e/L_{PP} = 0.19$ ), all three approaches yield similar low values of  $K_Q$  around 0.0007. However, substantial differences emerge at longer wavelengths. The experimental data shows a dramatic increase in torque amplitude, reaching approximately 0.0038 at  $\lambda_e/L_{PP} = 0.46$ .

In contrast, both numerical models maintain relatively stable torque levels across wavelengths, with the CSM model showing a strong increase to 0.0047 at the longest wavelength, while the AD model exhibits the smallest variation, reaching only 0.0032. Significant discrepancy occurs at  $\lambda_e/L_{PP} = 0.46$ , where CSM model exceeds both experimental measurements and AD model. Analogous to the first harmonic, mean value of the thrust

and torque coefficients are depicted in Figure 44. Loading of the propeller in calm water, self-propelled state from the experimental measurements is indicated with red line.

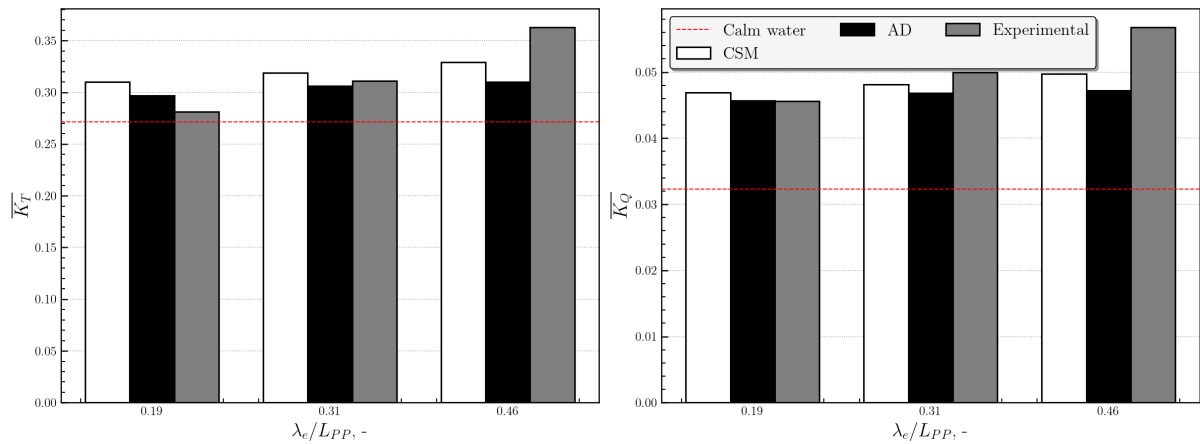


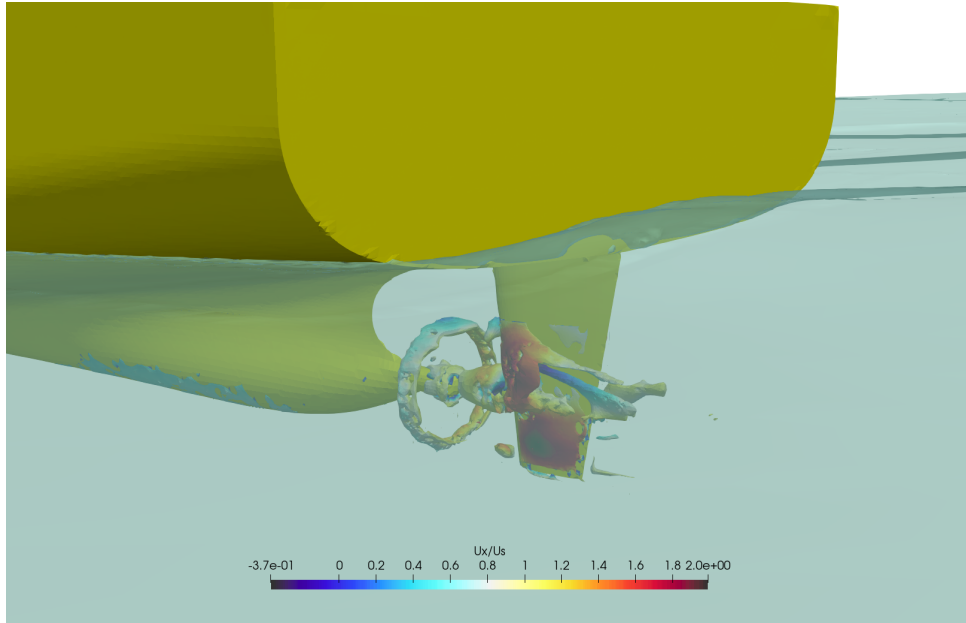
Figure 44: Mean value of thrust and torque coefficients

For the mean thrust coefficient  $\overline{K_T}$  (left), both numerical models and experimental measurements exhibit values consistently above the calm water baseline (red dashed line at approximately 0.27). The CSM model maintains relatively stable mean thrust values between 0.30-0.32 across all wavelengths, showing minimal wavelength dependency. The AD model exhibits similar behaviour with slightly lower values ranging from 0.29-0.30.

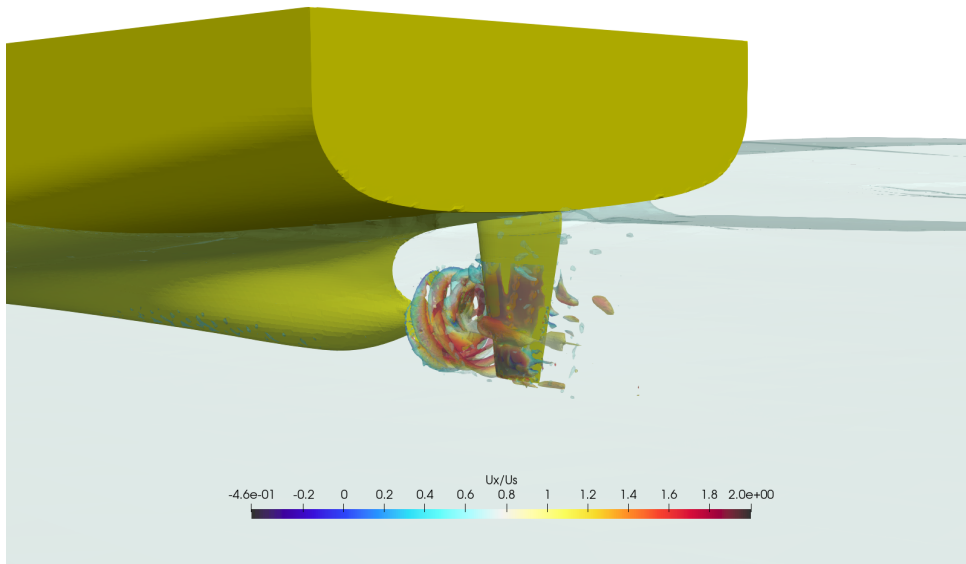
In contrast, experimental measurements show a progressive increase with wavelength, starting near 0.27 at  $\lambda_e/L_{PP} = 0.19$  and reaching approximately 0.35 at  $\lambda_e/L_{PP} = 0.45$ . The mean torque coefficient  $\overline{K_Q}$  (right) demonstrates more pronounced variations, particularly in the experiments. All methods show values substantially above the calm water reference (red dashed line at approximately 0.032). Both numerical models (CSM and AD) exhibit relatively constant torque levels across wavelengths, ranging between 0.045-0.048. However, experimental measurements display a strong wavelength dependency, increasing from approximately 0.044 at the shortest wavelength to 0.055 at  $\lambda_e/L_{PP} = 0.46$ , representing a 25% increase compared to the numerical predictions at the longest wavelength.

The increasing discrepancy between experimental and numerical results at longer wavelengths is particularly evident in the torque measurements. It should be noted that the numerical simulations maintain constant ship speed throughout the wave encounter, while in experimental conditions the ship model naturally experiences speed loss due to wave-induced added resistance which partially contributes to the observed differences

in propeller loading characteristics. Apart from the statistical analysis, differences in these numerical models are clearly visible in the computed velocity fields. Contour of the Q-criterion value for both models where the color scale represents a ratio between longitudinal flow velocity and ship speed is given in Figure 45.



(a) AD

Figure 45: Q-criterion iso-surface at  $Q = 250s^{-2}$ 

(a) CSM

The Q-criterion iso-surface shows that the AD model produces a simplified, axisymmetric wake structure with uniform vortex distribution, while the CSM model captures complex three-dimensional vortical patterns including discrete blade tip vortices and helical wake

structures. The velocity field ( $U_x/U_s$ ) show corresponding differences, where the AD model generates uniform flow acceleration across the propeller disk compared to the highly non-uniform, blade-resolved velocity distribution exhibited by the CSM model.

Furthermore, in the torque signals from both fully discretized propeller model and experiment there is an evident peak that corresponds to the propeller revolution rate frequency, Figure 47. This confirms that the propeller modelling with discrete blade geometry is far more superior and physically accurate than averaged actuator disk models.

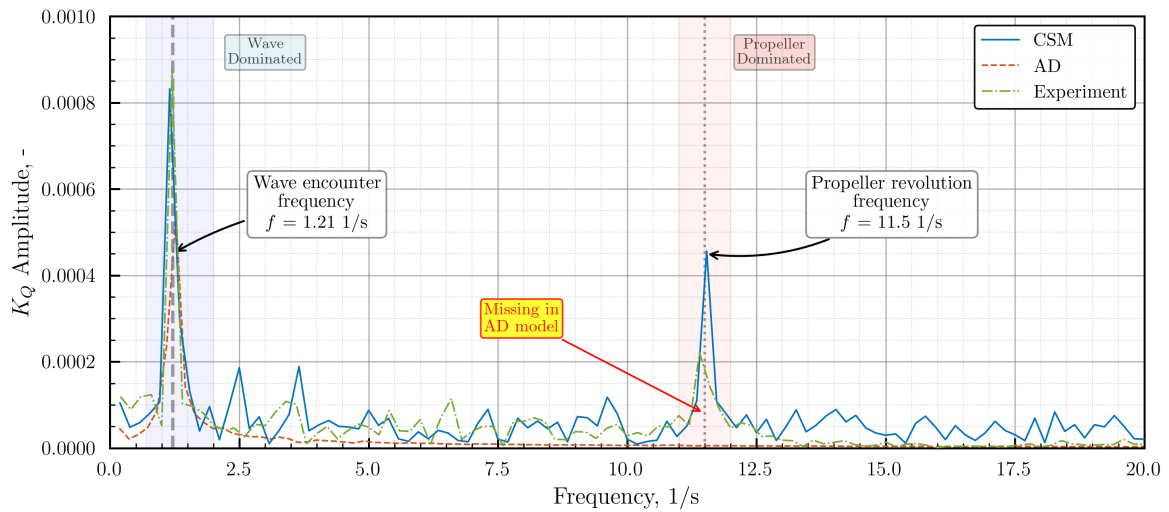
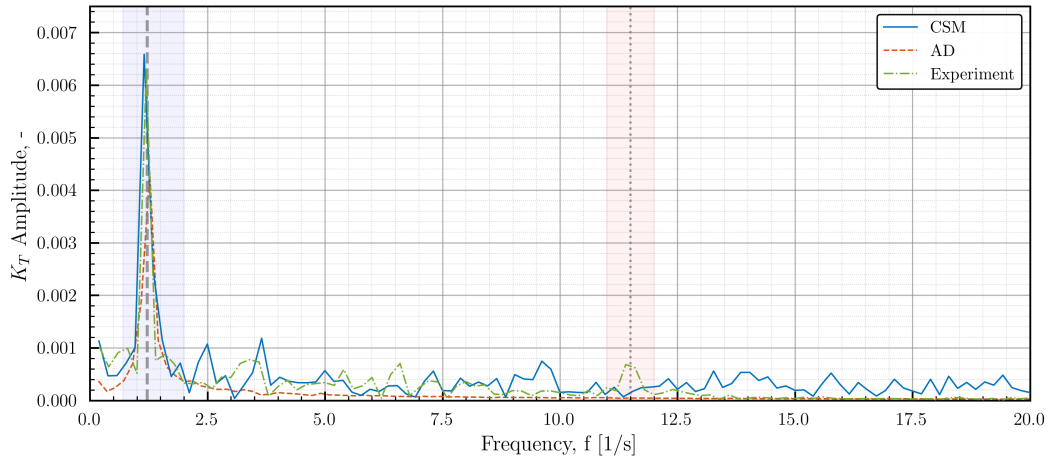


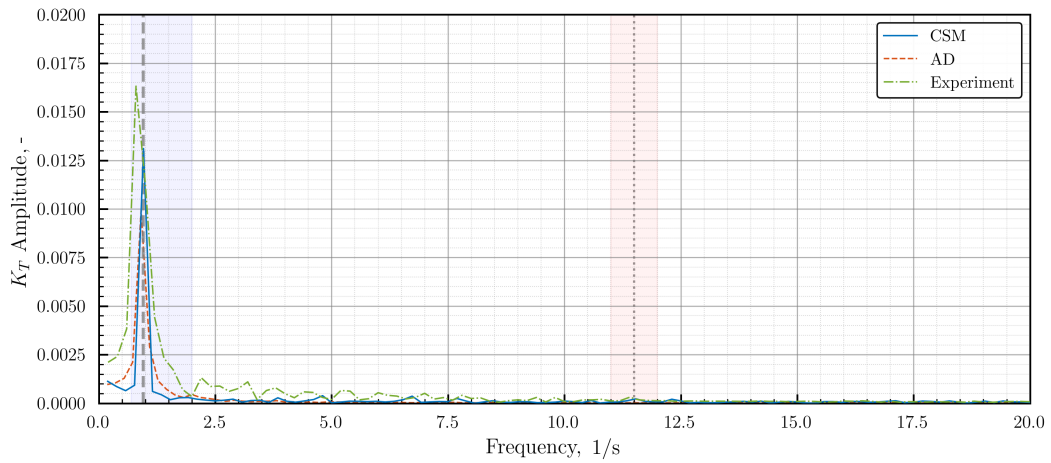
Figure 47: Frequency content of the torque signal for the first wave case

The full scope of numerical and experimental signals indicating wave and propeller frequency are given in Figure 48 for thrust and in 49 for torque, across all three wave cases. Interestingly, the propeller rate frequency is much more pronounced in torque signals opposing to thrust.

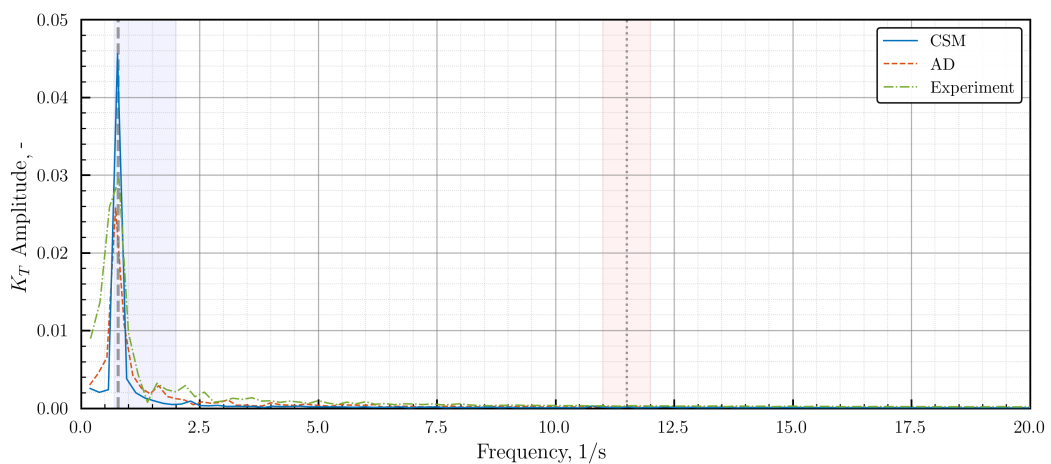
This might be addressed to circumferential variations in the flow field and local blade loading distributions. The presence of high-frequency content within the CSM model might have implications in the evaluation of structural integrity, although for such assessment, a comprehensive and complex fluid-structure interface would be necessary in order to determine these cyclic loads.



(a) Thrust frequency content from AD, CSM and experiments for the first wave case

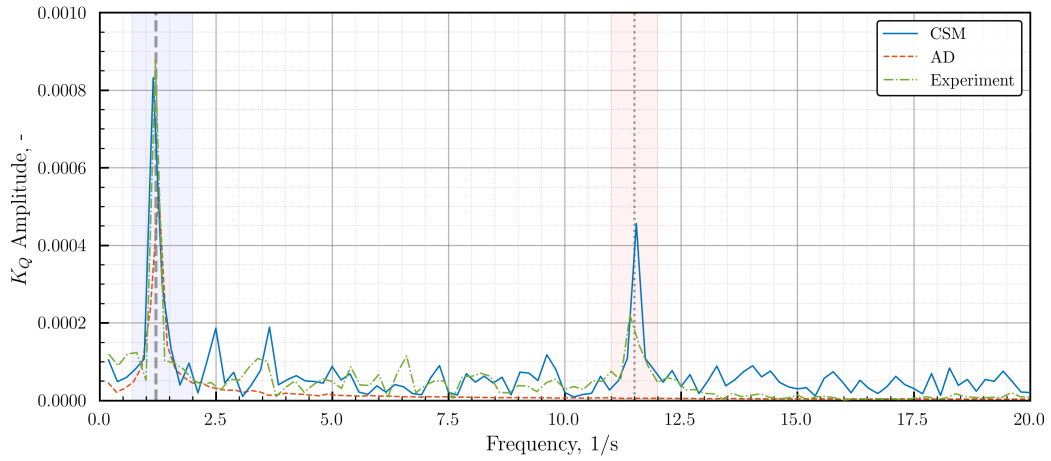


(b) Thrust frequency content from AD, CSM and experiments for the second wave case

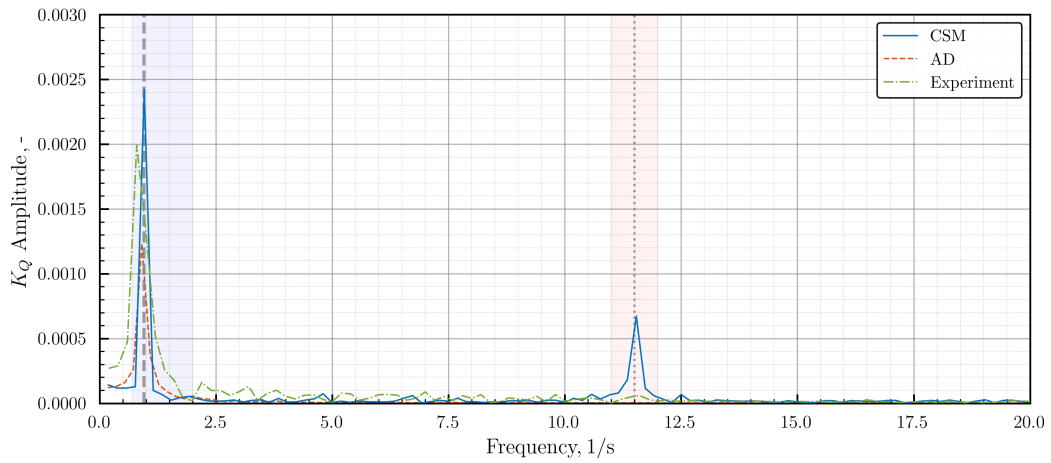


(c) Thrust frequency content from AD, CSM and experiments for the third wave case

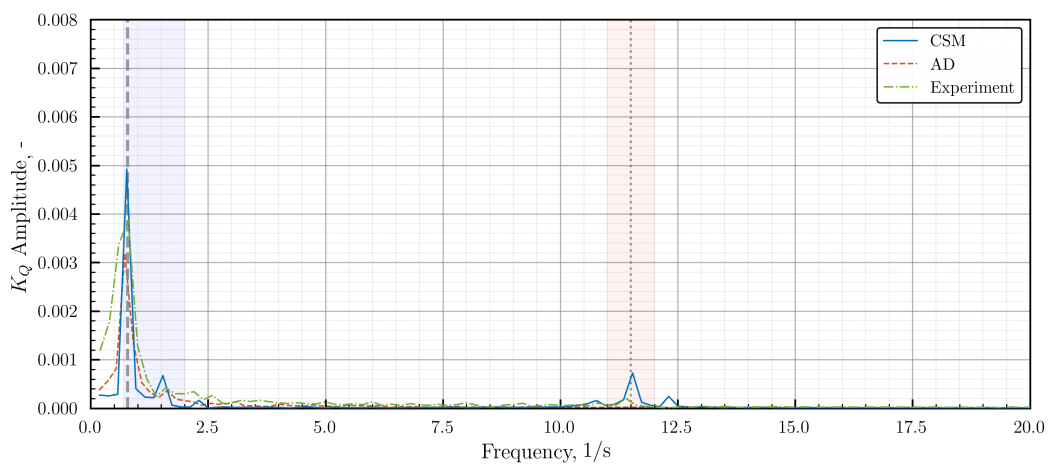
Figure 48: Comparison of thrust frequency content from AD, CSM, and experiments for three wave cases



(a) Torque frequency content from AD, CSM and experiments for the first wave case



(b) Torque frequency content from AD, CSM and experiments for the second wave case



(c) Torque frequency content from AD, CSM and experiments for the third wave case.

Figure 49: Comparison of torque frequency content from AD, CSM, and experiments for three wave cases

Beyond the isolated propeller performance characteristics, next paragraph deals with comprehensive hull-propeller interactions that are quantified classically via propulsive coefficients.

### 6.4 Propulsive Coefficients in Waves

Wholesome assessment of propulsion characteristics in waves requires additional insights into hull-propeller interactions. Thus, this subchapter presents a quantification of propulsive efficiency in waves from both numerical methods. The methodology of calculating propulsive coefficients is thoroughly explained in Chapter 4. The results of the open water efficiency  $\eta_0$  and hull efficiency  $\eta_H$  in dependence of the encounter wavelength are plotted in Figure 50.

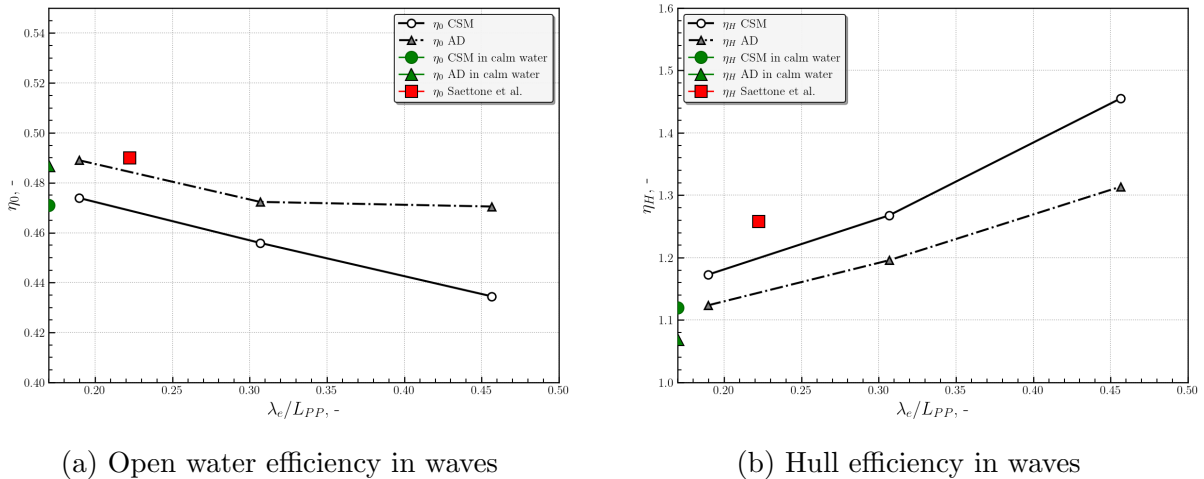


Figure 50: Open water and hull efficiency from CSM and AD models

The absolute difference between open water efficiency values in calm water result from the minimal discrepancy in calm water performance of these methods, as seen in Table 12. For the encounter wavelengths in the range of 20-30% of  $L_{PP}$  decline of the open water efficiency is seen for both numerical models.

This is a direct impact of the increased thrust in waves. For the case of the longest encounter wave, AD seems to exhibit a minor change than the fully discretized propeller model. For clarity, thrust deduction fraction and effective wake fraction are shown separately in Figure 51.

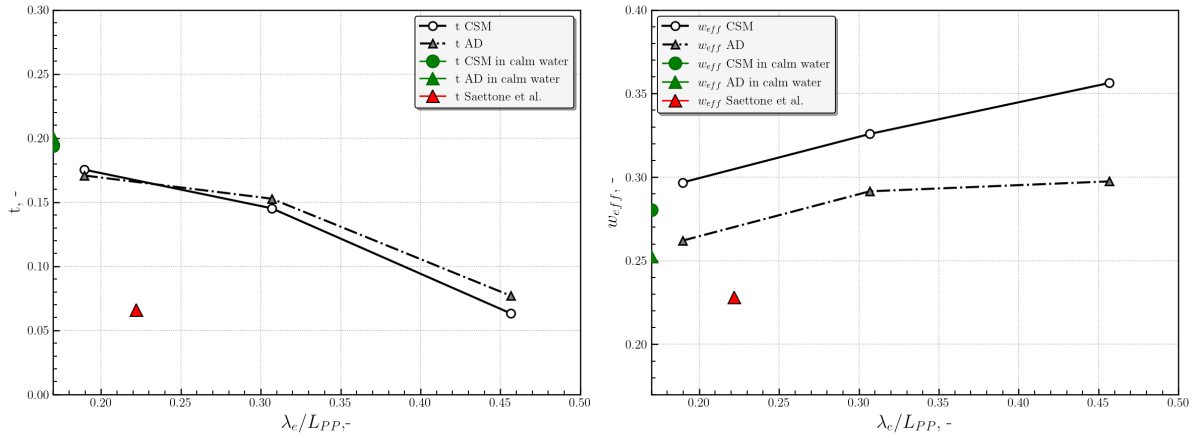


Figure 51: Thrust deduction fraction and effective wake fraction from AD and CSM

The computed thrust deduction fraction for both CSM and AD method shows similar behaviour with respect to wavelength. For comparison purposes, experimental thrust deduction fraction for the same ship model at  $\lambda = 0.46$  m is shown from (Saettone et al., 2021). Observing the computed results for CSM and AD, both methods exhibit similar effects on the thrust deduction fraction while the effective wake fraction computed from AD shows negligible difference for longer wavelengths.

This might be characterized as an inherent limitation of the AD method in higher sea states, where the disturbed flow velocities due to waves and ship motions are not properly taken into account. In order to ease the understanding in calculation of the thrust deduction fraction, time domain signals of overall resistance with a running propeller  $\overline{R_{T_{AP}}}$  and towed hull resistance  $\overline{R_{T_{towed}}}$  are shown in Figure 52 for CSM and for AD in 53.

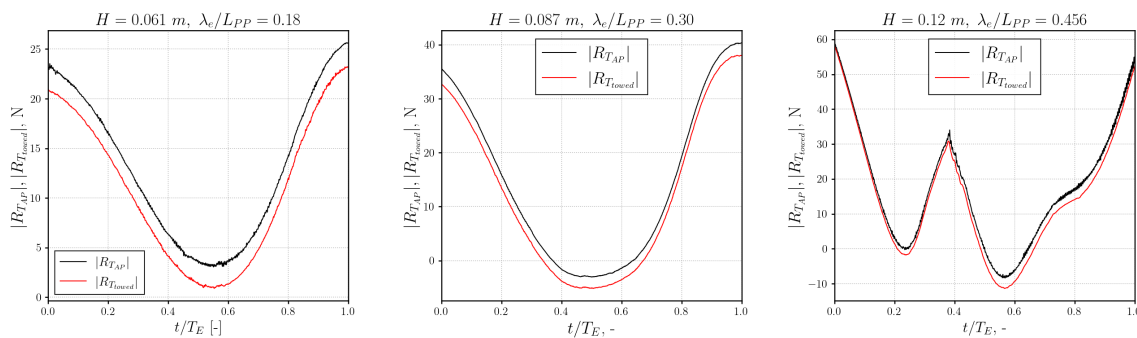


Figure 52: Comparison of propeller-induced component in the total resistance in one encounter period by CSM

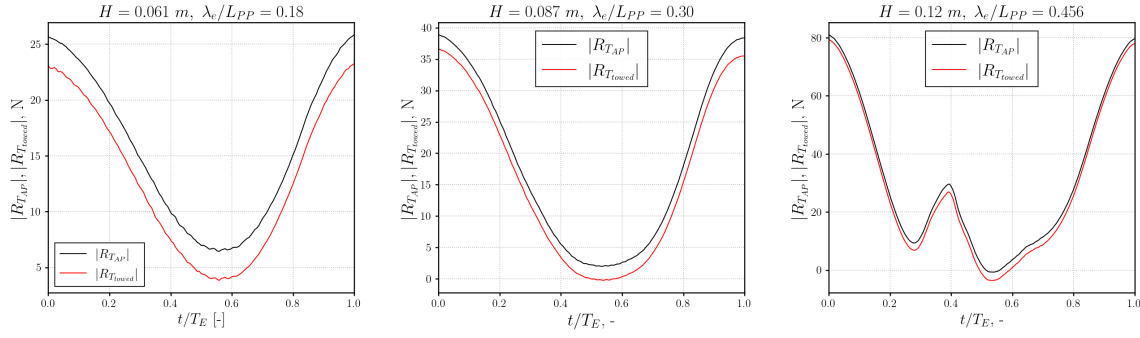


Figure 53: Comparison of propeller-induced component in the total resistance in one encounter period by AD

The relative rotative efficiency  $\eta_R$  along with overall quasi-propulsive efficiency  $\eta_D$  is given in Figure 54.

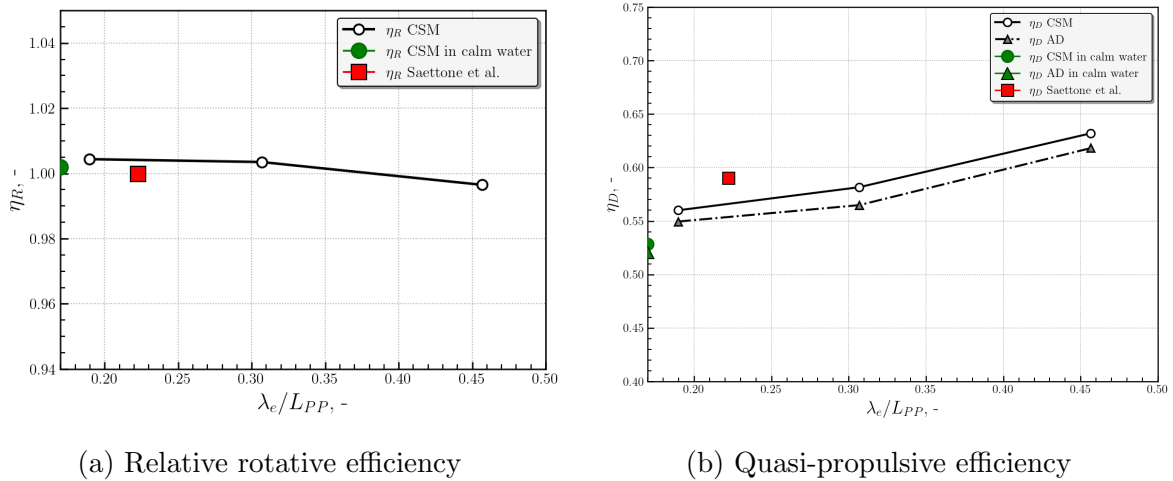


Figure 54: Relative rotative and quasi-propulsive efficiency obtained with CSM and AD models

The relative rotative efficiency shows negligible change with respect to wavelength. Similar findings are reported in (Saettone et al., 2021). The overall propulsive efficiency  $\eta_D$  exhibit similar trend for both propulsion models. The main contributor in the sudden jump of propulsive efficiency is the low thrust deduction fraction and high effective wake fraction. Generally low value of thrust deduction fraction at approximately  $\lambda_e/L_{PP} = 0.46$  reveals that the propeller-induced contribution in the total resistance is much lower than the wave-induced component. In the next chapter, computed results are thoroughly discussed, compared to existing literature and followed by conclusions.

## 7 DISCUSSION OF THE RESULTS

This chapter presents a comprehensive discussion of the numerical results obtained from both full-scale and model-scale simulations. The discussion is structured to critically evaluate the performance of the AD and CSM models across different operating conditions, from calm water to various wave environments. Particular attention is given to the strengths and limitations of each modeling approach, providing an objective assessment of their predictive capabilities.

The results are analyzed in the context of available experimental data, acknowledging the inherent differences in test conditions and scale effects that influence direct comparisons. By examining both scales separately and then comparing them, this discussion aims to establish a clear understanding of how numerical predictions relate to physical reality and where further improvements in modeling methodology are needed. The insights gained from this analysis contribute to better understanding of ship propulsion behaviour in realistic sea conditions and guide further research directions.

### 7.1 Discussion of the Results in Full Scale

A significant amount of full scale simulations with AD at a very specific scale including both calm water and waves, have been performed. Observing the computed results of the sea trials, the AD model is showing excellent agreement with measured values. The key factor in the AD model is the corrective term, which proved to be an elegant and robust solution, as it is shown by previous authors (Vukčević et al., 2017a; Bakica et al., 2019). The self-propulsion balance (thrust=resistance) is thus successfully achieved. However, it is important to stress that the viscous component of the resistance requires careful treatment at this scale.

For the Post-panamax ship, the viscous component consists of approximately 53% of the total resistance. It was found that the calculated viscous force differ significantly with even a slight change in certain geometrical parameter of the boundary layer, especially the thickness of the first adjacent cell. This is to be expected, since the micro-scale effects of hull roughness are modelled using an approximate wall function and applied to the macro-scale of a full-scale containership. However, the resource-saving characteristic of the wall functions makes them a first choice for this kind of applications, which is especially

valid for industrial cases. Moving towards wave modelling, a significant challenge is the mesh resolution requirements in the free surface area for satisfying wave propagation for the representative sea state studies at this scale. Given the size of the ship compared with the targeted  $H_{1/3}$ , it is clear that the mesh spatial resolution in the vicinity of the free surface area needs to be remarkably high.

Therefore, in order to prevent a very high cell count in this region, a wave propagation study is conducted in order to determine wave amplitudes and periods that match the desired characteristics of wave spectrum. An iterative procedure is carried out in which the amplitudes and periods are adjusted according to the acceptable deviation from the theoretical spectrum. This proved practical as the two-dimensional numerical simulations were sufficiently fast to enable iterations with multiple inputs on a daily basis. As indicated in subchapter 5.4.1, the insufficient number of computational cells in the longitudinal direction was detrimental to a more accurate match of wave periods and consequently, wavelengths. However, as the computed zero-crossing period is within the range of RSS, as seen in Figure 22, this discrepancy did not substantially contaminate the results.

After appropriately identifying the wave amplitudes and periods, calm water simulations with and without the AD for a loading condition that resembled the chosen data segment are performed. For this loading condition, the computed calm water resistance with AD model of 2725 kN shows slightly imbalanced self-propulsion state as seen in Table 9 where the produced thrust is approximately 2.8% lower. Persisting on the almost perfect match between these two values would require a slightly higher propeller revolution rate. Given the approximately quadratic relationship between thrust and revolution rate from Eq. (38) around the operating point, only a minimal increase in propeller RPM (around 1.4%) would be required to overcome this 2.8% thrust deficit. Therefore, this minimal shift of the self-propulsion state is neglected. The calculated propulsion coefficients for the calm water regime are well in line with empirical formulas for single-screw merchant ships given by (Molland et al., 2011).

A marginally lower thrust deduction (0.138) and wake fraction (0.208) from the empirical data might indicate an optimized hull form and a highly efficient propeller design. While the propeller itself is equipped with a Propeller Boss Cap Fins (PBCF) as an ESD, the actuator disk methodology cannot accurately capture the hydrodynamic effects of such devices. Although the PBCF geometry was included in the open water

simulations, the RANS-based computational approach cannot reliably verify whether hub vortex energy recovery was achieved. Although the quasi-propulsive efficiency value of 0.73 exceeds traditionally reported ranges, it should be noted that these empirical benchmarks are largely based on older ship designs. The observed higher efficiencies likely reflect advancements in hull form optimization and propeller design incorporated in modern Post-Panamax containerships. Also, excluding mechanical losses ( $\eta_s$ ) contributes to a minimal increase of the quasi-propulsive efficiency. Furthermore, the actuator disk model, by its reliance on open water curves, could not capture accurately enough rotative effects of the flow, thereby effectively setting the relative rotative efficiency  $\eta_R$  to unity, thus limiting this simplified propulsion modelling approach.

The RSS simulations were conducted after performing calm water simulations. While the (ITTC, 2017b) recommends minimum full scale test durations of 20 to 30 min in irregular wave tests, in this thesis CFD simulation in RSS are limited to six minutes of real time to comply with computational constraints. This is justifiable for the relatively mild short duration sea state considered ( $H_{1/3} = 1.315$  m), where wave-induced ship motions were relatively low and wave-induced nonlinearities occurred less frequently compared to those in severe sea states. These RSS simulations captured the ship's traveled distance of more than two nautical miles with about 45 to 60 wave encounters across all dominant wave periods, thereby providing sufficient data for a statistical analysis under these relatively moderate conditions.

Particularly valuable is the opportunity to systematically compare CFD-based predictions with high-quality onboard measurements, which were challenging to collect, both from the practical standpoint in selecting and mounting the appropriate instruments and from the proprietary nature of the data itself. Figure 55 presents delivered power spectral densities obtained from measurements as well as from filtered and unfiltered CFD computations. The high frequency oscillations indicate that the unfiltered CFD solutions captured wave-induced changes in propulsion output. However, the Savitzky-Golay smoothing filter was applied to the delivered power prediction to omit high-frequency wave-induced oscillations for consistent comparison with the measured data, which are inherently filtered by the propulsion system's measuring properties. Applying the filter caused two prominent peaks to appear in the power spectrum:

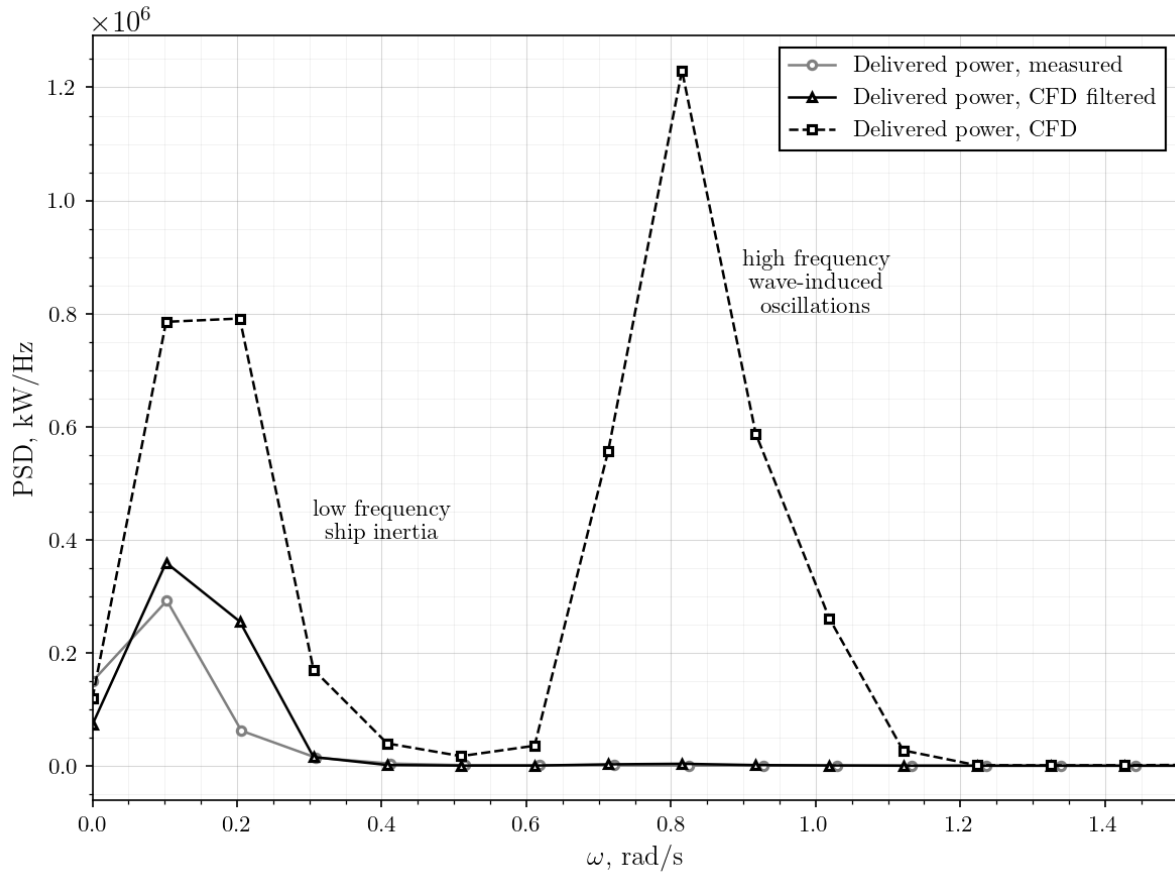
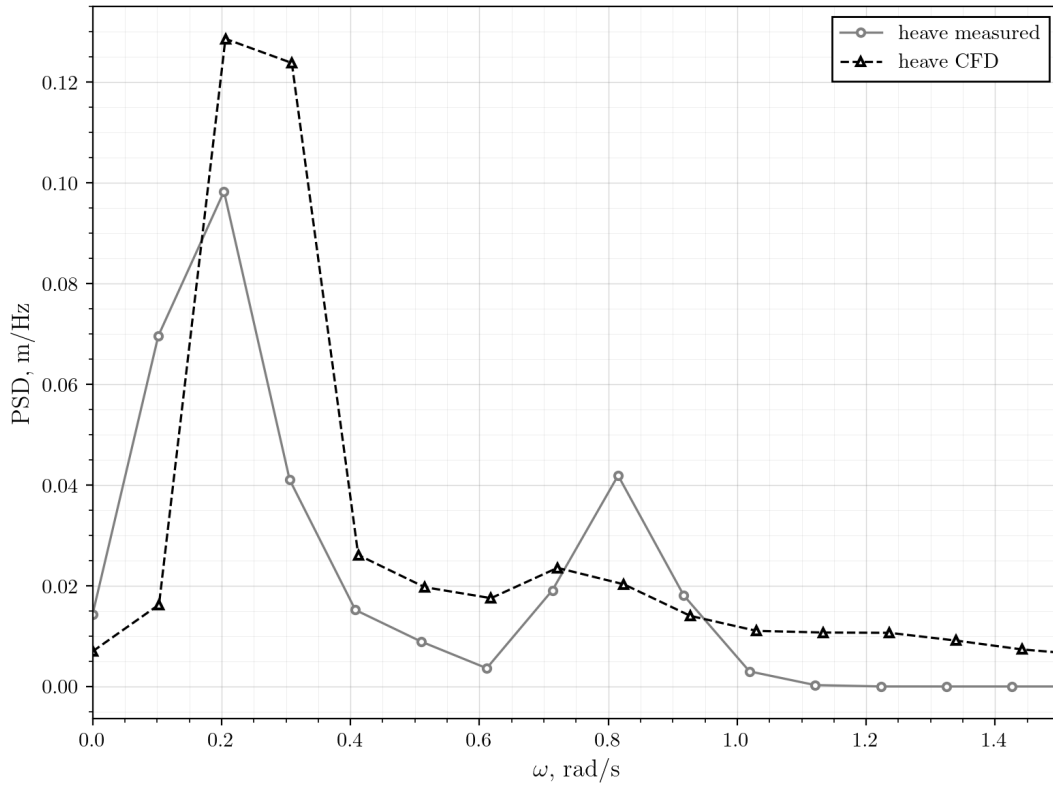


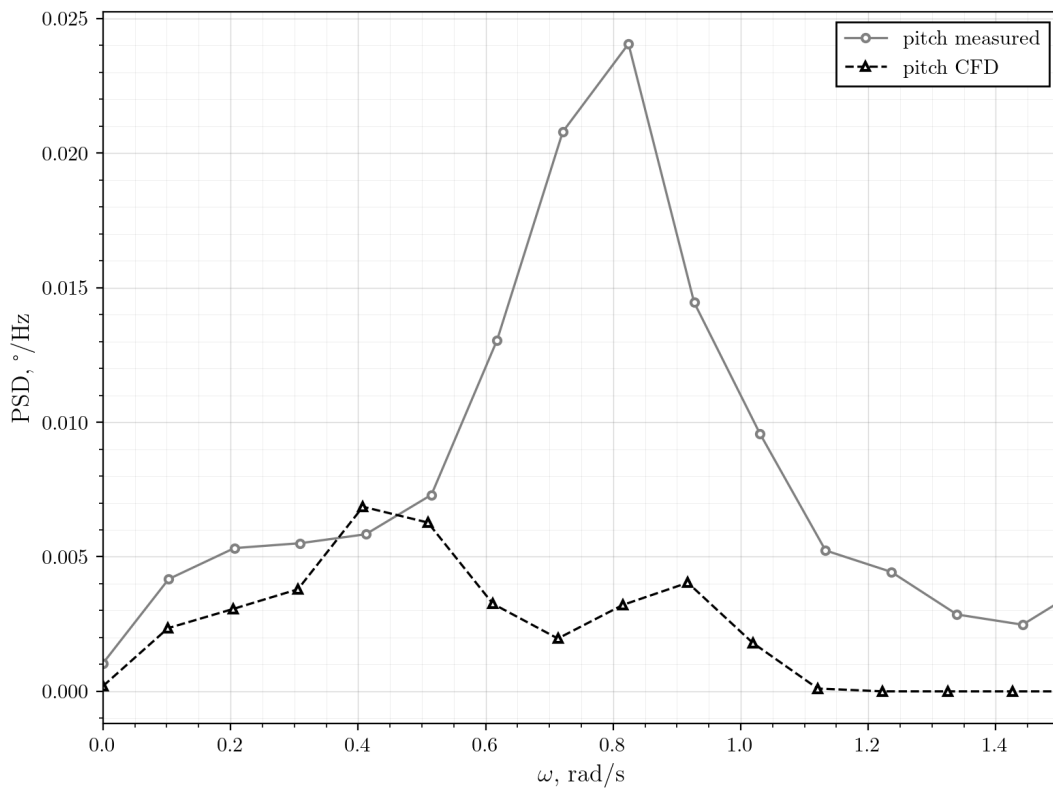
Figure 55: Power density spectrum of the delivered power

Interestingly, the spectrum’s low frequency peak occurs around 0.1 rad/s for both measurements and CFD model. It is, however, challenging to assess what is exactly causing the low frequency response. As in indicated in (Pinkster, 1980), second-order low frequency components are associated with the frequencies of wave groups traveling in irregular waves. The second peak at 0.8 rad/s, corresponding to the sea state’s zero-crossing wave period of 7.85 s, well in line with calculation in subchapter 5.4.1.

This led to conclusion that, in mild sea states, the AD model captures both low and high frequency responses of ship dynamics in the propulsion output. However, the level of accuracy in severe sea state, which is difficult to assess, would likely deteriorate due to the simplified approach of the AD model and the increasingly nonlinear interactions of propulsion characteristics. Figure 56a and 56b presents the transformed seakeeping signals of heave and pitch into the frequency domain in the same manner as the signals of delivered power.



(a) Heave spectrum



(b) Pitch spectrum

Figure 56: Power density spectrum of ship motions

Both the numerical CFD method as well as the onboard measurements captured the heave spectrum's peak of low frequency heave oscillations. The peak of the heave response was slightly overpredicted, whereas the peak of the pitch spectrum corresponded to the modal wave period of the RSS. The difference of computed and measured pitch is also as listed in Table 8. Higher variability characterized the computed pitch response, whereas the amplitudes range is well in line with measurements. The variability and amplitude range of computed heave response is also in accordance with measurements. Differences between mean values of pitch and heave (Table 8) and measurements was due to the ship's dynamic trim and sinkage, which were particularly difficult to predict. This was attributable to their small absolute values and the possible deviations of the longitudinal position of the ship's center of gravity and mass moment of inertia  $I_{55}$ , interpolated from the stability booklet.

Finally, obtained valuable insight into propulsion coefficients in representative sea states is obtained. The quasi-propulsive efficiency  $\eta_D$  remained highly competitive at 0.678. As presented in Table 9, the most significant change was in the wake fraction. This was attributable to pitch and heave motions, which significantly altered the flow field. Thrust deduction fraction also deteriorated slightly, for which the increased thrust requirement in waves contributed most. Hull efficiency in waves remained nearly constant. Findings related to propulsion coefficients were well in line with a similar study of (Sigmund and el Moctar, 2017). The principal limitation of AD model when applied to assess propulsion coefficients was the inability to predict the propeller's relative rotative efficiency  $\eta_R$ . The fully discretized propeller geometry would have been needed to produce meaningful results on this matter, which leaves space open for further research. For such methods, either significant computational resources or completely different conceptual development of the AD based model are required.

Investigation of the full-scale ship's propulsion coefficients under RSS conditions yielded a degradation of propulsion efficiency of only about 7% under representative conditions. This implies that it may be appropriate to consider reducing the traditional 15% sea margin when revisiting sea margin guidelines. Of course, several other factors, such as regular dry-docking, uncertainties of weather routing procedures, reduced contractual speeds (slow steaming), etc., must also be diligently considered.

Furthermore, a second limitation in this study is that the ship's surge motion is not

modelled. Surge amplitudes may have significantly influenced the flow field in the vicinity of the AD and the propeller's produced thrust and torque. However, to accurately model surge motion in propulsion simulations, the paradigm of ship resistance being equal to ship thrust need to be satisfied. Their inherent imbalance would have caused the ship to periodically accelerate and decelerate, and surge modelling should have been a priority only if the speed-loss related phenomena were of interest.

Also, modelling ship motions with grid deformation could have resulted in significant non-orthogonalities of control volumes due to surge-induced grid stretching and compression. Although this issue might have been bypassed using overset grids, a new set of numerical uncertainties as well as a significant increase in computational power would have been introduced. Here, neither involuntary nor voluntary speed loss was recorded in the chosen data segment and, therefore, surge was not considered. By acknowledging these two main constraints of this study, simplified propeller model and omitted surge modelling, a clear framework to enhance further understanding and research direction is pinpointed.

## 7.2 Discussion of the Results in Model Scale

This chapter is dedicated to discussion of the computed results for self-propulsion test in waves using different propeller models. Self-propulsion simulations in calm water show excellent agreement with experimental values of thrust and torque which indicated that even the computations on coarse grids can yield physically relevant results. The thrust from the CSM model deviates approximately 5.6% while the AD yields an underprediction by an almost negligible margin of 1.5%. Results on finer grids showed even better agreement with experimental values, however, the results from the coarse grids indicated that the coarse grid topology and the overall numerical model can be translated to complex propulsion simulations in waves.

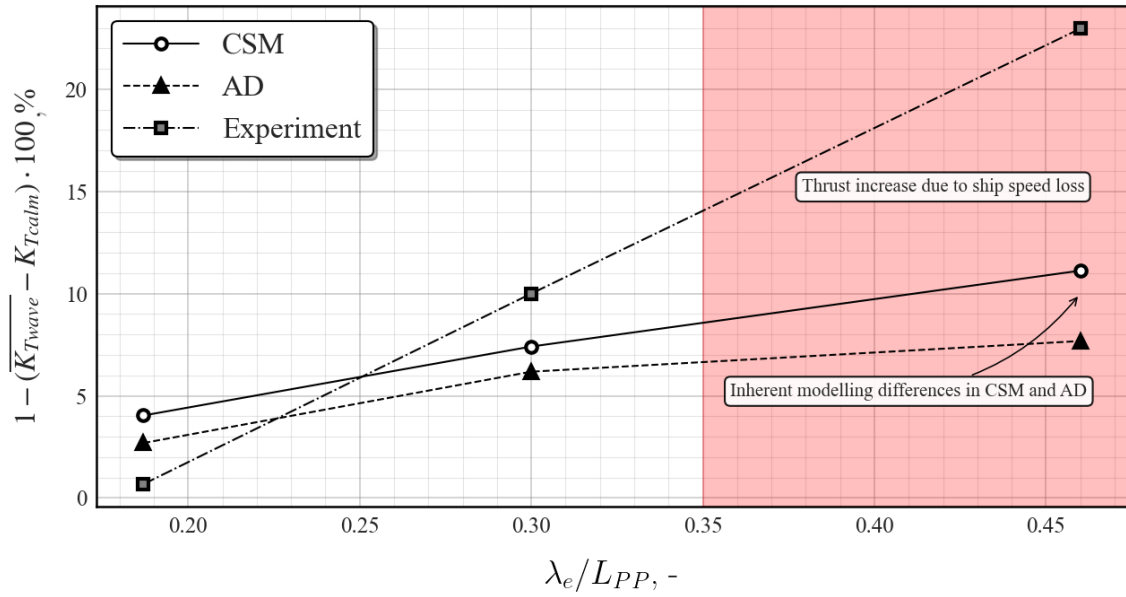
Before propulsion tests in waves, a simplified numerical assessment of the wave propagation was done in order to identify necessary cell number in the free surface area. This assessment proved vital for the methodology on using a single grid size for multiple wave heights which enormously saved computational time. The necessary cell numbers in vertical and longitudinal directions with respect to wave height and wavelength are given in subchapter 6.3.1. Furthermore, pitch and heave response of the DTC model showed favorable agreement with experiment, both obtained by CSM and AD model.

The biggest discrepancy can be seen in the heave response for the second case where  $H/L_{PP} = 0.015$ . On both grids the heave motion is underpredicted, while the grid with the AD model show a slight deviation.

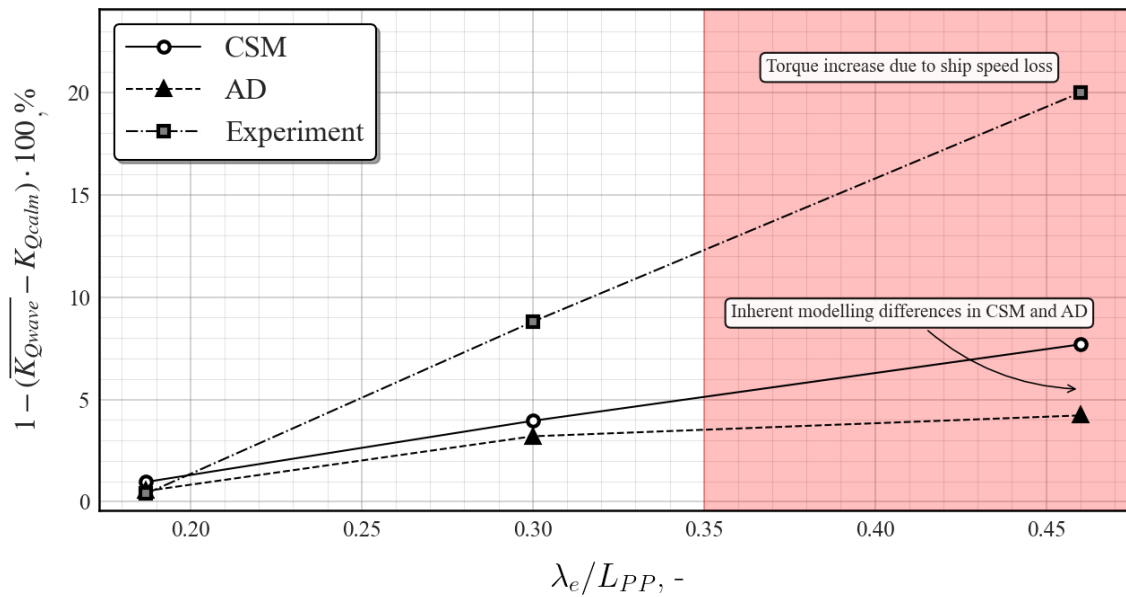
This can attributed to the grid density in the stern region of the model which slightly differs from the CSM model. Nevertheless, as shown further in the text, this did not have any significant influence in self-propulsion test. For the self-propulsion results, DFT analysis is conducted on the thrust and torque signals from the CSM and AD models. As expected, the dominant frequency is equivalent with encounter frequency as indicated in the plots. The statistical analysis of the signals shows that the CSM model has a somewhat better prediction of the mean amplitude and mean value. For the encounter wavelength close to the  $0.45L_{PP}$ , mean value of thrust and torque obtained by both propeller models deviate from the experiment. This might be attributed to the natural involuntary speed loss occurring in the free running experiment, where the inflow speeds at the propeller are significantly lower compared to calm water condition, thus amplifying thrust and torque.

The change of mean value of thrust and torque with respect to it's corresponding value from calm water is given in Figures 57a and 57b where similar trend of both AD and CSM model is seen up to approximately  $0.3L_{PP}$ , while for the wavelength close to the half-length of the ship the CSM model shows stronger increase in both thrust and torque. In other words, modelling surge, as indicated in subchapter 7.1, seem to be crucial for accurate modelling of propulsion characteristics in high sea states. The significant increases in thrust and torque observed in the experiment stem from the natural, involuntary speed loss that occurs at high sea states.

This implies that, for accurate numerical modelling of propulsion behaviour in higher sea states, two aspects need to be addressed. Firstly, a numerical propulsion model of sufficient fidelity must be adopted in the assessment. This points toward the use of fully discretized propeller models, which inevitably require significantly higher computational time than simplified propeller models. Secondly, the involuntary speed loss resulting from added resistance needs to be properly modelled. As stated earlier, this can be achieved using an overset grid topology.



(a) Thrust increase from the simulations and experiments



(b) Torque increase from the simulations and experiments

Figure 57: Comparison of thrust and torque increases from simulations and experiments

The observed differences in thrust and torque increase for  $\lambda_e / L_{PP} = 0.46$  might be characterized as the main limitation of this work, but represent an excellent avenue for future development of propulsion CFD models. The relative difference between CSM and AD model for the longest wave can be attributed to inherent limitation of the actuator disk model, in which the disturbed inflow on the propeller plane is averaged over the disk.

With such approach, thrust and torque increase seem to be underpredicted. However, it is important to stress that this discrepancy occurs at a wavelength that is approximately half of the ship length which, for this specific case, is very unlikely that the ship in full scale will navigate.

Regarding the propulsion coefficients in waves, open water propeller efficiency  $\eta_0$ , both CSM and AD propulsion model show similar trend while for the longest wavelength the fully discretized propeller seems to decline more rapidly. Since  $\eta_0$  is calculated using the thrust identity method, the CSM model appears to better capture the mean thrust increase in waves. The open water propeller efficiency is thus directly proportional to the values of mean thrust given in Figure 44 where the values from CSM model are closer to the experimental measurements compared to the AD model. Regarding the thrust deduction fraction, it is reasonable to assume that the major discrepancy between experimental and numerical results stem from the different setups in the approaches.

In the experimental setup in (Saettone et al., 2021), the DTC model is allowed for surge motion which can have profound effects on the results. Furthermore, the wave steepness of 0.103 is higher from the case in (Saettone et al., 2021), while in the free running experiments it is set to 0.0785 for each case. The trend of significantly lower thrust deduction fraction in waves is also reported in (Irannezhad et al., 2024). Jeong et al. (2025) reported the decrease of both thrust deduction fraction and wake fraction in waves in model scale. Furthermore, the relatively high thrust deduction fraction in calm water is also reported in some studies for the DTC model at lower Froude numbers (Kinaci et al., 2018), opposed to the experimental value of 0.09 from (el Moctar et al., 2012). The effective wake fraction, also based on the thrust identity method, show similar trend as thrust deduction fraction. It is reasonable to assume, although difficult to validate, that in higher sea states AD cannot properly capture disturbed flow velocities. The relative rotative coefficient  $\eta_R$ , shows negligible changes in waves obtained by the CSM model compared to calm water conditions. Actuator disk model is inherently unable to calculate  $\eta_R$  since the values are directly corresponding from the open water propeller curve.

For the wake field calculations from both propeller models, the absence of experimental measurements limits the analysis to a qualitative comparison of a single representative case rather than a systematic validation study. Figure 59 presents a comparison of the effective wake fields predicted by the AD model and the CSM approach at three measurement planes

for the third wave case: upstream of the propeller located approximately at  $0.03L_{PP}$ , downstream of the propeller at  $0.015L_{PP}$  right in between Costa bulb of the rudder and propeller hub, and behind the rudder at  $-0.015L_{PP}$ . For clarity, location of the measurement planes are illustrated in Figure 58:

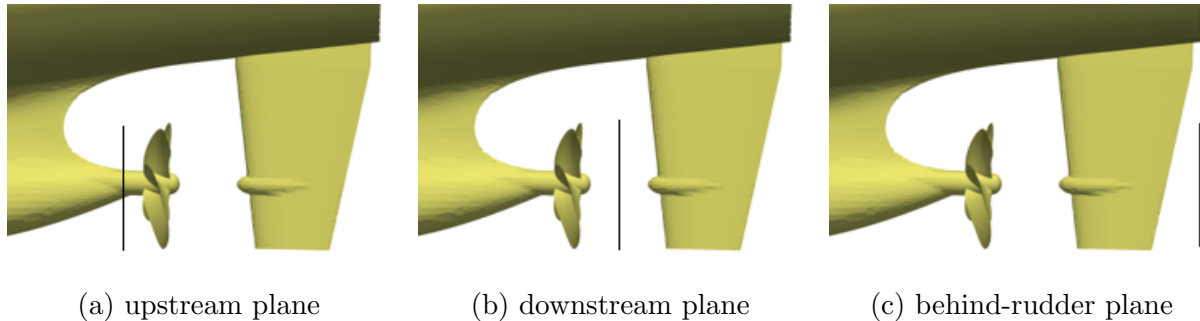


Figure 58: Location of measurement planes for wake field comparison

The measurements are taken from the third test case, for which the details are listed in Table 11. The upstream plane shows the incoming flow field, while the downstream and behind-rudder planes reveal the wake development and propeller-rudder interaction characteristics. The coloring scale resembles the normalized fluid velocity by the imposed ship speed, thus indicating the acceleration of the flow due to different propeller models. The upstream wake fields in Figures 59a and 59b show that the AD model accelerates the flow before the fluid reaches propeller plane.

This might be an indication for a different thrust deduction fraction however, the calculated values shown in Figure 51 for both waves and calm water show similar range of values. In the downstream region, Figures 59c and 59d, both the AD and CSM produce a highly symmetric flow field with concentric velocity contours around the hub. The velocity drop of the flow is more pronounced behind the AD model, ranging up to 20% lower speed than the ship speed. Behind the rudder, Figures 59e and 59f, both approaches demonstrate significant flow distortion due to the propeller-rudder interaction, but the CSM model exhibits a much larger area of accelerated flow. In general, it seems that the AD model accelerates the flow before reaching the propeller itself while the CSM does not affect the flow significantly. The downstream and behind-rudder measurement planes revealed the inherent differences from these propeller models. The acceleration of the flow is much more pronounced in the CSM model in both regions (downstream, behind-rudder). This indicates that fully resolved propeller geometry must be taken into account for accurate assessments of hull-propeller-rudder interactions.

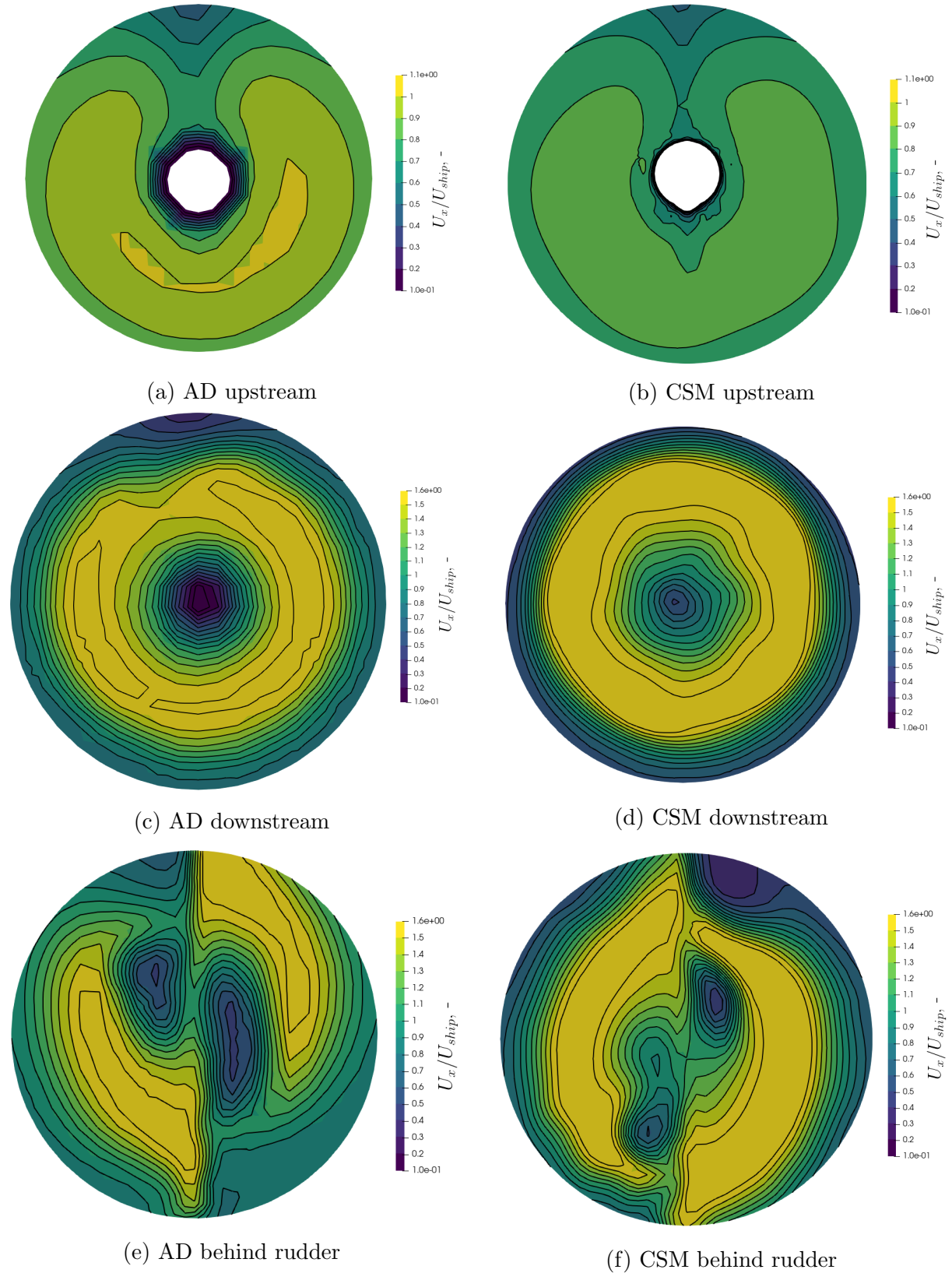


Figure 59: Comparison of effective wake fields. Upstream position is located at  $0.03L_{PP}$ , downstream at  $0.015L_{PP}$  and behind-rudder at  $-0.015L_{PP}$

### 7.3 Comparative Analysis of the Results in Full and Model Scale

In this subchapter, comparative analysis and discussion of full and model scale results are given. The similarity between ship particulars and dimensionless coefficients from full and model scale ships from the thesis are given in Table 14.

Table 14: Comparison of full and model scale ship particulars and dimensionless coefficients

Scale	$L/B$	$B/T$	$C_B$	$C_{AW}$	$C_M$	$F_r$
Full	6.8	3.65	0.69	0.86	0.983	0.189
Model	6.9	3.51	0.661	0.847	0.987	0.139
Difference %	1.5	3.9	4.2	1.5	$\approx 1$	27

The differences in hull geometries, noted in the last row of Table 14, permit comparative analysis of numerical results only to a limited extent. While both scales rigorously validate against their respective experimental datasets (onboard measurements for full scale and basin tests for model scale), direct quantitative comparison is constrained by fundamental differences in test conditions. Most critically, the wave environments differ substantially: full-scale simulations employ irregular, broad-spectrum waves (Pierson-Moskowitz,  $H_{1/3} = 1.31$  m) representative of natural seaways, whereas model-scale tests utilize monochromatic regular waves with discrete wavelengths.

This difference is not merely practical but fundamental; it is neither feasible nor physically meaningful to subject a full-scale ship to controlled regular wave conditions of sufficient amplitude and length in open ocean environment. The most notable difference between scales is the 27% higher Froude number in model tests, which simply stems from the initial targeting objectives in model-scale experiments. It is worth emphasizing that such a comparison represents a unique opportunity, as full-scale measurements in waves are exceptionally rare due to the practical difficulties and costs associated with installation and maintenance of measuring equipment on ships. The availability of both model and full-scale data for the same ship enables a more comprehensive validation than is typically possible in ship hydrodynamics research. Regarding the calm water numerical results, propulsive coefficients computed with AD across full and model scale are given in Figure 60.

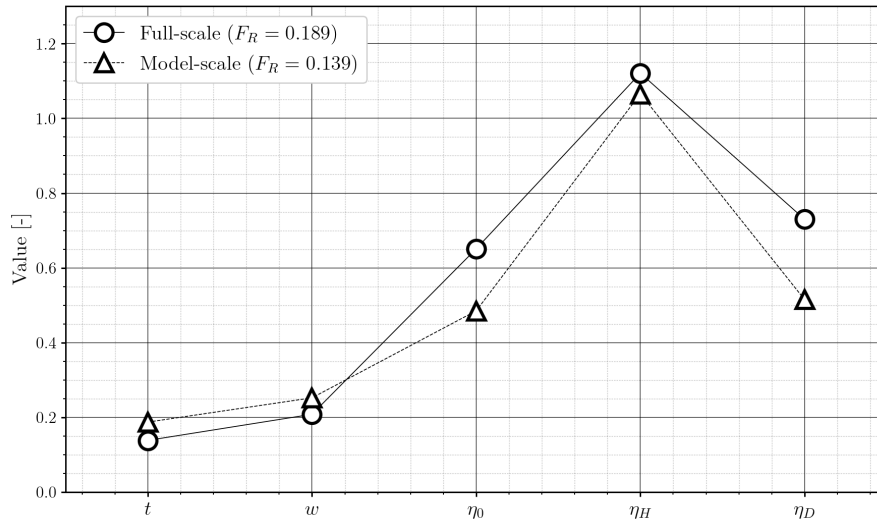


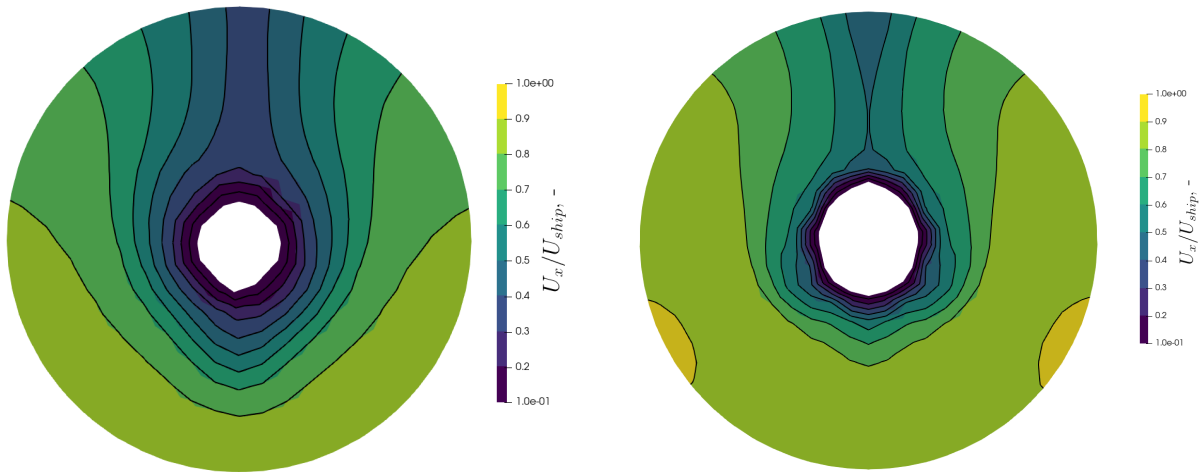
Figure 60: Propulsive coefficients across full and model scale in calm water conditions

The lower thrust deduction fraction in full scale is consistent with the literature, mainly attributed to the differences in the flow field and viscous effects. Regarding the comparative analysis in waves, different wave conditions are a limiting factor. However, in the model-scale chapter 6, the first test case resembles the wave parameters that are conducted in full-scale chapter 5. Therefore, meaningful comparison can still be given. A notable discrepancy emerged between full scale and model-scale propulsive efficiency trends in waves.

At full scale, operating in representative irregular seas, the total propulsive efficiency decreased by 7% (from 0.73 to 0.678), primarily due to increased wake fraction. Conversely, model scale simulations in regular waves showed an increase in quasi-propulsive efficiency. Several scale-dependent mechanisms likely contribute to this apparent contradiction. The most significant factor is likely the Reynolds number disparity between full-scale ( $Re \approx 10^9$ ) and model-scale ( $Re \approx 10^6$ - $10^7$ ). At model scale, the relatively thicker boundary layer may experience beneficial reorganization when subjected to wave-induced orbital velocities and pressure fluctuations. This could lead to a temporarily more uniform wake field that enhances propulsive efficiency.

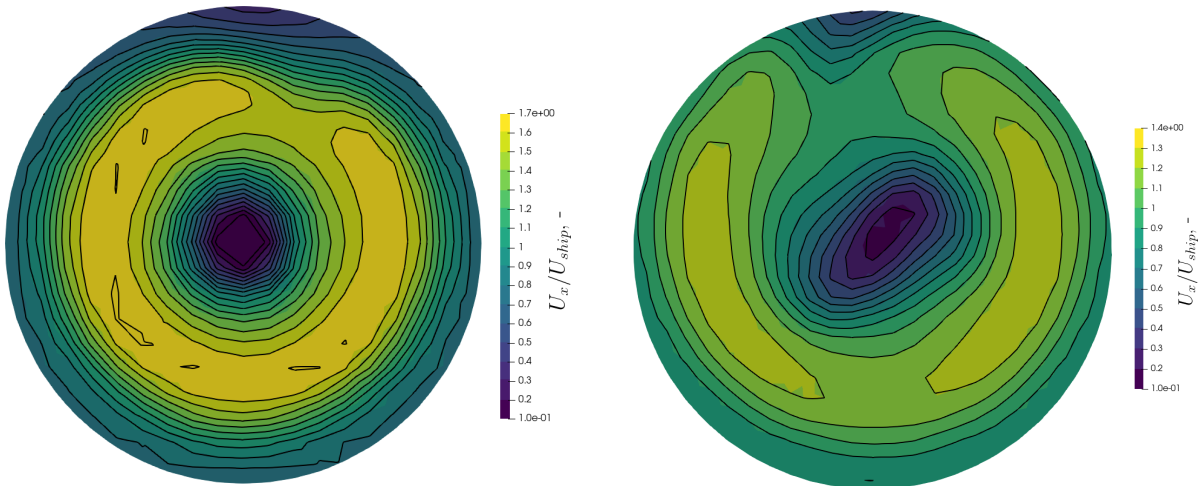
At full scale, the thinner, more developed turbulent boundary layer exhibits different response characteristics, with wave-induced pitch and heave motions creating persistent wake distortions that increase both the wake fraction and thrust deduction fraction. In model scale, the wake fraction is also showing increasing trend, opposed to the decreasing thrust deduction fraction in waves. In order to verify this statement, wake field plots are

given in Figure 61. The measurement positions are the same as in Figure 59.



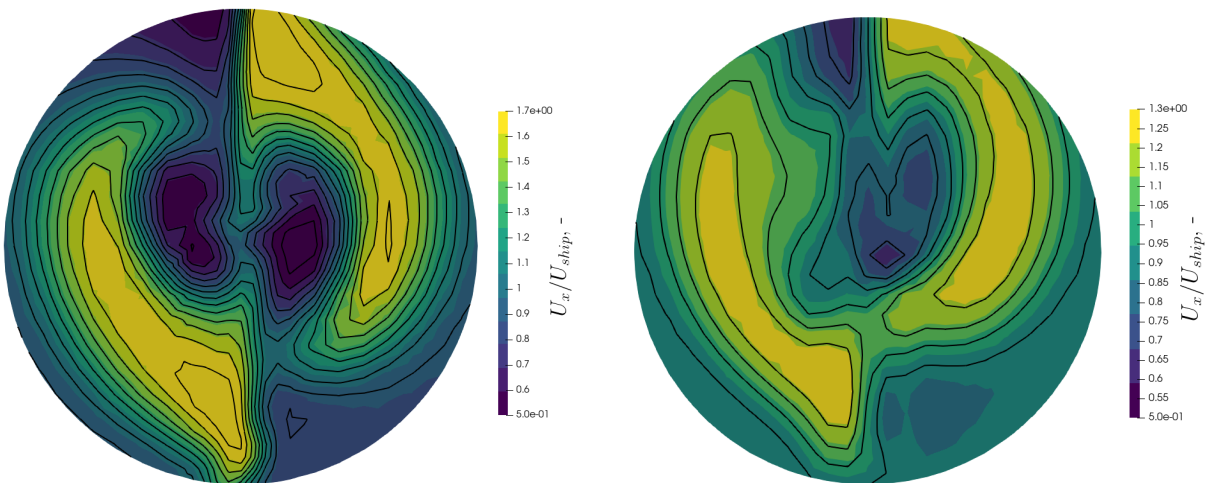
(a) AD upstream in model scale

(b) AD upstream in full scale



(c) AD downstream in model scale

(d) AD downstream in full scale



(e) AD behind rudder in model scale

(f) AD behind rudder in full scale

Figure 61: Comparison of effective wake fields from full and model-scale. Upstream position is located at  $0.03L_{PP}$ , downstream at  $0.015L_{PP}$  and behind-rudder is at  $-0.015L_{PP}$

Clearly, the deceleration of the flow is much more pronounced in the model-scale wake fields in all three measurement planes, Figure 61c, and Figure 61a and Figure 61e. Although there is a slight influence of the Froude number, the dominant factors that influence the wake field and averaged wake fraction are the Reynolds number effects, hull form geometry and propeller positioning. This has been noted first in (Benedek, 1967) and later emphasized in ITTC reports (ITTC Specialist Committee on Scaling of Wake Field, 2011; International Towing Tank Conference (ITTC), 2011). (Castro et al., 2011) and later (Vukčević et al., 2017a; Grlj et al., 2025) indicated for significantly different flow fields in model- and full-scale, specifically in the stern area.

This phenomena causes a more homogeneous inflow of the fluid towards the propeller, increasing its performance. Also, this difference in increasing propulsive efficiency in model-scale while decreasing in full-scale is even more exaggerated due to slightly different operating points of the propeller. In model-scale, the operating point is equivalent to  $J = 0.480$  while at full-scale is at  $J = 0.6$ . This insight leads to the conclusion that initial operating point of the propeller is going to have profound effects on the propulsive efficiency in waves.

## 8 CONCLUSIONS AND FUTURE WORK

The concluding chapter of this thesis is comprised of the main conclusions that this thesis has yielded and future research directions in the context of modelling ship propulsion in CFD.

### 8.1 Conclusions

This thesis developed, validated, and applied numerical methodologies for predicting ship propulsion from model to full scale in calm water and waves, with special emphasis on Actuator Disk (AD) and fully blade-resolved Coupled Sliding Mesh (CSM) propeller models. Using high-quality onboard measurements from a 14,000 TEU Post-Panamax containership and basin data for the DTC model, the work delivers the following main conclusions.

At full scale, the AD model has been shown to predict propulsion performance with notable accuracy and efficiency, provided its limitations are respected. In calm water conditions, the simulated delivered power exceeded sea trial measurements by approximately 5%, with minimal numerical uncertainty. This difference was largely attributed to aerodynamic resistance of the superstructure given in subchapter 5.3.2, which accounted for roughly 5.5% of the total resistance and explained much of the observed discrepancy.

In irregular waves, the AD captured the dominant trends and frequencies in measured delivered power, pitch, and heave, with a modest overprediction of mean power and slightly exaggerated variability. Analysis of propulsive coefficients revealed a 24.5% increase in wake fraction, a small increase in thrust deduction, and an overall reduction in quasi-propulsive efficiency of about 7%. These findings confirm that with verified open water inputs and careful wave modeling, the AD approach can reliably reproduce full-scale propulsion in realistic seas while maintaining computational efficiency.

At model scale, both the AD and blade-resolved CSM methods reproduced calm water self-propulsion results with small deviations compared to experimental data. However, in regular head waves, their differences became more pronounced. While both models accurately predicted ship motions and encounter frequency behaviour, only the CSM captured higher harmonics and blade-rate effects arising from the unsteady propeller

inflow. The AD model, due to its inherent averaging of the inflow field, tended to underpredict the amplitude of unsteady loading, particularly at long wavelengths. In terms of hull efficiency, both models exhibited similar degradation trends in moderate waves, but the CSM showed greater sensitivity in long-wave conditions, highlighting its superior capability in resolving local flow phenomena. These results suggest that while the AD model is sufficient for capturing overall propulsive behaviour and mean trends, the CSM approach is indispensable when detailed blade-scale physics are of interest.

A comparison of the results in model- and full-scale clarified why propulsive efficiencies differ between model and full scale in waves. The variation arises mainly from differences in Reynolds regimes, as well as from distinct wake characteristics. At model scale, a thicker, less developed boundary layer may organize under wave-orbital forcing, occasionally improving inflow uniformity, while at full scale, a thinner and more turbulent boundary layer generates more persistent wake distortions. Consequently, the full-scale ship experiences higher wake fractions and reduced efficiency. Differences in operating point, especially the higher advance coefficient at full scale, further explain these divergences. Together, these effects show that model-scale experiments may sometimes suggest improved hull efficiency under certain wave conditions, whereas at full scale, irregular seas consistently result in a measurable efficiency reduction of roughly 7%.

Despite its strengths, the study's conclusions are bounded by several limitations. The simplified AD approach cannot resolve relative rotative efficiency or blade harmonics, which limits its fidelity under severe sea states. Surge motion was intentionally constrained due to inherent mesh related penalties, omitting possible speed-loss phenomena relevant in higher wave steepness. The irregular wave simulation duration of 5 min, while sufficient for moderate conditions, does not allow for fatigue or extreme event analysis and corresponding propulsion assessments in those conditions. Based on these limitations, several guidelines for future work are established.

## 8.2 Scientific Contributions

Main scientific contributions of this thesis are listed in this chapter. As the thesis is divided in two main areas, the contributions are listed correspondingly. The first part of this thesis focuses on full-scale ship simulations validated against real operational data. The main contributions from this work can be summarized as:

- Numerical simulation of sea trials for an ultra-large container ship where the results are directly compared to actual sea trial measurements. The scale of the Post-Panamax containership expands the current CFD application regarding full-scale sea trials. Currently, these are the largest ship dimensions that are simulated under sea trial conditions and compared with actual data where the results are made public. Results from numerical simulations of sea trials at this scale confirm the maturity of the actuator disk models and their application in full-scale.
- Numerical simulations based on fully viscous and turbulent flow in full-scale while applying irregular sea state where the results of the simulations are directly compared with high-quality onboard measurements from an ultra-large container ship. Such methodology represents a significant and unique contribution in CFD application in ship hydrodynamics, particularly for full-scale cases. Results from the numerical simulations imply that the simplified AD propeller model might be used in preliminary ship design, particularly for the power performance assessment and fuel consumption studies across various navigational conditions.

The second part of this thesis examines model-scale applications and validates two different propulsion modeling approaches. The main contributions include:

- Development and validation of a CSM model that integrates fully discretized propeller geometry with rigid body ship motions using AMI interpolation, enabling accurate simulation of hull-propeller interactions in wave conditions.
- Comparison between low-fidelity actuator disk and high-fidelity fully discretized propeller model in regular head waves, demonstrating the limitations of simplified approach in capturing frequency-dependent phenomena and propeller blade effects.
- Systematic analysis of propulsive efficiency coefficients in waves, quantifying the inherent limitations of AD method, revealing that both approaches show similar trends for thrust deduction and effective wake fractions in wavelengths shorter than approximately  $0.3L_{PP}$ .

- Comprehensive CFD validation study of ship propulsion performance in waves against high-quality experimental data from a free-running DTC model, providing insights into the accuracy requirements for different propeller modelling approaches in propulsion assessments in waves.

Besides the scientific contributions listed, this thesis has yielded direct improvements to the OpenFOAM source code that enhance its capability in ship hydrodynamics. In wave modeling, boundary conditions allowing for diverse simulations including arbitrary wind, waves and currents have been established.

This is achieved through rewritten boundary conditions for the velocity and phase fraction field `waveVelocityFvPatchVectorField` and `waveAbsorptionVelocity2DFvPatchVectorField`, respectively. Several additional utilities have been implemented with function object paradigm. Calculation of wetted surface area of the ship is implemented through `wettedSurfaceArea` class, particularly useful when tracking overall convergence of the simulation and benchmarking different interface tracking methods.

Dynamic switching of the discretization schemes has been implemented with `schemeSwitcher` class, enabling the usage of different numerical schemes within one single simulation. This proved practical for wave simulations when a switch from first to second-order temporal scheme has been required. Also, a post-processing tool for proper calculation of wave spectrum from a random wave trace in time-domain is constructed in python. The most prominent contribution is the Coupled Sliding Mesh (CSM), implemented within the `sixDoFRigidBodyMotion` class that enables the usage of both AMI for rotating propellers and ship rigid body dynamics with morphing mesh approach. All of the numerical contributions listed above are publicly available on the author's GitHub page found at Sulovsky (2025).

### 8.3 Future Work

This research has several practical implications. The AD methodology works well for broad parametric studies, calm water conditions, and moderate sea states, while the blade-resolved CSM approach is essential when accurate hull-propeller interactions, blade-rate phenomena, or complex unsteady inflow dynamics are needed. At full scale, propulsive efficiency decreases by approximately 7% under representative sea conditions, suggesting that conventional sea margins, typically around 15%, may need adjustment for modern hull and propeller designs, especially considering recent advances in voyage optimization and weather routing.

However, any changes to sea margins must carefully consider overall ship safety and maneuverability. Future work should expand direct comparisons between full-scale CFD and onboard measurements across different wave headings, particularly in rough weather conditions. Including air resistance in the simulations would also improve accuracy. This can be modeled separately using a single-phase formulation, where steady-state wind resistance results are applied as additional forces and moments acting on the ship. This approach dramatically reduces computational cost while maintaining reasonable accuracy, though it is limited to the steady-state condition of the wind.

The model-scale results show that involuntary ship speed loss from added resistance significantly affects propulsion performance, confirming that this effect must be included in simulations. However, the morphing mesh approach used in this study cannot easily capture speed loss. Allowing the ship to surge freely would create extreme cell distortion and poor mesh quality, compromising both solution stability and numerical accuracy. This limitation can be avoided by using a fully overset mesh approach, where the entire computational domain moves with the ship. Combined with realistic irregular wave spectra, this method would provide the most complete representation of ship behaviour at sea, particularly important for full-scale predictions.

Regarding possible numerical improvements of the propulsion models developed within this thesis, the AD model can be improved in several ways. Firstly, a more accurate distribution of thrust and torque can be implemented, that is not based solely on Goldstein optimum but rather on pressure distribution on the blades coming from high-fidelity CFD. Also, as already mentioned in chapter 3.1, adjustable propeller revolution rate would significantly enhance the model's capabilities.

The second model developed within the thesis, CSM, can be improved to account for twin screw ships as the current implementation assumes a single rotating zone. This would expand its applicability to multiple ship types and propulsion arrangements. Furthermore, as already indicated in subchapter 3.2 where the implementation details of CSM model are outlined, a "protected" propeller cell zone irrespective of the region where the grid points are moving with the same magnitude as a rigid body (inner distance region), within the SLERP interpolation field can be implemented. Such improvement might be of interest for application in the field of numerical modelling of Floating Offshore Wind Platform (FOWT) as the rotor blades are significantly larger than the tower and floating platform, opposed to the ship's propeller and hull topology. Also, this would require an implementation of flow-induced rotation of the blades, opposed to the a priori known rotation rate of the propeller.

## References

- M.A. Ali, H. Peng, and W. Qiu. Propeller–hull interaction simulation for self-propulsion with sinkage and trim. *Physics of Fluids*, 36(2):025159, 2024. doi: 10.1063/5.0183523.
- Stephen B. Pope. *Turbulent Flows*. Cambridge University Press, Cambridge, UK, 2000. ISBN 978-0521598866. doi: 10.1017/CBO9780511840531.
- A. Bakica, I. Gatin, V. Vukčević, H. Jasak, and N. Vladimir. Accurate assessment of ship-propulsion characteristics using CFD. *Ocean Engineering*, 175:149–162, 2019. ISSN 0029-8018. doi: 10.1016/j.oceaneng.2018.12.043.
- A. Bakica, N. Vladimir, I. Gatin, and H. Jasak. CFD simulation of loadings on circular duct in calm water and waves. *Ships and Offshore Structures*, 15(sup1):S110–S122, 2020. doi: 10.1080/17445302.2020.1730082.
- Zoltan Benedek. The Scale Effect on Nominal Wake Fraction of Single-Screw Ships. *Periodica Polytechnica, Mechanical Engineering*, 11(4):25–38, 1967.
- Lothar Birk. *Introduction to Ship Propulsion*. Wiley, 2019. ISBN 9781119191575. doi: 10.1002/9781119191575.ch32.
- A. M. Castro, P. Carrica, and F. Stern. Full scale self-propulsion computations using discretized propeller for the KRISO container ship KCS. *Computers & Fluids*, 51(1): 35–47, 2011. ISSN 0045-7930. doi: 10.1016/j.compfluid.2011.07.005.
- N. Degiuli, C.G. Grlj, I. Martić, S.B. Šegota, N. Anđelić, and D. Majnarić. Machine Learning Models for the Prediction of Wind Loads on Containerships. *Journal of Marine Science and Engineering*, 13(3), 2025. doi: 10.3390/jmse13030417.
- G.B. Deng, P. Queutey, and M. Visonneau. Three-Dimensional Flow Computation with Reynolds Stress and Algebraic Stress Models. In W. Rodi and M. Mulas, editors, *Engineering Turbulence Modelling and Experiments 6*, pages 389–398. Elsevier Science B.V., Amsterdam, 2005. ISBN 978-0-08-044544-1. doi: 10.1016/B978-008044544-1/50037-6.

- G. Dodet, X. Bertin, and R. Taborda. Wave climate variability in the North-East Atlantic Ocean over the last six decades. *Ocean Modelling*, 31(3):120–131, 2010. ISSN 1463-5003. doi: 10.1016/j.ocemod.2009.10.010.
- L. Eça and M. Hoekstra. The numerical friction line. *Journal of Marine Science and Technology*, 13:328–345, 2008. doi: 10.1007/s00773-008-0018-1.
- L. Eça and M. Hoekstra. A procedure for the estimation of the numerical uncertainty of CFD calculations based on grid refinement studies. *Journal of Computational Physics*, 262:104–130, 2014. doi: 10.1016/j.jcp.2014.01.006.
- O. el Moctar, V. Shigunov, and Zorn T. Duisburg Test Case: Post-Panamax Container Ship for Benchmarking. *Ship Technology Research*, 59(3):50–64, 2012. doi: 10.1179/str.2012.59.3.004.
- O. el Moctar, T. E. Schellin, and H. Söding. *Numerical Methods for Seakeeping Problems*. Springer Cham, 1st edition, 2021. ISBN 978-3-030-62561-0. doi: 10.1007/978-3-030-62561-0.
- Odd Magnus Faltinsen. *Sea Loads on Ships and Offshore Structures*. Cambridge University Press, 1990. ISBN 0-521-45870-6.
- J. H. Ferziger and M. Perić. *Computational Methods for Fluid Dynamics*. Springer, Berlin, Heidelberg, 3 edition, 2002. ISBN 978-3-642-56026-2. doi: 10.1007/978-3-642-56026-2.
- I. Gatin, V. Vukčević, H. Jasak, and H. Rusche. Enhanced coupling of solid body motion and fluid flow in finite volume framework. *Ocean Engineering*, 143:295–304, 2017. ISSN 0029-8018. doi: 10.1016/j.oceaneng.2017.08.009.
- I. Gatin, S. Liu, V. Vukčević, and H. Jasak. Finite Volume method for general compressible naval hydrodynamics. *Ocean Engineering*, 196:106773, 2020. ISSN 0029-8018. doi: 10.1016/j.oceaneng.2019.106773.
- Sydney Goldstein. On the optimum velocity distribution for a propeller in axial flow. *Journal of the Aeronautical Sciences*, 2:1–12, 1929.
- C. G. Grlj, N. Degiuli, and I. Martić. Assessment of the effect of speed and scale on the total resistance and its components for a bulk carrier. *Results in Engineering*, 26:105095, 2025. ISSN 2590-1230. doi: 10.1016/j.rineng.2025.105095.

- C.G. Grlj, N. Degiuli, Ž. Tuković, A. Farkas, and I. Martić. The effect of loading conditions and ship speed on the wind and air resistance of a containership. *Ocean Engineering*, 273:113991, 2023. doi: 10.1016/j.oceaneng.2023.113991.
- P. Halder and S. Liu. Numerical investigation of added resistance of a container ship in short regular waves using unsteady RANS simulations. *Brodogradnja: An International Journal of Naval Architecture and Ocean Engineering for Research and Development*, 76(2):1–27, 2025. doi: 10.21278/brod76204.
- P. Higuera, J.L. Lara, and I.J. Losada. Realistic wave generation and active wave absorption for Navier-Stokes models: Application to OpenFOAM. *Coastal Engineering*, 71:102–118, 2013. doi: 10.1016/j.coastaleng.2012.07.002.
- Takanori Hino. A 3D unstructured grid method for incompressible viscous flows. *Journal of the society of Naval Architects of Japan*, 1997(182):9–15, 1997.
- Julius Oscar Hinze. *Turbulence*. McGraw-Hill, New York, NY, 2nd edition, 1975. ISBN 978-0070290372.
- N. Hogben and F. E. Lumb. *Ocean Wave Statistics: A Statistical Survey of Wave Characteristics Estimated Visually from Voluntary Observing Ships Sailing Along the Shipping Routes of the World*. H.M. Stationery Office, London, 1967.
- L. Huang, B. Pena, and G. Thomas. Towards a full-scale CFD guideline for simulating a ship advancing in open water. *Ship Technology Research*, 70(3):222–238, 2023. doi: 10.1080/09377255.2023.2167537.
- International Towing Tank Conference (ITTC). Recommended Procedures and Guidelines 7.5-02-03-02.5: Experimental Wake Scaling Methods. Technical report, International Towing Tank Conference, 2011. URL <https://ittc.info/media/1247/75-02-03-025.pdf>. Provides standardized experimental procedures for wake scaling emphasizing Reynolds number effects over Froude number similarity.
- M. Irannezhad, M. Kjellberg, R.E. Bensow, and A. Eslamdoost. Impacts of regular head waves on thrust deduction at model self-propulsion point. *Ocean Engineering*, 309:118375, 2024. ISSN 0029-8018. doi: 10.1016/j.oceaneng.2024.118375.

- ITTC. Practical Guidelines for Ship CFD Applications. Recommended Procedures and Guidelines 7.5-03-02-03, International Towing Tank Conference, 2017a.
- ITTC. Seakeeping Experiments. Recommended Procedures and Guidelines 7.5-02-07-02.1, International Towing Tank Conference, 2017b.
- ITTC Specialist Committee on Scaling of Wake Field. The Specialist Committee on Scaling of Wake Field: Final Report and Recommendations to the 26th ITTC. Technical report, International Towing Tank Conference (ITTC), 2011.
- W. Jabary, F. Sprenger, L. Kleinsorge, H. Baumfalk, S. Mewes, J. Neugebauer, C. Jiang, and O. el Moctar. Development of a Unified Data Model to Improve Ship Operational Performance Analyses. In *COMPIT 2022*, Pontignano, Italy, 2022.
- W. Jabary, F. Sprenger, C. Liu, L. Kleinsorge, H. Baumfalk, M. Kaster, S. Mewes, J. Neugebauer, C. Jiang, and O. el Moctar. Development of machine learning approaches to enhance ship operational performance evaluation based on an integrated data model. In *ISOPE 2022*, Ottawa, Canada, 2023.
- H. Jasak and T. Uroić. *Practical Computational Fluid Dynamics with the Finite Volume Method*, pages 103–161. Springer International Publishing, Cham, 2020.
- H. Jasak, V. Vukčević, I. Gatin, and I. Lalović. CFD validation and grid sensitivity studies of full scale ship self propulsion. *International Journal of Naval Architecture and Ocean Engineering*, 11(1):33–43, 2019. ISSN 2092-6782. doi: 10.1016/j.ijnaoe.2017.12.004.
- Hrvoje Jasak. *Error Analysis and Estimation for the Finite Volume Method with Applications to Fluid Flows*. Phd thesis, Imperial College London, 1996.
- Hrvoje Jasak. OpenFOAM : Open Source CFD in Research and Industry. *international Journal of Naval Architects, elsevier BV.*, 12 2009. doi: 10.3744/jnaoe.2009.1.2.089.
- S. Jeong, H.S. Kim, Y.H. Jang, B.U. You, and K.J. Paik. Development of Virtual Disk Method for Propeller Interacting with Free Surface. *Journal of Marine Science and Engineering*, 13(10), 2025. ISSN 2077-1312. doi: 10.3390/jmse13101912.
- T. Kawamura, K. Ouchi, and S. Takeuchi. Model and full scale CFD analysis of propeller boss cap fins (PBCF). In *Third International Symposium on Marine Propulsors*, Tasmania, Australia, 2013.

- D. Kim and T. Tezdogan. CFD-based hydrodynamic analyses of ship course keeping control and turning performance in irregular waves. *Ocean Engineering*, 248:110808, 2022. ISSN 0029-8018. doi: 10.1016/j.oceaneng.2022.110808.
- Ö. Kemal Kinaci, M.K. Gokce, A.D. Alkan, and A. Kukner. On Self-Propulsion Assessment of Marine Vehicles. *Brodogradnja*, 69(4):29–51, 2018. doi: 10.21278/brod69403.
- V. Krasilnikov, V. S. Skjefstad, K. Koushan, and H.J. Rambech. A Calibration Study with CFD Methodology for Self-Propulsion Simulations at Ship Scale. *Journal of Marine Science and Engineering*, 11(7):1342, 2023. doi: 10.3390/jmse11071342.
- J. Larsson and F. Stern. Verification and Validation of Ship Hydrodynamics Computational Methods. In Takanori Hino, editor, *Proceedings of the Tokyo 2015 Workshop on CFD in Ship Hydrodynamics*, volume 3, pages 287–296, Tokyo, Japan, 2015. National Maritime Research Institute.
- S. Lemaire, G. Vaz, M. D. van Rijswijk, and S.R. Turnock. Influence of Interpolation Scheme on the Accuracy of Overset Method for Computing Rudder-Propeller Interaction. *Journal of Verification, Validation and Uncertainty Quantification*, 8(1):011002, March 2023. doi: 10.1115/1.4056681.
- R. Lopes, A. Eslamdoost, R. Johansson, S. RoyChoudhury, R.E. Bensow, P. Hogström, and D. Ponkratov. Resistance prediction using CFD at model- and full-scale and comparison with measurements. *Ocean Engineering*, 321:120367, 2025. ISSN 0029-8018. doi: 10.1016/j.oceaneng.2025.120367.
- H. Mahmoodi, I. Ghamari, A. Hajivand, and M. MAnsoori. A CFD investigation of the propulsion performance of a low-speed VLCC tanker at different initial trim angles. *Ocean Engineering*, 275:114148, 2023. ISSN 0029-8018. doi: 10.1016/j.oceaneng.2023.114148.
- Florian Menter. Two-equation eddy-viscosity turbulence models for engineering applications. *AIAA Journal*, 32(8):1598–1605, 1994. doi: 10.2514/3.12149.
- M. Mikulec and H. Piehl. Verification and validation of CFD simulations with full-scale ship speed/power trial data. *Brodogradnja*, 74(1):41–62, 2023.

- A. Molland, S.R. Turnock, and D.A. Hudson. *Ship Resistance and Propulsion: Practical Estimation of Ship Propulsive Power*. Cambridge University Press, Cambridge, September 2011. ISBN 9780511974113. doi: 10.1017/CBO9780511974113.
- H. Orihara and M. Tsujimoto. Performance prediction of full-scale ship and analysis by means of on-board monitoring. Part 2: Validation of full-scale performance predictions in actual seas. *Journal of Marine Science and Technology*, 23:782–801, 2018. doi: 10.1007/s00773-017-0511-5.
- M. Orych, S. Werner, and L. Larsson. Roughness effect modelling for wall resolved RANS – Comparison of methods for marine hydrodynamics. *Ocean Engineering*, 266:112778, 2022. ISSN 0029-8018. doi: 10.1016/j.oceaneng.2022.112778.
- M. Orych, M. Östberg, M. Kjellberg, S. Werner, and L. Larsson. Speed and delivered power in waves — Predictions with CFD simulations at full scale. *Ocean Engineering*, 285:115289, 2023. ISSN 0029-8018. doi: 10.1016/j.oceaneng.2023.115289.
- S. V. Patankar and D. B. Spalding. A calculation procedure for heat, mass and momentum transfer in three-dimensional parabolic flows. *International Journal of Heat and Mass Transfer*, 15:1787–1806, 1972.
- B. Pena and L. Huang. A review on the turbulence modelling strategy for ship hydrodynamic simulations. *Ocean Engineering*, 241:110082, 2021. ISSN 0029-8018. doi: 10.1016/j.oceaneng.2021.110082.
- W.J. Pierson and L. Moskowitz. A proposed spectral form for fully developed wind seas based on the similarity theory of S.A. Kitaigorodskii. *Journal of Geophysical Research*, 69(24):5181–5190, 1964.
- Johanes Albert Pinkster. *Low frequency second order wave exciting forces on floating structures*. PhD thesis, Delft University of Technology, Delft, Netherlands, 1980. MARIN Publication No. 600.
- D. Ponkratov and C. Zegos. Validation of Ship Scale CFD Self-Propulsion Simulation by the Direct Comparison with Sea Trials result. In *Fourth International Symposium on Marine Propulsors*, Austin, USA, 2015.

- J. Prpić-Oršić, M. Valčić, and Z. Čarija. A Hybrid Wind Load Estimation Method for Container Ship Based on Computational Fluid Dynamics and Neural Networks. *Journal of Marine Science and Engineering*, 8(7), 2020. doi: 10.3390/jmse8070539.
- J. Prpić-Oršić, O.M. Faltinsen, I. Sulovsky, and M. Marjanović. Uncertainty of criteria limits of ship operability in rough sea. In *Innovations in Sustainable Maritime Technology—IMAM 2025*, pages 30–41. Springer Nature Switzerland, 2025. doi: 10.1007/978-3-032-01432-0\_3.
- Ø. Rabliås and T. Kristiansen. A rational model for maneuvering in irregular waves with the effect of waves on the propeller and rudder inflow taken into account. *Ocean Engineering*, 243:110186, 2022. ISSN 0029-8018. doi: 10.1016/j.oceaneng.2021.110186.
- Øyvind Rabliås. *Numerical and Experimental Studies of Maneuvering in Regular and Irregular Waves*. Phd thesis, NTNU, Trondheim, Month 2022.
- K. J. Rawson and E. C. Tupper. *Basic Ship Theory*. Butterworth-Heinemann, fifth edition, 2001.
- P.J. Roache. *Verification and Validation in Computational Science and Engineering*. Hermosa Publishers, Albuquerque, 1998.
- J. Roenby, H. Bredmose, and H. Jasak. A computational method for sharp interface advection. *Royal Society Open Science*, 3(11), 2016. doi: 10.1098/rsos.160405.
- F. Roshan, A. Dashtimanesh, and R.N. Bilandi. Hydrodynamic characteristics of tunneled planing hulls in calm water. *Brodogradnja*, 71(1):1–18, 2020. ISSN 0007-215X. doi: 10.21278/brod71102.
- Henrik Rusche. *Computational Fluid Dynamics of Dispersed Two-Phase Flows at High Phase Fractions*. Phd thesis, Imperial College London, 2002.
- S. Saettone, B. Taskar, S. Steen, and P. Andersen. Experimental measurements of propulsive factors in following and head waves. *Applied Ocean Research*, 111:102639, 2021. ISSN 0141-1187. doi: 10.1016/j.apor.2021.102639.
- G. Shenwei, J. Zeng, and J. Jua. Full-Scale Numerical Simulation of a Free-Running Cruise Ship in Heavy Head Sea Conditions. *Journal of Marine Science and Engineering*, 13(4), 2025. ISSN 2077-1312. doi: 10.3390/jmse13040626.

- Ken Shoemake. Animating Rotation with Quaternion Curves. *ACM SIGGRAPH Computer Graphics*, 19(3):245–254, 1985. doi: 10.1145/325165.325242.
- S. Sigmund and O. el Moctar. Numerical and experimental investigation of propulsion in waves. *Ocean Engineering*, 144:35–49, 2017. ISSN 0029-8018. doi: 10.1016/j.oceaneng.2017.08.016.
- Claus D. Simonsen and F. Stern. Flow pattern around an appended tanker hull form in simple maneuvering conditions. *ComputersFluids*, 34(2):169–198, 2005. ISSN 0045-7930. doi: 10.1016/j.compfluid.2004.05.001.
- F. Stern, H. T. Kim, V. C. Patel, and H. C. Chen. A Viscous-Flow Approach to the Computation of Propeller-Hull Interaction. *Journal of Ship Research*, 32(04):246–262, December 1988. ISSN 0022-4502. doi: 10.5957/jsr.1988.32.4.246.
- I. Sulovsky and J. Prpić-Oršić. Mathematical model of ship speed drop in irregular waves. In *Book of Abstracts - My First Conference 2021 - 5th Annual PhD Conference*, Rijeka, Croatia, 2021.
- I. Sulovsky and J. Prpić-Oršić. On the Overset Grids in Computational Marine Hydrodynamics. In *Book of Abstracts - My First Conference 2022 - 6th Annual PhD Conference*, Rijeka, Croatia, 2022a.
- I. Sulovsky and J. Prpić-Oršić. Seakeeping analysis of a Double Ended Ferry. *Pomorski zbornik, Special Edition*, 4:223–235, 2022b. doi: 10.18048/2022.04.16.
- I. Sulovsky and J. Prpić-Oršić. Numerical Simulations of a Ship Navigating in Rough Seas. In *Book of Abstracts - My First Conference 2023 - 7th Annual PhD Conference*, Rijeka, Croatia, 2023.
- I. Sulovsky and J. Prpić-Oršić. Computational ship hydrodynamics in full scale: RANS computations using a Post-Panamax containership data. In *Book of Abstracts - My First Conference 2024 - 8th Annual PhD Conference*, Rijeka, Croatia, 2024a.
- I. Sulovsky and J. Prpić-Oršić. Hydrodynamics of ship propulsion in waves: A review. In *Advances in Maritime Technology and Engineering, MARTECH 2024, vol.2*, volume 13 of *Proceedings in Marine Technology and Ocean Engineering*, pages 189–195, 2024b. doi: 10.1201/9781003508779-21.

- I. Sulovsky and J. Prpić-Oršić. On the Development of Numerical Ocean for Seakeeping Simulations in Openfoam®. *Pomorski zbornik, Special Edition*, pages 229–241, 2024c.
- I. Sulovsky and J. Prpić-Oršić. Automatic grid generation for ship calm water computations by coupling python and snappyHexMesh. In *Book of Abstracts - 27th Numerical Towing Tank Symposium September*, Zagreb, Croatia, 2025.
- I. Sulovsky, G. du Hauteclocque, and J. Prpić-Oršić. Application of an Overset Mesh for Wave Response of a Containership Scale Model. In *Book of Abstracts - 24th Numerical Towing Tank Symposium September*, Zagreb, Croatia, 2022.
- I. Sulovsky, R. Dejhalla, and J. Prpić-Oršić. CFD Study on Propulsion Characteristics of Ships Subjected To Waves. In *16th Baška GNSS Conference: Technologies, Techniques and Applications Across PNT and The 3rd Workshop on Smart, Blue and Green Maritime Technologies*, Baška, Croatia, 2023a.
- I. Sulovsky, M. Greco, G. de Hauteclocque, and J. Prpić-Oršić. Comparative Study of Potential Flow and CFD in the Assessment of Seakeeping and Added Resistance of Ships. *Journal of Marine Science and Engineering*, 11(3):641, 2023b. doi: 10.3390/jmse11030641.
- I. Sulovsky, S. Mewes, O. el Moctar, and J. Prpić-Oršić. URANS - based Simulation of Ship Propulsion in Seaways. In *Book of Abstracts - 25th Numerical Towing Tank Symposium September*, Ericeira, Portugal, 2023.
- I. Sulovsky, S. Mewes, O. el Moctar, and J. Prpić-Oršić. CFD study on a full-scale ship performance in a representative sea state. *Ocean Engineering*, 333:121519, 2025. ISSN 0029-8018. doi: 10.1016/j.oceaneng.2025.121519.
- I. Sulovsky, A. Bakica, and J. Prpić-Oršić. CFD assessment of ship propulsion and propeller-hull interactions in waves using low and high fidelity approach. *Ocean Engineering*, 346: 123843, 2026. ISSN 0029-8018. doi: doi.org/10.1016/j.oceaneng.2025.123843.
- Ivan Sulovsky. OpenFOAM Extensions for Ship Hydrodynamics. <https://github.com/isulovsky>, 2025. Accessed: 2025-10-17.

- Y. Tahara and F. Stern. A Large-Domain Approach for Calculating Ship Boundary Layers and Wakes and Wave Fields for Nonzero Froude Number. *Journal of Computational Physics*, 127(2):398–411, 1996. ISSN 0021-9991. doi: 10.1006/jcph.1996.0183.
- J. Tu, G.H. Yeoh, and Chaoqun Liu. Chapter 7 - Practical Guidelines for CFD Simulation and Analysis. In Jiyuan Tu, Guan-Heng Yeoh, and Chaoqun Liu, editors, *Computational Fluid Dynamics (Third Edition)*, pages 255–290. Butterworth-Heinemann, third edition edition, 2018. ISBN 978-0-08-101127-0. doi: 10.1016/B978-0-08-101127-0.00007-6.
- Željko Tuković. *Metoda kontrolnih volumena na domenama promjenjivog oblika*. Doctoral thesis, University of Zagreb, Faculty of Mechanical Engineering and Naval Architecture, 2005.
- A. Turk, I. Sulovsky, M. Marjanović, and J. Prpić-Oršić. Evaluating Roll Damping in Parametric Rolling: Challenges and Approaches. *Theory and Practice of Shipbuilding*, 9:139–150, 2024. doi: 10.3233/PMST240034.
- S. Turnock, S. Hosseinzadeh, Y. Zhang, J. Bowker, D. Buckland, M. Gregory, and N. Townsend. Hull-propeller-rudder interactions: Time-accurate data of a scaled model ship in waves. *Ocean Engineering*, 312:119258, 2024. ISSN 0029-8018. doi: 10.1016/j.oceaneng.2024.119258.
- S. Đurasević, I. Gatin, T. Uroić, and H. Jasak. Hydrodynamic performance of a full-scale ship with a Pre-Swirl Duct: A numerical study with partially rotating grid method. *Ocean Engineering*, 283:1–23, 2023. doi: 10.1016/j.oceaneng.2023.115049.
- S. Đurasević, I. Gatin, and H. Jasak. Numerical simulations of the ONRT ship maneuvering in calm water and head waves with the partially rotating grid method. *Ocean Engineering*, 312:119056, 2024. ISSN 0029-8018. doi: 10.1016/j.oceaneng.2024.119056.
- M. Valčić and J. Prpić-Oršić. Hybrid method for estimating wind loads on ships based on elliptic fourier analysis and radial basis neural networks. *Ocean Engineering*, 122: 227–240, 2016. doi: 10.1016/j.oceaneng.2016.06.031.
- H. K. Versteeg and W. Malalasekera. *An Introduction to Computational Fluid Dynamics: The Finite Volume Method*. Pearson Education, Harlow, England, 2 edition, 2007. ISBN 978-0-13-127498-3.

- D. Villa and S. Gaggero. Ship Self Propulsion with Different CFD Methods: from Actuator Disk to Viscous-Inviscid Unsteady Coupled Solvers. In *10th International Conference on Hydrodynamics ICHD'12*, St. Petersburg, Russia, October 1-4 2012.
- V. Vukčević, H. Jasak, I. Gatin, and T. Uroić. Ship scale self propulsion CFD simulation results compared to sea trial measurements. In *VII International Conference on Computational Methods in Marine Engineering, MARINE 2017*, pages 1052–1061, Barcelona, 2017a. International Center for Numerical Methods in Engineering (CIMNE).
- V. Vukčević, H. Jasak, and I. Gatin. Implementation of the Ghost Fluid Method for free surface flows in polyhedral Finite Volume framework. *Computers & Fluids*, 153:1–19, 2017b. ISSN 0045-7930. doi: 10.1016/j.compfluid.2017.05.003.
- H. Wang, X. Xiang, G. Xiang, C. Liu, and L. Yang. An improved body force method for simulation of self-propulsion AUV with ducted propeller. *Ocean Engineering*, 281: 114731, 2023. ISSN 0029-8018. doi: 10.1016/j.oceaneng.2023.114731.
- H.G. Weller, G. Tabor, H. Jasak, and H C. Fureby. A tensorial approach to computational continuum mechanics using object-oriented techniques. *Computer in Physics*, 12(6): 620–631, 11 1998. ISSN 0894-1866. doi: 10.1063/1.168744.
- David C. Wilcox. *Turbulence Modeling for CFD*. DCW Industries, La Canada, CA, 3rd edition, 2006. ISBN 978-1928729082.
- Saad Yousef. *4. Basic Iterative Methods*, pages 103–128. Springer, 2003. ISBN 978-3-642-56026-2. doi: 10.1137/1.9780898718003.ch4.
- J. Yu, C. Yao, L. Liu, D. Feng, and X. Wang. Application of virtual disk propulsion model for self-propelled surface ship in regular head wave. *Journal of Marine Science and Technology*, 28:471–495, 2023. doi: 10.1007/s00773-023-00935-8.

## List of Figures

1	Polyhedral control volume with geometric notation . . . . .	19
2	Typical mesh topology in self-propulsion simulations with AD . . . . .	25
3	Computational workflow of the AD model . . . . .	26
4	Typical mesh topology in propulsion simulations with CSM . . . . .	29
5	Computational workflow of the CSM model . . . . .	30
6	Methodology for calculation of propulsion coefficients in waves . . . . .	35
7	The asymmetrical rudder and the propeller with PBCF . . . . .	38
8	GPS trail of the Post-Panamax Containership . . . . .	39
9	Environmental onboard measurements . . . . .	40
10	Navigational onboard measurements . . . . .	41
11	Computational domain for open water simulations . . . . .	42
12	Reverse open water test from (Kawamura et al., 2013) . . . . .	42
13	Mesh for open water simulations . . . . .	43
14	Velocity field in the open water simulation for $J = 0.5$ . . . . .	43
15	Open water propeller curves . . . . .	45
16	Boundaries of the computational domain for sea trial simulations . . . . .	47
17	Kelvin wake refinements . . . . .	48
18	Cross section at propeller plane and center line . . . . .	48
19	Resistance and thrust signals from the sea trial simulation . . . . .	49
20	Wave elevations from sea trial simulations . . . . .	51
21	Air resistance signal and velocity field over superstructure . . . . .	52
22	Wave Statistics from (Hogben and Lumb, 1967) . . . . .	53
23	Validation dataset of shipboard measurements . . . . .	54
24	Validation dataset of environmental onboard measurements . . . . .	55
25	Wave elevations in time domain with recreated wave spectrum . . . . .	57
26	Comparison of CFD results and onboard measurements . . . . .	59
27	The surrounding wave field of the ship operating under RSS conditions . . . . .	61

28	Experimental DTC model. Reprinted from (Rabliås, 2022) with permission of the author . . . . .	64
29	Aft and bow sections of the model. Reprinted from (Rabliås, 2022) with permission of the author . . . . .	64
30	Open water curves of the DTC propeller . . . . .	65
31	Boundaries of the computational domain for sea trial simulations . . . . .	67
32	Mesh regions for propulsion models . . . . .	67
33	Discretized boundary layer at the bilge area of the DTC hull . . . . .	68
34	Computational domain for 2D wave propagation study . . . . .	70
35	Results from the 2D wave propagation study . . . . .	70
36	Computational grid for wave simulations - bottom view . . . . .	71
37	Computational grid for wave simulations - transversal view . . . . .	72
38	RAO for heave and pitch motion . . . . .	73
39	Comparison of FFT results for $H = 0.061 m$ , $\lambda_e/L_{PP} = 0.187$ . . . . .	75
40	Comparison of FFT results for $H = 0.087 m$ , $\lambda_e/L_{PP} = 0.3$ . . . . .	76
41	Comparison of FFT for $H = 0.112 m$ , $\lambda_e/L_{PP} = 0.46$ . . . . .	77
42	Computed wave fields for different wave conditions . . . . .	78
43	Value of the first harmonic for thrust and torque coefficients . . . . .	79
44	Mean value of thrust and torque coefficients . . . . .	80
45	Q-criterion iso-surface at $Q = 250s^{-2}$ . . . . .	81
47	Frequency content of the torque signal for the first wave case . . . . .	82
48	Comparison of thrust frequency content from AD, CSM, and experiments for three wave cases . . . . .	83
49	Comparison of torque frequency content from AD, CSM, and experiments for three wave cases . . . . .	84
50	Open water and hull efficiency from CSM and AD models . . . . .	85
51	Thrust deduction fraction and effective wake fraction from AD and CSM . . . . .	86
52	Comparison of propeller-induced component in the total resistance in one encounter period by CSM . . . . .	86

53	Comparison of propeller-induced component in the total resistance in one encounter period by AD . . . . .	87
54	Relative rotative and quasi-propulsive efficiency obtained with CSM and AD models . . . . .	87
55	Power density spectrum of the delivered power . . . . .	91
56	Power density spectrum of ship motions . . . . .	92
57	Comparison of thrust and torque increases from simulations and experiments	96
58	Location of measurement planes for wake field comparison . . . . .	98
59	Comparison of effective wake fields. Upstream position is located at $0.03L_{PP}$ , downstream at $0.015L_{PP}$ and behind-rudder at $-0.015L_{PP}$ . . . . .	99
60	Propulsive coefficients across full and model scale in calm water conditions	101
61	Comparison of effective wake fields from full and model-scale. Upstream position is located at $0.03L_{PP}$ , downstream at $0.015L_{PP}$ and behind-rudder is at $-0.015L_{PP}$ . . . . .	102

## List of Tables

1	Main features of the ship and propeller . . . . .	38
2	Verification study for open water propeller simulations . . . . .	44
3	Calculated GCI indexes for thrust and torque coefficients . . . . .	44
4	Ship parameters for a sea trial condition . . . . .	46
5	Results of sea trial simulations . . . . .	50
6	Comparison of numerical and theoretical spectrum statistics . . . . .	58
7	Features of the ship and propeller in navigation . . . . .	59
8	Comparison of onboard measurements and CFD . . . . .	60
9	Propulsion coefficients comparison . . . . .	62
10	DTC model particulars . . . . .	65
11	Experimental test matrix for regular waves . . . . .	66
12	Results of self-propulsion simulations in calm water . . . . .	68
13	Grid characteristics for wave propagation study . . . . .	69
14	Comparison of full and model scale ship particulars and dimensionless coefficients . . . . .	100

## Abbreviations

**AD** Actuator Disk

**AMI** Arbitrary Mesh Interface

**CFD** Computational Fluid Dynamics

**CV** Control Volume

**CPU** Central Processing Unit

**CSM** Coupled Sliding Mesh

**DFT** Discrete Fourier Transform

**DIC** Diagonal Incomplete Cholesky

**DTC** Duisburg Test Case

**ESD** Energy Saving Device

**FVM** Finite Volume Method

**FOWT** Floating Offshore Wind Platform

**GHG** Greenhouse Gas

**GPS** Global Positioning System

**HVAC** Heating, Ventilation and Air Conditioning

**HPC** High-Performance Computing

**GCI** Grid Convergence Index

**IMU** Inertial Motion Unit

**ITTC** International Towing Tank Conference

**JIP** Joint Industry Project

**ONRT** Office of Naval Research Tumblehome

**PBCF** Propeller Boss Cap Fins

**PDE** Partial Differential Equations

**PBiCGStab** Preconditioned BiConjugate Gradient Stabilized

**PISO** Pressure-Implicit with Splitting of Operators

**PCG** Preconditioned Conjugate Gradient

**PM** Pierson-Moskowitz Spectrum

**RAO** Response Amplitude Operator

**RSS** Representative Sea State

**RSM** Reynolds Stress Model

**RANS** Reynolds-Averaged Navier-Stokes

**RTIM** Resistance and Thrust Identity Method

**SIMPLE** Semi-Implicit Method for Pressure Linked Equations

**SLERP** Spherical Linear Interpolation

**VOF** Volume of Fluid

## List of Publications

### Journal articles

1. I. Sulovsky, M. Greco, G. de Hauteclocque, and J. Prpić-Oršić. Comparative Study of Potential Flow and CFD in the Assessment of Seakeeping and Added Resistance of Ships. *Journal of Marine Science and Engineering*, 11(3):641, 2023b. doi: 10.3390/jmse11030641
2. I. Sulovsky, S. Mewes, O. el Moctar, and J. Prpić-Oršić. CFD study on a full-scale ship performance in a representative sea state. *Ocean Engineering*, 333:121519, 2025. ISSN 0029-8018. doi: 10.1016/j.oceaneng.2025.121519
3. I. Sulovsky, A. Bakica, and J. Prpić-Oršić. CFD assessment of ship propulsion and propeller-hull interactions in waves using low and high fidelity approach. *Ocean Engineering*, 346:123843, 2026. ISSN 0029-8018. doi: doi.org/10.1016/j.oceaneng.2025.123843

### Conference Proceedings

1. I. Sulovsky and J. Prpić-Oršić. Seakeeping analysis of a Double Ended Ferry. *Pomorski zbornik, Special Edition*, 4:223–235, 2022b. doi: 10.18048/2022.04.16
2. I. Sulovsky and J. Prpić-Oršić. On the Development of Numerical Ocean for Seakeeping Simulations in Openfoam®. *Pomorski zbornik, Special Edition*, pages 229–241, 2024c
3. I. Sulovsky and J. Prpić-Oršić. Hydrodynamics of ship propulsion in waves: A review. In *Advances in Maritime Technology and Engineering, MARTECH 2024, vol.2*, volume 13 of *Proceedings in Marine Technology and Ocean Engineering*, pages 189–195, 2024b. doi: 10.1201/9781003508779-21
4. A. Turk, I. Sulovsky, M. Marjanović, and J. Prpić-Oršić. Evaluating Roll Damping in Parametric Rolling: Challenges and Approaches. *Theory and Practice of Shipbuilding*, 9:139–150, 2024. doi: 10.3233/PMST240034

5. J. Prpić-Oršić, O.M. Faltinsen, I. Sulovsky, and M. Marjanović. Uncertainty of criteria limits of ship operability in rough sea. In *Innovations in Sustainable Maritime Technology—IMAM 2025*, pages 30–41. Springer Nature Switzerland, 2025. doi: 10.1007/978-3-032-01432-0\_3

## Conference Abstracts

1. I. Sulovsky and J. Prpić-Oršić. Mathematical model of ship speed drop in irregular waves. In *Book of Abstracts - My First Conference 2021 - 5th Annual PhD Conference*, Rijeka, Croatia, 2021
2. I. Sulovsky and J. Prpić-Oršić. On the Overset Grids in Computational Marine Hydrodynamics. In *Book of Abstracts - My First Conference 2022 - 6th Annual PhD Conference*, Rijeka, Croatia, 2022a
3. I. Sulovsky, G. du Hauteclocque, and J. Prpić-Oršić. Application of an Overset Mesh for Wave Response of a Containership Scale Model. In *Book of Abstracts - 24th Numerical Towing Tank Symposium September*, Zagreb, Croatia, 2022
4. I. Sulovsky and J. Prpić-Oršić. Numerical Simulations of a Ship Navigating in Rough Seas. In *Book of Abstracts - My First Conference 2023 - 7th Annual PhD Conference*, Rijeka, Croatia, 2023
5. I. Sulovsky, R. Dejhalla, and J. Prpić-Oršić. CFD Study on Propulsion Characteristics of Ships Subjected To Waves. In *16th Baška GNSS Conference: Technologies, Techniques and Applications Across PNT and The 3rd Workshop on Smart, Blue and Green Maritime Technologies*, Baška, Croatia, 2023a
6. I. Sulovsky, S. Mewes, O. el Moctar, and J. Prpić-Oršić. URANS - based Simulation of Ship Propulsion in Seaways. In *Book of Abstracts - 25th Numerical Towing Tank Symposium September*, Ericeira, Portugal, 2023
7. I. Sulovsky and J. Prpić-Oršić. Computational ship hydrodynamics in full scale: RANS computations using a Post-Panamax containership data. In *Book of Abstracts - My First Conference 2024 - 8th Annual PhD Conference*, Rijeka, Croatia, 2024a

8. I. Sulovsky and J. Prpić-Oršić. Automatic grid generation for ship calm water computations by coupling python and snappyHexMesh. In *Book of Abstracts - 27th Numerical Towing Tank Symposium September, Zagreb, Croatia, 2025*

## Curriculum Vitae

Ivan Sulovsky was born on 3<sup>th</sup> October, 1993 in Rijeka, Croatia, where he completed both elementary and high school, the Technical school for mechanical engineering and naval architecture. Afterwards, he received the Mag.ing.nav.arch (MSc) deegree in the field of naval architecture from the Faculty of Engineering, University of Rijeka in 2018. During his master's deegree, he received the Dean's award for excellence for two years consecutively. After graduation, he works in several ship design offices in Rijeka region for two years after which he is enrolled as a teaching and research assistant at Faculty of Engineering, University of Rijeka at the Department of Naval Architecture and Ocean Engineering. At the same time he begins with his doctoral study under the supervision of Prof. dr. sc. Jasna Prpić-Oršić. His research interest cover the development and application of computational methods for problems in ship hydrodynamics, including resistance and self-propulsion, seakeeping etc. Ivan has been involved in collaborative research projects with institutions such as the University of Duisburg-Essen and Norwegian University of Science and Technology, where he spent three months altogether. He has participated in the course "Hydrodynamics in Ship Design", held in MARIN, Wageningen. During his doctoral study, Ivan presented his work at numerous international conferences and workshops in the field of ship hydrodynamics. As of 2024., he co-leads a part of the COST project DEWATRA related to the hydrodynamic optimizations of ships. He currently lives in Rijeka, Croatia, is married, and is a father of two children.